

**AN IMPROVED OCEAN VECTOR WINDS RETRIEVAL APPROACH USING C- AND
Ku-BAND SCATTEROMETER AND MULTI-FREQUENCY MICROWAVE
RADIOMETER MEASUREMENTS**

by

SULEIMAN ODEH ALSWEISS
M.S. University of Central Florida, 2007

A dissertation submitted in partial fulfillment of the requirements
for the degree of Doctor of Philosophy
in the Department of Electrical Engineering and Computer Science
in the College of Engineering and Computer Science
at the University of Central Florida
Orlando, Florida

Spring Term
2011

Major Professor: W. Linwood Jones

© 2011 Suleiman Odeh Alsweiss

ABSTRACT

This dissertation will specifically address the issue of improving the quality of satellite scatterometer retrieved ocean surface vector winds (OVW), especially in the presence of strong rain associated with tropical cyclones. A novel active/passive OVW retrieval algorithm is developed that corrects Ku-band scatterometer measurements for rain effects and then uses them to retrieve accurate OVW. The rain correction procedure makes use of independent information available from collocated multi-frequency passive microwave observations provided by a companion sensor and also from simultaneous C-band scatterometer measurements. The synergy of these active and passive measurements enables improved correction for rain effects, which enhances the utility of Ku-band scatterometer measurements in extreme wind events.

The OVW retrieval algorithm is based on the next generation instrument conceptual design for future US scatterometers, i.e. the Dual Frequency Scatterometer (DFS) developed by NASA's Jet Propulsion Laboratory. Under this dissertation research, an end-to-end computer simulation was developed to evaluate the performance of this active/passive technique for retrieving hurricane force winds in the presence of intense rain. High-resolution hurricane wind and precipitation fields were simulated for several scenes of Hurricane Isabel in 2003 using the Weather Research and Forecasting (WRF) Model. Using these numerical weather model environmental fields, active/passive measurements were simulated for instruments proposed for the Global Change Observation Mission- Water Cycle (GCOM-W2) satellite series planned by the Japanese Aerospace Exploration Agency. Further, the quality of the simulation was evaluated using actual hurricane measurements from the Advanced Microwave Scanning Radiometer and

SeaWinds scatterometer onboard the Advanced Earth Observing Satellite-II (ADEOS-II). The analysis of these satellite data provided confidence in the capability of the simulation to generate realistic active/passive measurements at the top of the atmosphere.

Results are very encouraging, and they show that the new algorithm can retrieve accurate ocean surface wind speeds in realistic hurricane conditions using the rain corrected Ku-band scatterometer measurements. They demonstrate the potential to improve wind measurements in extreme wind events for future wind scatterometry missions such as the proposed GCOM-W2.

Standing before the committee, watching a dream coming true, I saw your face, and I recognized that the true reason behind a successful man, is a loving woman, who worth the whole world.

Diala ... I love you

Standing before the committee, watching a dream coming true, I heard your voice, and I recognized that you always make me want to be a better man.

Dad ... I love you

Standing before the committee, watching a dream coming true, I felt your prayers, and I recognized how I was able to survive all the hard times.

Mom ... I love you

Standing before the committee, watching a dream coming true, I remembered your smiles, and I recognized how blessed I am to have you all.

Kanar, Malek, Manar, & Joseph ... I love you

To all of you, and to my beloved country JORDAN, I dedicate the fruit of these years of hard work,

ACKNOWLEDGMENTS

I would like to express my sincere gratefulness and appreciation to my advisor, Dr. W. Linwood Jones, for his guidance, dedication, and support throughout the program. His mentorship was paramount in providing a well rounded experience consistent with my long-term career goals. In addition, I would like to thank my committee members: Dr. Wasfy Mikhael, Dr. Michael Georgeopolous, and Dr. Svetla H. Veleva for their insightful advice.

I would like to acknowledge my parents and family for their faith in me, and allowing me to be as ambitious as I wanted. Most importantly, I would like to thank my wife Diala, for her endless love and support throughout all the hard times I endured. They have always been there to brace my falls.

Special thanks go to my friends Salem El-Nimri and Ruba Amarin who taught me the true meaning of friendship.

Also, I am thankful to my team members at CFRSL for their continuous assistance. In particular, I would like to thank Dr. Peth Laupattarakasem for all his help. Last but not least I would like to thank all of my friends for their encouragements.

This work was accomplished with the help of Dr. Svetla Hristova-Veleva, Radar Science and Engineering, JPL.

TABLE OF CONTENTS

LIST OF FIGURES	x
LIST OF TABLES	xv
LIST OF ACRONYMS / ABBREVIATIONS	xvi
CHAPTER 1 : INTRODUCTION	1
1.1 Scatterometers Applications and Limitations in Tropical Cyclones.....	2
1.2 Future Scatterometer Missions Requirements	3
1.3 Dissertation Objectives	5
CHAPTER 2 : ACTIVE REMOTE SENSING OF OCEAN WINDS	8
2.1 Space-borne Scatterometers.....	9
2.2 The Geophysical Model Function.....	12
2.3 Estimation of Wind Velocity from Scatterometer Measurements	17
2.4 Rain Effects on Radar backscatter	22
CHAPTER 3 : ACTIVE/PASSIVE SIMULATION OVERVIEW	25
3.1 Instruments.....	26
3.1.1 Dual Frequency Scatterometer (DFS).....	26
3.1.2 Advanced Microwave Scanning Radiometer (AMSR).....	31
3.1.3 SeaWinds	32
3.2 Data products and Numerical Weather Model.....	35

3.2.1	ADEOS-II Data Products.....	36
3.2.2	Weather Research and Forecasting Model	37
3.3	Realistic Measurements Simulation.....	40
3.3.1	Viewing Geometry Simulation	41
3.3.2	DFS Observations Simulation.....	42
3.3.3	AMSR Brightness Temperatures Simulation.....	46
3.4	Validation of Simulated Measurements.....	49
CHAPTER 4 : WIND RETRIEVAL ALGORITHM		60
4.1	Rain Contamination Correction	61
4.2	Wind Vector Retrieval Algorithm	69
CHAPTER 5 : ALGORITHM PERFORMANCE EVALUATION & RESULTS.....		74
5.1	Rain Correction Effectiveness	74
5.2	Wind Speed Retrievals.....	81
5.3	Wind Direction Retrievals	91
CHAPTER 6 : SUMMARY & CONCLUSION.....		94
6.1	Summary and Conclusion.....	94
6.2	Future Work	96
APPENDIX A.	SPACE-BORNE ACTIVE MICROWAVE WIND ESTIMATION HISTORY	98

APPENDIX B.	THE SAFFIR-SIMPSON HURRICANE WIND SCALE.....	101
APPENDIX C.	MAXIMUM LIKELIHOOD ESTIMATION.....	102
APPENDIX D.	V-POL TB FIELDS FOR HURRICANE ISABEL.....	105
APPENDIX E.	V-POL WIND DIRECTIONAL SIGNATURE FOR HURRICANE SCENES ISABEL3 & ISABEL4.....	106
APPENDIX F.	V-POL T-FACTOR COMPARISON.....	107
	LIST OF REFERENCES.....	108

LIST OF FIGURES

Figure 2.1 Scatterometer transmitting an EM pulse and measure the power in the return echo. ...	9
Figure 2.2 SeaWinds H-pol GMF for constant wind speed values at 46° incidence angle.	14
Figure 2.3 Measurement geometry for the IWRAP instrument (Courtesy of D. E. Fernandez) [7].	16
Figure 2.4 The saturation behavior of the mean σ^0 for different cases obtained from the IWRAP dual polarized C- and Ku-band GMF (Courtesy of D. E. Fernandez) [7].	17
Figure 2.5 Schematic of conical scanning scatterometer measurement geometry cases: a) swath edge, b) sweet spot (left hand side), and c) near-nadir (satellite ground track).	19
Figure 2.6 Possible wind vector solutions loci for different swath locations: a) Near nadir, b) Swath edge, and c) Mid-swath.	21
Figure 3.1 Illustration of the DFS measurement geometry [8].	27
Figure 3.2 Geometry of scatterometer measurement slices used for wind vector retrievals [8]. .	28
Figure 3.3 Conceptual configuration of the GCOM-W2 mission with DFS and AMSR aboard [38].	30
Figure 3.4 Illustration of the SeaWinds measurement geometry.	34
Figure 3.5 SeaWinds' σ^0 resolution elements.	35
Figure 3.6 WRF simulation of Hurricane Isabel in September 2003 showing (a) wind speed, (b) rain rate, (c) C-band attenuation, (d) C-band RVBS, (e) ku-band attenuation, and (f) Ku-band RVBS.	39
Figure 3.7 (a) a single pulse IFOV with range bins (slices) and (b) DFS IFOVs for the Ku-band outer beam showing along track and along scan overlap.	41

Figure 3.8 DFS antenna patterns for the (a) C- and (b) Ku-band beams.	43
Figure 3.9 The calculated k_p values for various values of H-pol Ku-band σ^0 in dB scale.	44
Figure 3.10 DFS σ^0 simulation top-level block diagram.	45
Figure 3.11 Calculating antenna brightness temperatures at the center of the IFOV for AMSR channels.	46
Figure 3.12 H-pol Tb fields on a latitude/longitude grid, for hurricane Isabel in September 2003. Right side panels (a, c, and e) show the original high resolution Tb fields, and the left side panels (b, d, and f) show the averaged Tb fields over the antenna pattern for 6, 19, and 89 GHz AMSR channels respectively.	48
Figure 3.13 H-pol Wind directional signature for hurricane scenes Isabel3 (left panels) and Isabel4 (right panels). Upper panels [(a) and (b)] give the simulated results, and lower panels [(c) and (d)] give the SeaWinds measurements from ADEOS-II.	53
Figure 3.14 H-pol Cross-correlations between real ADEOS-II active and passive observations hurricane signatures at the top of atmosphere (upper plots) and simulated observations (lower plots).	55
Figure 3.15 Calculated correlation coefficients from the measured parameters (red stars) and the simulated parameters (blue diamonds) for H-pol AMSR channels.	57
Figure 3.16 Hurricane Isabel σ^0 values at the top of the atmosphere compared with surface wind speeds for panel-(a) simulated observations, and panel-(b) SeaWinds on ADEOS-II observations.	58
Figure 4.1 Multilinear regression procedure implemented in the rain correction.	62

Figure 4.2 Stepwise regression procedure [from Wikipedia: http://en.wikipedia.org/wiki/File:Stepwise.jpg].	64
Figure 4.3 H-pol T-factor comparison using (a) AMSR H-pol Tb's only, (b) AMSR H- and V-pol Tb's, and (c) AMSR H- and V-pol Tb's with C-band σ^0 measurements.	68
Figure 4.4 OVW retrieval process block diagram.	70
Figure 4.5 Grouped IFOV slices (filled with green color) with portions falling within the WVC boundaries (red box) showing the Gaussian weighting scheme applied.	71
Figure 4.6 MLE objective function. a) 3-D active/passive (RadScat) MLE residue surface in dB, b) 2-D residue contours with ranked wind vector aliases.	72
Figure 4.7 GCOM-W2 end-to-end simulation block diagram.	73
Figure 5.1 Isabel2 hurricane case for H-pol ku-band (a) surface σ^0 truth field, (b) σ^0 field at the top of the atmosphere (no correction applied), (c) estimated T-factor, and (d) the corrected σ^0 surface field using the estimated T-factor.	76
Figure 5.2 Isabel5 hurricane case for H-pol ku-band (a) surface σ^0 truth field, (b) σ^0 field at the top of the atmosphere (no correction applied), (c) estimated T-factor, and (d) the corrected σ^0 surface field using the estimated T-factor.	77
Figure 5.3 Isabel6 hurricane case for H-pol ku-band (a) surface σ^0 truth field, (b) σ^0 field at the top of the atmosphere (no correction applied), (c) estimated T-factor, and (d) the corrected σ^0 surface field using the estimated T-factor.	78
Figure 5.4 Isabel5 H-pol ku-band σ^0 differences (dB) when (a) no correction is applied, and (b) when T-factor correction is applied.	80

Figure 5.5 Isabel5 H-pol ku-band differences when (a) no correction to the σ^0 is applied, and (b) when T-factor correction is applied.	81
Figure 5.6 Isabel5 surface wind speeds: (a) WRF wind field, (b) conventional C-band retrievals, (c) conventional Ku-band retrievals, and (d) the rain corrected Ku-band retrievals.	82
Figure 5.7 Isabel6 surface wind speeds: (a) WRF wind field, (b) conventional C-band OVW retrievals, (c) conventional Ku-band OVW retrievals, and (d) the rain corrected Ku-band OVW retrievals.	83
Figure 5.8 Isabel5 case for (a) conventional Ku-band wind speed retrievals errors, (b) rain corrected Ku-band wind speeds retrievals error, (c) conventional Ku-band wind speed scatter plot, and (d) rain corrected Ku-band wind speed scatter plot.	85
Figure 5.9 Isabel5 case for (a) conventional Ku-band wind speed retrieval errors, (b) rain corrected Ku-band wind speeds retrieval error, (c) conventional Ku-band wind speed scatter plot, and (d) rain corrected Ku-band wind speed scatter plot.	86
Figure 5.10 Isabel5 case for (a) east/west and (b) north/south radial cuts through the storm. Solid black line represents WRF wind speeds, blue solid line represents conventional Ku-band retrieved wind speeds, red solid line represents rain corrected Ku-band retrievals.	88
Figure 5.11 RMSE surface as a function of wind speed (m/s) and rain rate (mm/h)	89
Figure 5.12 Wind speed retrieval error statistics for conventional Ku-band speed retrievals and rain corrected Ku-band speed retrievals.	91
Figure 5.13 Wind direction comparison between WRF surface truth and (a) the conventional Ku-band retrievals, and (b) the rain corrected Ku-band retrievals.	92
Figure A.1 Spaceborne wind measuring scatterometers sponsored by NASA and ESA.	100

Figure D.1 V-pol Tb fields on a latitude/longitude grid, for hurricane Isabel in September 2003. Right side panels (a, c, and e) show the original high resolution Tb fields, and the left side panels (b, d, and f) show the averaged Tb fields over the antenna patten 105

Figure E.1 V-pol Wind directional signature for hurricane scenes Isabel3 (left panels) and Isabel4 (right panels). Upper panels [(a) and (b)] give the simulated results, and lower panels [(c) and (d)] give the SeaWinds measurements from ADEOS-II..... 106

Figure F.1 V-pol T-factor comparison using (a) AMSR V-pol Tb's only, (b) AMSR V- and H-pol Tb's, and (c) AMSR V- and H-pol Tb's with C-band σ^0 measurements..... 107

LIST OF TABLES

Table 3.1 Summary of DFS sampling and performance requirements.....	29
Table 3.2 Operating characteristics of AMSR.....	32
Table 3.3 List of simulated hurricane scenes.....	51
Table 4.1 H-pol T-factor Combinations.....	63
Table 4.2 V-pol T-factor Combinations.....	63
Table 4.3 Stepwise Regression Analysis Output	65
Table 4.4 R2 comparison of T-factor model.....	66
Table 5.1 Wind speed comparisons for different wind speed bins	90
Table A.1 Characteristics of space-borne wind scatterometers.....	100
Table B.1 Saffir-Simpson Hurricane Scale.....	101

LIST OF ACRONYMS / ABBREVIATIONS

ADEOS	Advanced Earth Observing Satellite
AMSR	Advanced Microwave Scanning Radiometer
ASCAT	Advanced Scatterometer
CDR	Climate Data Record
CFRSL	Central Florida Remote Sensing Laboratory
CPHC	Central Pacific Hurricane Center
DFS	Dual Frequency Scatterometer
DMSP	Defense Meteorological Satellite Program
DSD	Drop Size Distribution
ECMWF	European Centre for Medium-Range Weather Forecasting
ERS	European Remote Sensing Satellite
EM	Electromagnetic
ESA	European Space Agency
GCOM	Global Change Observation Mission
GCOM-W2	Global Change Observation Mission-Water Cycle
GMF	Geophysical Model Function
HRD	Hurricane Research Division
IFOV	Instantaneous-field-of-view
JAXA	Japan Aerospace Exploration Agency
JPL	Jet Propulsion Laboratory

JTWC	Joint Typhoon Warning Center
L2A	QuikSCAT Level 2A
L2Ao	AMSR Level 2A Overlay
L2B	QuikSCAT Level 2B
MetOp	Meteorological Operational
MLE	Maximum Likelihood Estimation
MUDH	Multidimensional Histogram
NASA	National Aeronautics and Space Administration
NCEP	National Centers for Environmental Prediction
NESDIS	National Environmental Satellite, Data, and Information Service
NHC	National Hurricane Center
NOAA	National Oceanic and Atmospheric Administration
NRCS	Normalized Radar Cross Section
NRL	Naval Research Laboratory
NSCAT	NASA Scatterometer
NWP	Numerical Weather Prediction
NWS	National Weather Service
OVW	Ocean Vector Winds
QuikSCAT	Quick Scatterometer
SFMR	Stepped Frequency Microwave Radiometer
SNR	Signal-to-noise Ratio
SSM/I	Special Sensor Microwave/Imager

SST	Sea Surface Temperature
STD	Standard Deviation
Tb	Brightness Temperature
TC	Tropical Cyclone
TMI	TRMM Microwave Imager
TPC	Tropical Prediction Center
TRMM	Tropical Rainfall Measuring Mission
WRF	Weather Research and Forecast
WVC	Wind Vector Cell

CHAPTER 1 : INTRODUCTION

As the largest source of momentum for the ocean surface, winds affect the full range of ocean movement from individual surface waves to complete current systems. They also regulate the interaction between the atmosphere and the ocean via modulating the air-sea exchanges of heat, moisture, and gases. Moreover, ocean vector winds (OVWs) can reach destructive force in extreme weather events, known as tropical cyclones (TCs), causing one of the most severe weather phenomena on earth that is devastating to human livelihood and economy.

Currently, TCs are an actively researched topic of great interest to policymakers and the scientific community at large [1]. For instance, in the United States, TCs are monitored by several federal governmental organizations under the lead of the National Oceanic and Atmospheric Administration (NOAA), including the Tropical Prediction Center/National Hurricane Center (TPC/NHC), Central Pacific Hurricane Center (CPHC), Weather Forecast Office (WFO), and Joint Typhoon Warning Center (JTWC). They all try to predict the storm path and intensity to issue accurate and timely warnings to those in harm's way.

In this introductory chapter, applications of scatterometers in TCs are discussed along with their limitations and the expectations from future scatterometer missions.

1.1 Scatterometers Applications and Limitations in Tropical Cyclones

Over the past decade, forecasters have come to rely more on satellite remote sensing to help filling the gaps between conventional observations from buoys and sea ships over the vast open ocean areas. Along with other remotely sensed data used to study TCs (from over flights by reconnaissance aircraft), the satellite scatterometer measurements of OVW close to the ocean surface have proved to be exceedingly useful and have revolutionized operational weather and storm forecasting and modeling [2, 3].

Currently, spaceborne scatterometers OVW measurements are an intrinsic part of everyday forecasting and warning processes associated with TCs or any wind driven sea condition. They have achieved high accuracy for synoptic ocean wind conditions and have provided complementary information about the ocean/atmosphere boundary conditions under all-weather, day/night conditions with high spatial and temporal sampling and global coverage. For instance, data products from previous and current satellite scatterometer systems are integrated into the numerical weather prediction (NWP) models at the National Center for Environmental Prediction (NCEP). In addition, they are routinely assimilated into NWP modeling centers all around the world, such as the European Centre for Medium-Range Weather Forecasting (ECMWF) [4].

Despite all the success that scatterometers have achieved, their OVW estimates have limitations, which impede the delineation of the fine scale structure associated with TCs [5]. These limitations are linked to the sensors characteristics and can be summarized as follows [6]:

- Uncertainty in the radar measurements due to rain contamination
- Measured ocean σ^0 at Ku-band begins to saturate beyond wind speeds of approximately 30 m/s and eventually decreases at speeds around 50 m/s
- Instrument spatial resolution is not adequate to resolve small-scale storm structure associated with extreme wind events.

Future improved active/passive microwave satellite sensors offer the potential to overcome the current observation limitations and provide valuable information to describe the sea state structure related to the intensity of the surface winds. Such a combined consistent analysis can be essential to issue more precise forecasting, and help to propose a more consistent view of the storm structure and intensity.

1.2 Future Scatterometer Missions Requirements

In 2006, the NOAA operational community experience with then currently available satellite OVW measurements culminated in the formulation of new operational OVW requirements. These requirements reflect the observational needs of forecasters to prepare warnings and

forecasts for a variety of meteorological and oceanographic phenomena observed over the oceans including TCs.

Thus, “NOAA Operational Satellite Ocean Surface Vector Winds Requirements” workshop held in Miami Florida in 2006 [6], resulted in a generation of a consensus set of measurement requirements. These requirements, summarized below, are more stringent than the measurements capabilities of current instruments and are expected to become the guideline for the design of future operational OVW measurement systems:

- Improvements in the spatial resolution of the data on the order of a few kilometers. This performance improvement would increase coverage in coastal regions (currently unavailable within 20 km of the coast), and better resolve critical physical processes in tropical cyclones.
- All-weather coverage, including coverage under heavy rain typical of TCs.
- Very high wind speed retrievals including winds in TCs. Currently, retrievals are limited in its wind speed range due to saturation of the Ku-band “model function” (the empirical relation between the radar measurements and vector winds) at high wind speeds [7].
- Improving the temporal revisit characteristics by maintaining wide instrument swath.

In order to best meet the requirements set while maintaining the high level of heritage and validation required for an operational mission, a conceptual instrument design called the Next-generation Ocean Vector Wind Mission (XOVWM) was proposed. The instrument concept

includes both active and passive measurements, where the components and the rationale for their inclusion are the following [6]:

- Ku-band synthetic aperture radar (SAR) scatterometer: Ku-band SAR scatterometry presents the only method for achieving high spatial resolution with a moderate size antenna.
- C-band Real Aperture scatterometer: C-band is required for minimizing rain effects.
- Multi-frequency polarimetric radiometer: required for providing rain corrections and improving wind speed estimation and rain correction.

The system proposed by the XOVWM provides a significant enhancement over current instrument capabilities making the next-generation concept an attractive candidate for providing the first step towards an operational mission, which will meet the science community requirements.

1.3 Dissertation Objectives

This dissertation describes the development of a novel active/passive OVW retrieval algorithm for the next generation scatterometer missions. The architecture of this new algorithm uses the higher spatial resolution of the Ku-band scatterometer measurements to infer ocean surface winds in TC's. The multi-frequency microwave radiometer and C-band scatterometer provide

rain correction for the Ku-band backscatter observations to enable accurate wind retrievals in the presence of strong tropical rainfall.

The algorithm is based on the instrument conceptual design of the next generation Dual Frequency Scatterometer (DFS) developed by National Aeronautics and Space Administration's (NASA) Jet Propulsion Laboratory (JPL) [8]. With the Advanced Microwave Scanning Radiometer (AMSR) sharing the platform with the DFS, the simultaneous C- and Ku-band DFS measurements, with the collocated radiometer observations will provide an exceptional data set for the purpose of this dissertation.

The synergy of these active and passive instruments is anticipated to greatly improve the accuracy of the OVW retrievals, and therefore, enhance the usefulness of Ku-band scatterometer measurements in extreme wind events. Horizontally polarized (H-pol) C-band measurements provided by the DFS, which have been shown to be less susceptible to rain contamination, will be exploited along with the multi-frequency passive observations to correct the rain contamination effects on the higher resolution Ku-band measurements.

The remainder of this dissertation is organized as follows. In Chapter 2, a description of OVW measurements in extreme wind events, and the effects of rain on scatterometer measurements is presented. Chapter 3 provides an overview on the instruments, datasets, and numerical weather model used in the algorithm development and simulation evaluation. Chapter 4 describes the development the new active/passive OVW retrieval algorithm. Then, in Chapter 5, the algorithm

performance evaluation and results are presented. Finally, conclusions and a discussion of future work are given in Chapter 6.

CHAPTER 2 : ACTIVE REMOTE SENSING OF OCEAN WINDS

Active remote sensing instruments, or radars, provide their own source of electromagnetic (EM) radiation to illuminate the object under observation. During World War II, it was noted that radar measurements of ships and low-flying aircraft over the oceans contained background noise or “sea clutter”. An intensive airborne radar research program conducted by the Navy (and later NASA) in the 1960-70’s, led to the discovery that this sea clutter was related to the local instantaneous wind velocity over the ocean surface. This discovery promoted active remote sensing technology development that introduced a new type of radar designed specifically to measure this type of ocean backscatter, which is known as a microwave scatterometer [9].

Today, scatterometers are employed to observe global ocean surface winds from space with high spatial and temporal sampling, which is crucial for operational numerical weather prediction and many scientific applications in oceanography, meteorology, and global climate change.

In this chapter, a detailed description of space-borne radar scatterometers will be provided to better understand the remote sensing of ocean vector winds from space. Moreover, we will discuss the factors that determine the surface wind measurement accuracy and the major shortcomings that limit scatterometer performance especially in extreme weather events with intense rain rates.

2.1 Space-borne Scatterometers

Satellite scatterometers are spaceborne mono-static radar remote sensors that are designed to measure OVW on a global scale. They transmit EM pulses to the Earth's surface and measure the absolute power in the return echo after being scattered by the wind-roughened ocean surface and experiencing two-way propagation effects within the intervening atmosphere as illustrated in Fig. 2.1.

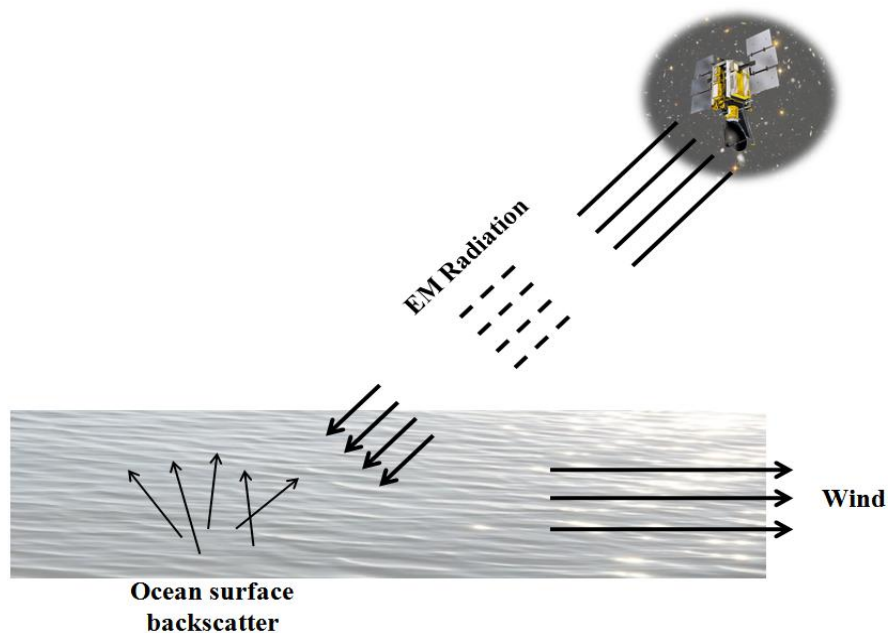


Figure 2.1 Scatterometer transmitting an EM pulse and measure the power in the return echo.

The scattered radiation will occur in all directions as determined by the laws of physics and electromagnetic scattering theory [10, 11]. The returned power (backscattered power, P_r) is of a special interest and is related to the radar parameters via the fundamental radar equation [12]:

$$P_r = \frac{P_t G^2 \lambda^2}{(4\pi)^3 R^4} \sigma \quad (2.1)$$

where R is the distance to the earth (range), G is the antenna gain, λ is the electromagnetic wavelength, and σ is the radar cross section of an isolated point target.

For earth remote sensing purposes, the radar equation must be modified because the earth's surface is a distributed target where many scatterers contribute simultaneously to the total echo power. Thus, equation (2.1) must be modified to account for the instantaneous scattering surface area (or scattering volume in the atmosphere) defined by the transmitted radar pulse and the antenna beam dimensions.

Thus, for ocean backscatter, the radar cross section σ will be replaced by the instantaneous illuminated area (A_{eff}) of the surface multiplied by the ocean reflection coefficient also known as the normalized radar cross section (σ^0), as shown in (2.2).

$$\sigma = \sigma^0 \times A_{eff} \quad (2.2)$$

The A_{eff} is approximately a rectangular “pulse footprint” defined by the radar antenna beam width in azimuth and the radar pulse illumination (range resolution) in range. This is calculated as

$$A_{eff} = \left(\frac{c\tau}{2}\right) 2R \tan\left(\frac{\beta}{2}\right) \sec(\psi) \quad (2.3)$$

where c is the speed of light, τ is the radar pulse width in seconds, β is the antenna half-power beamwidth in azimuth (cross-range direction), and ψ is the grazing angle of the instantaneous line-of-sight with the ocean surface.

The ocean σ^0 is affected by several geophysical parameters, which are generally unknown; but it is possible to determine this quantity by inverting (2.1) to calculate σ^0 from measured P_r , as:

$$\sigma^0 = \frac{(4\pi)^3 R^4}{PtG^2\lambda^2 A_{eff}} Pr \quad (2.4)$$

In microwave scatterometry, the measurement of ocean σ^0 is used to infer near-surface winds. Increasing wind stress at the ocean surface will monotonically increase the σ^0 values and thereby the backscattered power. This process is dominated by Bragg scattering due to centimeter wavelength capillary ocean waves, which respond near-instantaneously to the strength of the local surface wind [13-15]. Moreover, the ocean radar backscatter is anisotropic with the wind direction that enables radars to measure ocean wind vector (speed and direction) [16].

2.2 The Geophysical Model Function

Scatterometer ocean backscatter observations with simultaneous surface wind measurements have been used to establish a robust empirical relationship, known as the geophysical model function (GMF), between the ocean surface normalized radar backscatter σ^0 and the friction wind velocity at the air/sea interface [17-19]. This echo power is modulated by ocean capillary waves, which are in equilibrium with the wind stress, or momentum flux, at the sea surface. The momentum flux is driven by turbulence generated by wind shear and depends on the stability of the atmosphere [20].

However by convention, users prefer the winds measured at the standard height of 10 m above the surface. Because the vertical wind profile depends upon the stability of the atmosphere, which is generally not known, this makes the desired translation difficult to perform. Fortunately, for the majority of ocean observations the air and sea physical temperature are approximately equal, which defines the neutral atmospheric stability logarithmic profile. Therefore, the OVW science community has agreed that scatterometers should report the equivalent neutral stability OVW at 10-m altitude (U_{10}) [21].

If the user desires the actual wind at some other height, then the scatterometer 10m neutral stability wind speed is translated to the surface along the neutral profile and then moved to the desired height along the actual wind profile that exists at the point of measurement. By knowing the air and sea temperature, then the actual wind can be uniquely related to the theoretical parameter U_{10} [21].

Thus, for a specific polarization (p), frequency (f), and earth incidence angle (θ), the GMF is a function of neutral stability 10m wind speed (ws) and relative wind direction to antenna azimuth (χ) as expressed in (2.5). Frequently, modelers have used a simple analytical expression for σ^0 in dB as a three-term Fourier cosine series of ws and χ as shown in (2.6).

$$\sigma_{GMF}^0 = GMF_{p,f,\theta}(ws, \chi) \quad (2.5)$$

$$\sigma^0 = C_0(ws) + C_1(ws) \cos(\chi) + C_2(ws) \cos(2\chi) \quad (2.6)$$

For satellite scatterometers, the coefficients C_0 , C_1 , and C_2 are determined empirically by correlating observed σ^0 values with known surface wind fields (typically from numerical weather models). Often, the GMF are tabulated using averaged σ^0 values over wind speed and relative wind direction bins [22, 23]. For light to moderate winds, this approach is effective, but the resulting GMFs are less well defined for high wind speeds (> 20 m/s) due to the small number of occurrences and the lack of fidelity in numerical models for these extreme wind events.

An example of the SeaWinds H-pol GMF is plotted in dB in Fig. 2.2 for constant wind speed values (10-50 m/s, in 10 m/s steps) over the full 360° range of χ . Note that the GMF is anisotropic in χ (even function around 180°) with σ^0 having maxima at upwind ($\chi = 0^\circ$) and downwind ($\chi = 180^\circ$) and minima near crosswind ($\chi = 90^\circ$ and 270°).

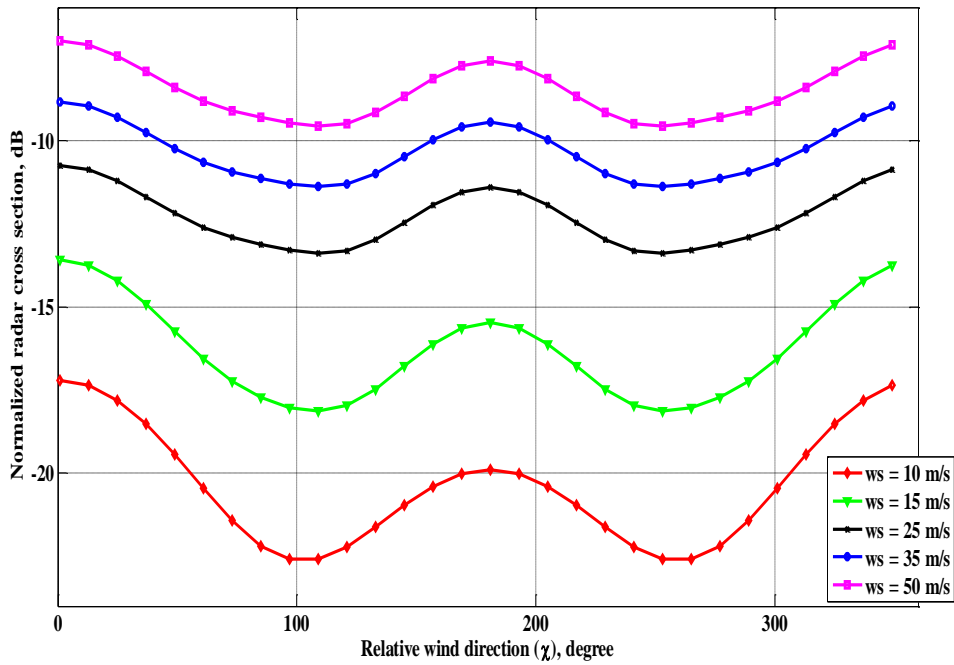


Figure 2.2 SeaWinds H-pol GMF for constant wind speed values at 46° incidence angle.

This anisotropy characteristic of σ^0 forms the basis for the measurement of wind direction by scatterometers. The anisotropy amplitude increases with increasing incidence angle and is typically larger for H-pol than for vertical polarization (V-pol) σ^0 values. Furthermore, the mean σ^0 [$C_0(ws)$] follows an approximately power-law relationship with wind speed up to ~ 30 m/s after which it slowly saturates until it reaches its maximum value near 50 m/s.

Moreover, there is also a small but significant difference in σ^0 magnitude between upwind and downwind angles (known as the "upwind-downwind asymmetry"), with upwind cross sections being typically larger than downwind. The upwind-downwind asymmetry ($\cos(\chi)$ term) increases with increasing incidence angle, is larger for H-pol than for V-pol, and is larger at lower wind speeds. Although small, this upwind/downwind asymmetry is critical; and in its absence,

scatterometer vector wind retrievals would always result in a 180° ambiguity in direction (i.e., it would not be possible to determine whether the wind was blowing "from" or "to" a given direction). Because of this asymmetry, it is possible, in principle, to determine a unique wind vector, although the small magnitude of the asymmetry requires that high precision measurements of σ^0 be obtained [24].

During the late 1990's and early 2000's, the University of Massachusetts (UMASS) participated in many NOAA Hurricane Research Division research/reconnaissance flights, and airborne dual-frequency scatterometer data were obtained to develop improved C- and Ku-band GMFs for hurricane force winds. In particular, during the 2002 and 2003 hurricane seasons, dual polarized C- and Ku-band σ^0 measurements were simultaneously collected in hurricanes (up to 65 m/s wind speeds) with the UMASS Imaging Wind and Rain Airborne Profiler (IWRAP), a high-resolution dual-band dual-polarized conically scanning airborne Doppler radar illustrated in Fig. 2.3.

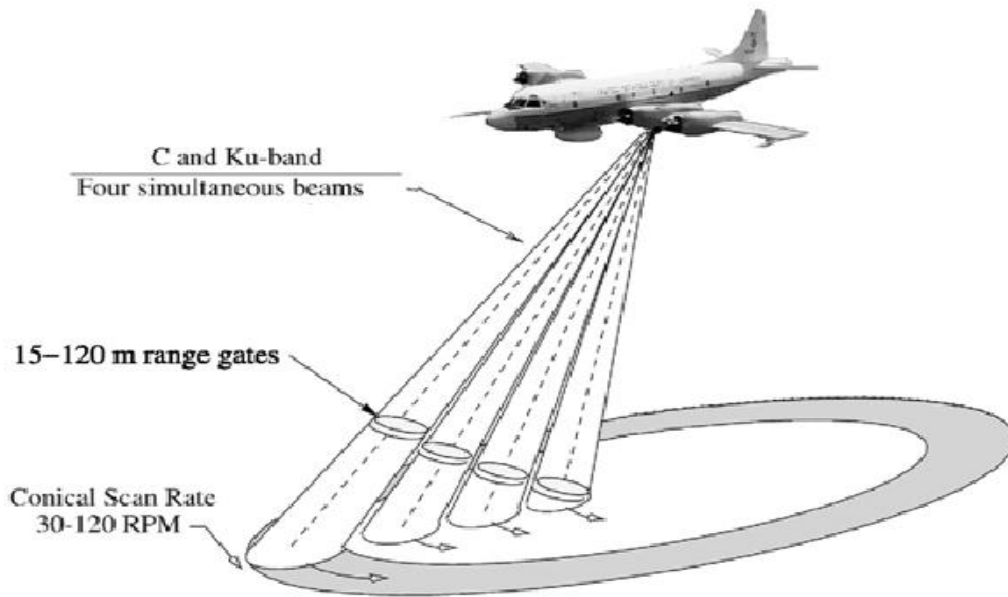


Figure 2.3 Measurement geometry for the IWRAP instrument (Courtesy of D. E. Fernandez) [7].

These experiments were significant in that for the first time extremely high wind speeds were observed with associated high quality surface truth surface wind measurements. As a result of these observations, Fernandez et. al. [7] discovered that σ^0 measurements at Ku-band saturate at wind speeds of about 50 to 55 m/s at both polarizations and for all incidence angles. Also, it was observed that the σ^0 would even decrease at higher wind speeds, which had never been observed before. On the other hand, for C-band measurements, particularly at horizontal polarization and high incidence angles, the saturation in the wind speed was not reached even at wind speeds as high as 65 m/s. Figure 2.4 summarizes the saturation behavior of the mean σ^0 for different cases obtained from the IWRAP dual polarized C- and Ku-band GMF that is used in this dissertation.

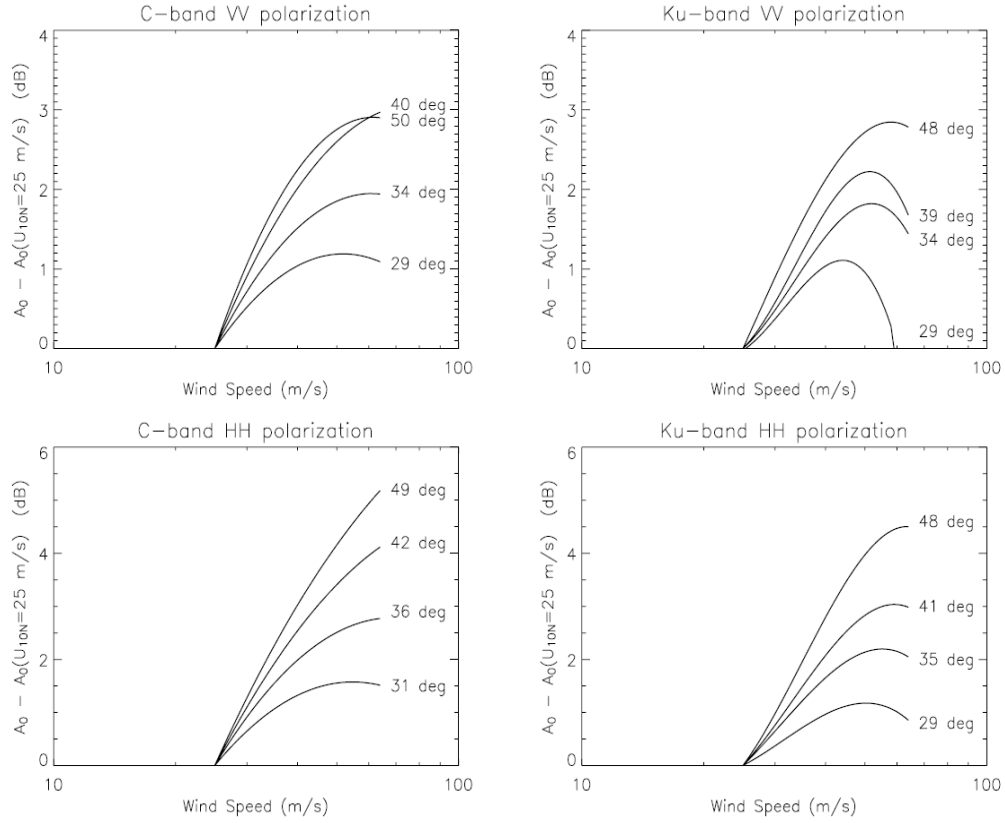


Figure 2.4 The saturation behavior of the mean σ^0 for different cases obtained from the IWRAP dual polarized C- and Ku-band GMF (Courtesy of D. E. Fernandez) [7].

2.3 Estimation of Wind Velocity from Scatterometer Measurements

Estimation of ocean wind velocity from σ^0 measurements involves inversion of the scatterometer GMF. The conventional approach [24] utilizes the maximum likelihood estimation (MLE) of wind velocity based on minimizing the difference between the measured and the modeled σ^0 (σ_{GMF}^0) (see Appendix C). However, for a single σ^0 measurement, no unique solution exists; and a single backscatter measurement is not sufficient to solve for both wind speed and wind direction. Thus, for satellite scatterometers, σ^0 observations of the ocean surface, obtained from different antenna azimuth looks known as “flavors” (i.e., pointing forward and aft from the

satellite location), are usually grouped into latitude/longitude boxes (called wind vector cells, WVCs). These grouped multi-look σ^0 observations are then processed using an OVW retrieval algorithm to infer neutral stability wind vectors at 10-m height above the sea surface.

Because of the bi-harmonic nature of the GMF, multiple possible wind vector solutions, also called “aliases”, may occur [24, 25]. The best solutions that are statistically consistent with all the collocated σ^0 values are computed *via* a simplified MLE objective function (ζ) as expressed in (2.7) [24], see Appendix-C.

$$\zeta = \sum_{i=1}^n \frac{(\sigma_{i,meas}^0 - \sigma_{GMF}^0(ws, \chi))^2}{Variance_{\sigma_{meas}^0}} \quad (2.7)$$

This method generates solutions by identifying wind speed and direction pair(s) that minimizes the sum of the square of the differences between the “ n ” radar backscatter measurements and the scatterometer GMF after being normalized by their corresponding estimated variance.

For conical scanning satellite instruments (e.g. SeaWinds, Dual Frequency Scatterometer), the azimuth diversity, as illustrated in Fig. 2.5, causes the retrieval error to vary systematically with cross-track location in the swath. For example, minimum errors are located symmetrically about the sub-track in the mid-swath regions, or “sweet spots”, where azimuth diversity in the measured σ^0 values is optimized. On the other hand, the largest errors occur at the swath edges

(small azimuthal differences in radar looks) and along the satellite sub-track where forward and aft measurements are 180° apart [26].

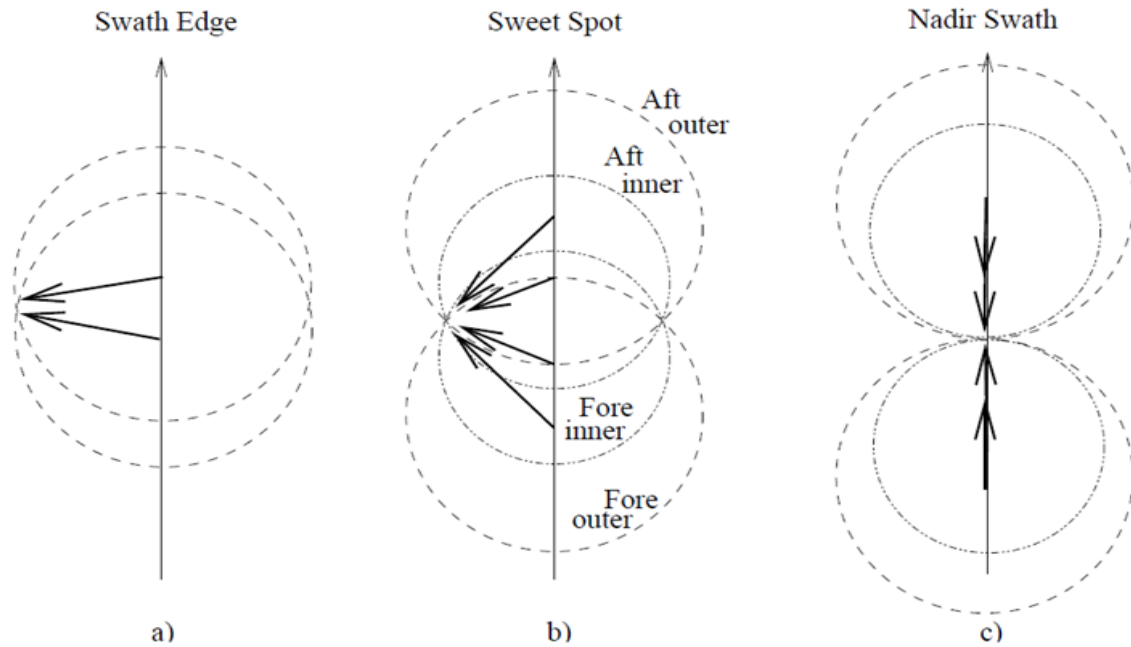
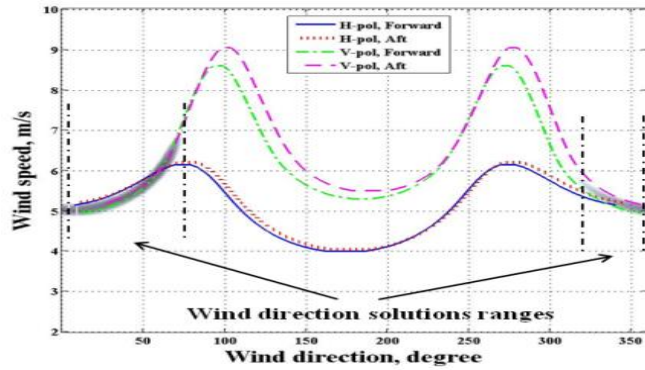


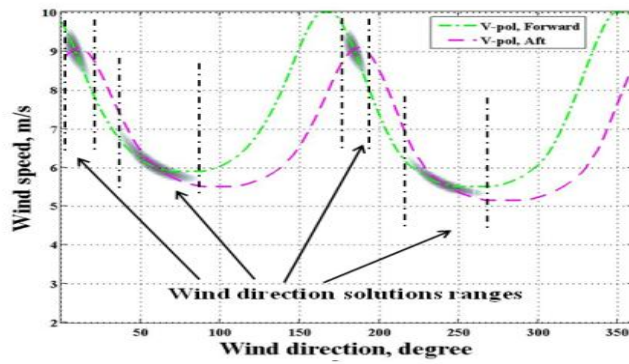
Figure 2.5 Schematic of conical scanning scatterometer measurement geometry cases: a) swath edge, b) sweet spot (left hand side), and c) near-nadir (satellite ground track).

From the OVW retrievals perspective, the effects of azimuth diversity is illustrated in Fig. 2.6, where each curve represents the loci of possible wind speed and direction pairs associated with a single noise-free σ^0 measurement of a given flavor. Note that each curve has a quasi-sinusoidal shape, which is shifted according to the corresponding azimuth for that particular measurement. Possible wind vector solutions (up to four aliases) are shown as dark shaded areas, where curves of constant σ^0 intersect. These aliases are ranked according to the inverse of the magnitude of the residue from the objective function in (2.7), i.e., the smaller the residue, the greater the

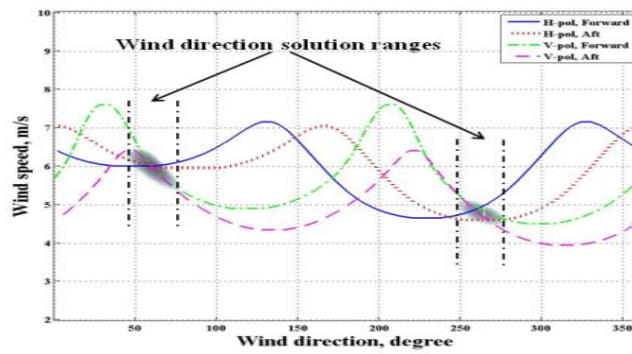
probability that the alias is the “true” ocean surface winds. As noted in panels-a and -b, at the near-sub-track and swath edge, loci intersections usually result in wider range of possible wind direction, while the mid-swath or “sweet-spot” (panel-c) measurements result in a tighter grouping (lower residue) and more probable wind vector solutions.



(a)



(b)



(c)

Figure 2.6 Possible wind vector solutions loci for different swath locations: a) Near nadir, b) Swath edge, and c) Mid-swath.

2.4 Rain Effects on Radar backscatter

The accuracy of ocean wind scatterometers is impacted to varying degrees by rain. In order to assess the effects of rain on OVW retrievals and ultimately to minimize its impact, we must understand the effects of rain.

There are three ways that rain affects σ^0 at the top of the atmosphere. First, the rain column attenuates both the transmitted radar signal and the wind-driven radar echo from the ocean surface. Second, the rain column produces its own volume backscatter (RVBS) due to scattering from rain drops and graupel (ice particles) in the atmosphere [27]. Third, rain striking the ocean roughens its surface, commonly referred to as “splash”, imposing some (possibly highly nonlinear) modulation on the surface backscatter cross section [28].

These rain effects on the measured top of the atmosphere (σ_{wind}^0) can be expressed as in (2.8). This model assumes that: the surface roughness spectrum is a superposition of the rain spectrum and the wind spectrum [29], the atmosphere is modeled with RVBS being an additive term, and the attenuation is expressed as a multiplicative term [30-32].

$$\sigma_{Top\ of\ atm.}^0 = (\sigma_{wind}^0 + \sigma_{se}^0) \times \alpha + \sigma_{rain}^0 \quad (2.8)$$

where $\sigma_{Top\ of\ atm.}^0$ is the measured σ^0 at the top of the atmosphere, σ_{se}^0 is the enhancement of surface backscatter as a result of rain drop impacts, α is the two way attenuation, and σ_{rain}^0 is the additional scattering due to RVBS.

Experiments performed in wind-wave tanks with simulated rain have demonstrated that the nonlinear interaction of rain-induced ring waves and wind-induced capillary waves is a potentially significant error source in wind [28, 29]. However, for high wind speeds in hurricanes, the splash effect is less significant due to the fact that breaking waves and spray caused by wind shearing wave crest are generating many water drops that impact the surface in addition to rain. These surface effects are captured in the empirical IWRAP GMF, whereby both wind and splash effects are included in the σ_{wind}^0 term.

$$\sigma_{Top\ of\ atm.}^0 = (\sigma_{wind}^0) \times \alpha + \sigma_{rain}^0 \quad (2.9)$$

In addition, it is worth mentioning that Ku-band scatterometers (due to their smaller EM wavelengths) are more susceptible to rain contamination than their C-band counterparts. Studies by Tournadre and Morland in 1997 have shown that the attenuation due to rain for a C-band scatterometer is a factor of 13 lower than that for a Ku-band at rain rate of 10 mm/h [33], and the RVBS for a C-band scatterometer can be 16 dB lower than the Ku-band scatterometer for a given

value of rain volume reflectivity factor (Z). Also, scatterometers with higher incidence angles suffer from greater scattering and attenuation due to the increased rain slant path.

Stiles et al. [34] have made several important observations on the impact of precipitation on the Ku-band scatterometer measurements, and can be summarized as follows:

1. *“The impact of rain on the measurements decreases with increasing wind speed.”*
2. *“The effect of rain on σ^0 is primarily increasing. Only the highest wind speed cases show a decrease in σ^0 due to rain attenuation ...”*
3. *“For low wind speeds, even very low rain rates have a significant impact on σ^0 ...”*
4. *“H-pol measurements are more sensitive to rain than the V-pol measurements due to enhanced RVBS ...”*

Although over global oceans rain events are infrequent, they are often associated with significant weather phenomena, and therefore it is important to explore any opportunity to improve scatterometer OVW retrievals in rain. Previously, various rain flags have been applied to scatterometers data, i.e. QuikSCAT, including multidimensional histogram (MUDH) technique [35], the normalized objective function (NOF) technique [31], and others [36]. In this dissertation, we developed a technique that corrects scatterometer measurements for rain effects rather than flagging the rain contaminated pixels.

CHAPTER 3 : ACTIVE/PASSIVE SIMULATION OVERVIEW

DFS and AMSR onboard the GCOM-W2 mission are instruments that have not flown yet. However, their operational and scientific requirements have been defined by JPL (including their instrument design, expected performance, and user impact) to satisfy the OVW science community needs and expectations [37].

Given the above, a high fidelity instrument simulation was developed and used to design an improved OVW retrieval algorithm that meets the OVW science requirements. Our objective was to verify that this simulation could mirror real instruments measurements, therefore realistic geophysical “nature runs” were simulated using the Weather Research and Forecast model (WRF) and used to simulate Ku-band scatterometer and passive microwave observations. The output of the simulation was then compared with real data obtained from the SeaWinds scatterometer and AMSR that were both flown on the ADEOS-II satellite. Results are presented in this chapter.

Moreover, we will provide some necessary background on the instruments design specifications for SeaWinds, AMSR, and DFS, the data products used in the validation, and the WRF model. Finally, we will provide a step-by-step description of the simulation and the validation methodology.

3.1 Instruments

In an effort to establish an operational ocean surface vector wind satellite capability, NASA has been pursuing the opportunity of flying a U.S. scatterometer on board JAXA's GCOM-W2 mission. The GCOM-W is a 13-year mission with three satellites in series, each with 5-year lifetime, and 1-year overlap with follow-on satellites for calibration. The GCOM-W1 and the GCOM-W2 are planned for launch in 2012, and 2016 respectively.

3.1.1 Dual Frequency Scatterometer (DFS)

The Dual Frequency Scatterometer (DFS) has been designed by JPL and proposed as a baseline scanning pencil-beam scatterometer onboard the GCOM-W2 mission [38]. DFS is a major extension to the QuikSCAT design, with the most significant change being the dual frequency operation of C- and Ku-bands and an increased diameter spinning parabolic reflector antenna (2-m), conically rotating at 22 rpm, to acquire ocean measurements over the full 360° field of view. The scanning geometry of the DFS is illustrated in Fig. 3.1. Both frequencies operate at two incidence angles with an inner beam at 49.6° and outer beam at 57.7°. For the C-band (5.4 GHz), both inner and outer beams are H-pol, while for the Ku-band (13.4 GHz) the inner beam is H-pol and the outer beam is V-pol [8].

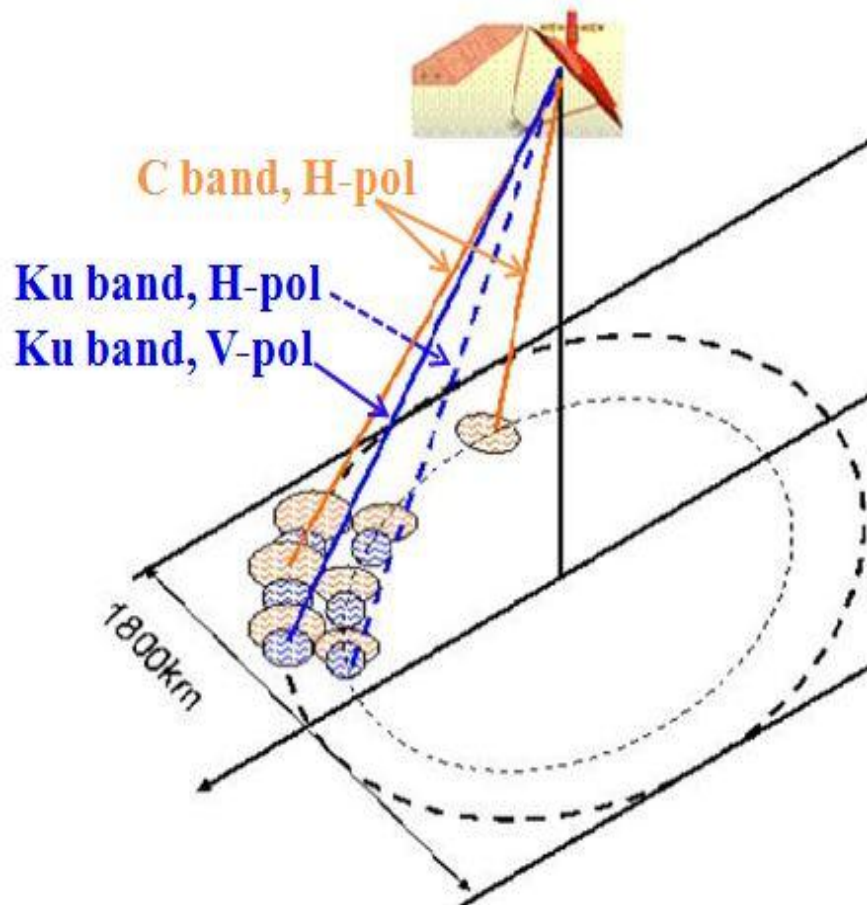


Figure 3.1 Illustration of the DFS measurement geometry [8].

With a 2-m antenna size, the expected resolution of DFS wind vector cells is approximately ~10 km with a 20 % improvement over QuikSCAT. Using range gate processing, the DFS 3-dB antenna footprint on the ocean surface will be comprised of a series of σ^0 “slices” as presented in Fig. 3.2. The spatial resolution of the slices is 3-km in range, and 16-km in azimuth, while for the C-band, it is 3-km in range, and 24-km or 34-km in azimuth for the inner and outer beam respectively [37].

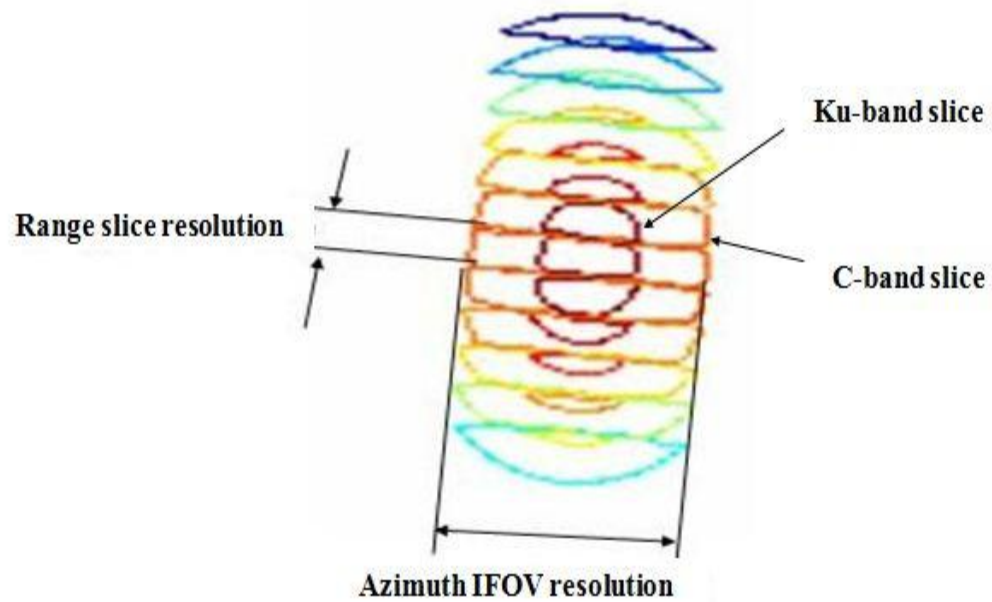


Figure 3.2 Geometry of scatterometer measurement slices used for wind vector retrievals [8].

For ease of reference, Table 3.1 below summarizes the driving performance and sampling characteristics for the DFS [6], and Fig. 3.3 provides an illustration of the GCOM-W2 mission with DFS and AMSR onboard.

Table 3.1 Summary of DFS sampling and performance requirements.

WVC Size	10 km
Coverage	90% of the ocean surface every 24 hours
Wind Speed Accuracy (RMS)	3-20 m/s: 2 m/s 20-30 m/s: 10% 30-50 m/s: 10% 50-80 m/s: 20%
Wind Direction Accuracy (RMS)	3-30 m/s: 20° 30-50 m/s: 20° 50-80 m/s: 30°
Retrieval in Precipitation	Near all-weather wind retrieval
Product Latency	< 180 minutes for 85% of the data

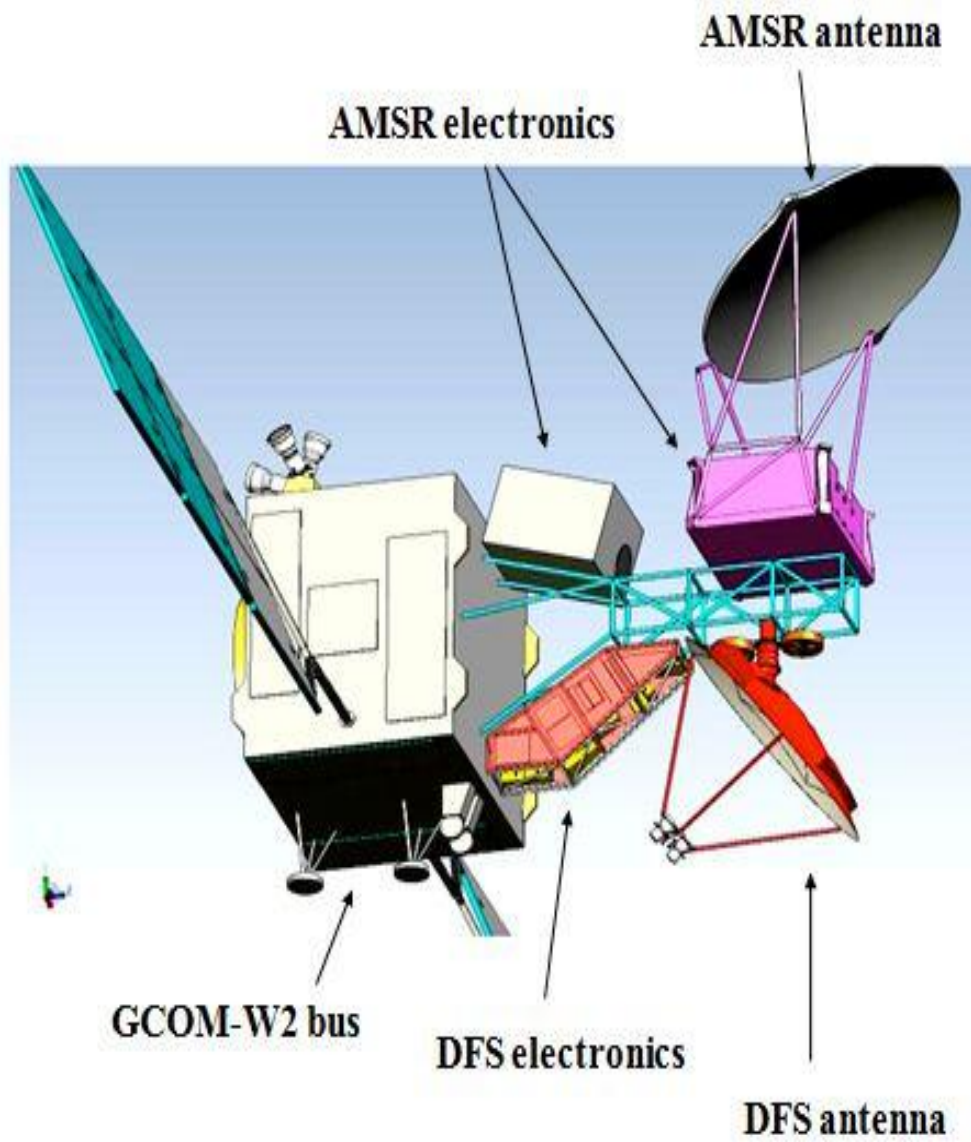


Figure 3.3 Conceptual configuration of the GCOM-W2 mission with DFS and AMSR aboard [38].

3.1.2 Advanced Microwave Scanning Radiometer (AMSR)

JAXA's ADEOS-II mission, also known as Midori-II, was launched in December 2002 and carried five earth observing sensors including AMSR and the SeaWinds scatterometer. An operational anomaly causes the premature termination of the ADEOS-II mission after less than one-year operation. This resulted in AMSR data being available for the first 10 months of 2003 and a combined SeaWinds and AMSR dataset being available from April through October of the same year.

AMSR was an eight-frequency, passive-microwave radiometer system that measured dual polarized (H- and V-pol) radiances at 6.9, 10.65, 18.7, 23.8, 36.5, and 89.0 GHz. AMSR acquired radiance data by conically scanning the Earth's surface to obtain measurements along a semicircular pattern in front of the spacecraft at a fixed earth incidence angle of 55° that results in a wide swath of 1,600 km. The aperture diameter of AMSR's antenna is 2 meters with a spatial resolution of individual measurements that varies from 5 km at 89 GHz to ~50 km at 6.9 and 10.65 GHz channels [39]. Table 3.2 provides summarized operating characteristics of AMSR.

Table 3.2 Operating characteristics of AMSR.

Frequency (GHz)	6.9	10.65	18.7	23.8	36.5	89	50.3	52.8
Bandwidth (MHz)	350	100	200	400	1,000	3,000	200	400
Polarization	H- & V-pol						V-pol	
I FOV (km)	40x70	27x46	14x25	17x29	8x14	3x6	6x10	
Incident angle (degrees)	~ 55°							
Swath width (km)	1600							
Dynamic range (k)	2.7 - 340							

3.1.3 SeaWinds

SeaWinds on ADEOS-II was a Ku-band (13.4 GHz) scatterometer with a conically scanning parabolic reflector antenna operating with two-beams at two different earth incidence angles (outer V-pol beam at 54° and inner H-pol beam at 46°) [40]. The scanning geometry of the SeaWinds scatterometer is illustrated in Fig. 3.4. It obtained σ^0 measurements over the full 360° of azimuth allowing the two pencil beams to sample a wide swath of 1,800 km and 1,400 km for the outer and inner beam respectively as the spacecraft moves along its ground track.

The SeaWinds measurement timing is such that the instantaneous field of view (IFOV) overlap in the along-scan direction by 50%, and the antenna spin rate provides 50% overlap in the along-track direction (scan-to-scan). These IFOVs are limited by the 3-dB antenna power beam width footprint of 24 × 31 km for the inner beam and 26 × 36 km for the outer beam. Furthermore, the IFOVs are subdivided into slices that are approximately 4-km width, as shown in Fig. 3.5.

By means of the SeaWinds design and geometry, σ^0 observations of the ocean surface were grouped into 25-km WVCs. In the overlap region of the two beams, each WVC is sampled with an average of 8-15 σ^0 measurements from different azimuth looks. These grouped multi-look σ^0 measurements or flavors, are relevant for wind direction discrimination and are used in the SeaWinds geophysical retrieval algorithm to infer neutral stability wind vectors at 10-m height above sea surface.

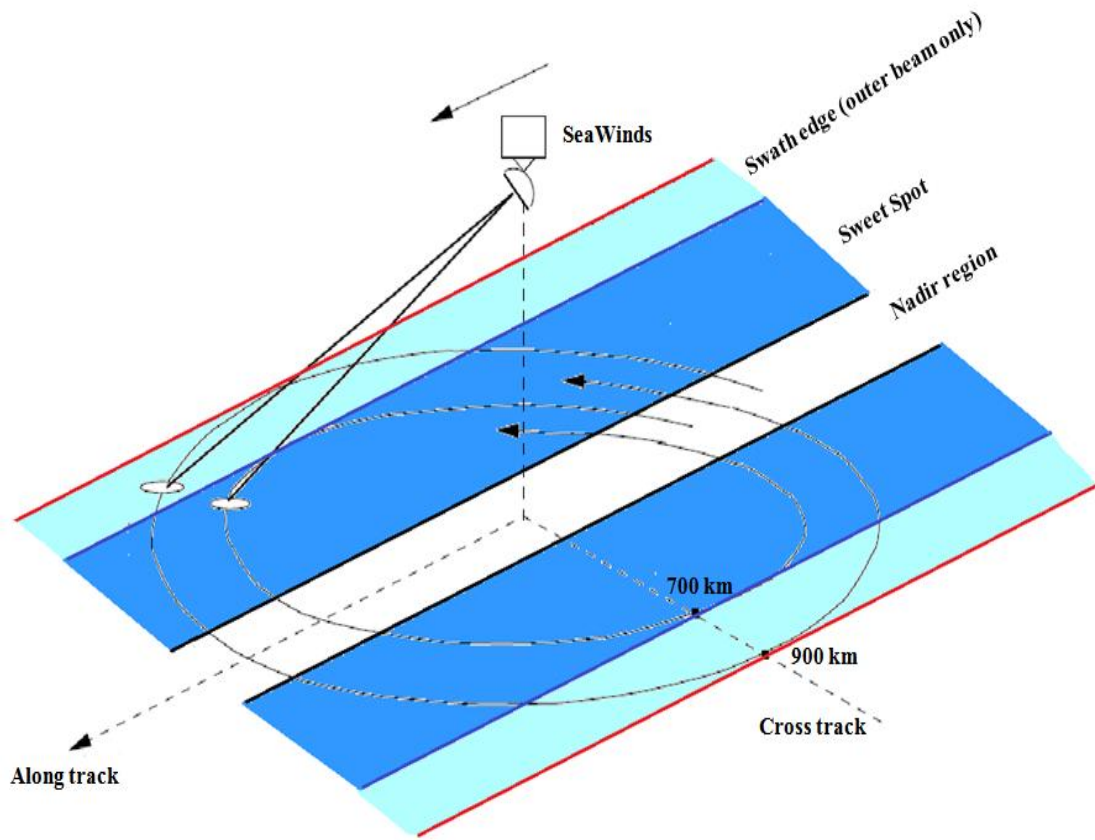


Figure 3.4 Illustration of the SeaWinds measurement geometry.

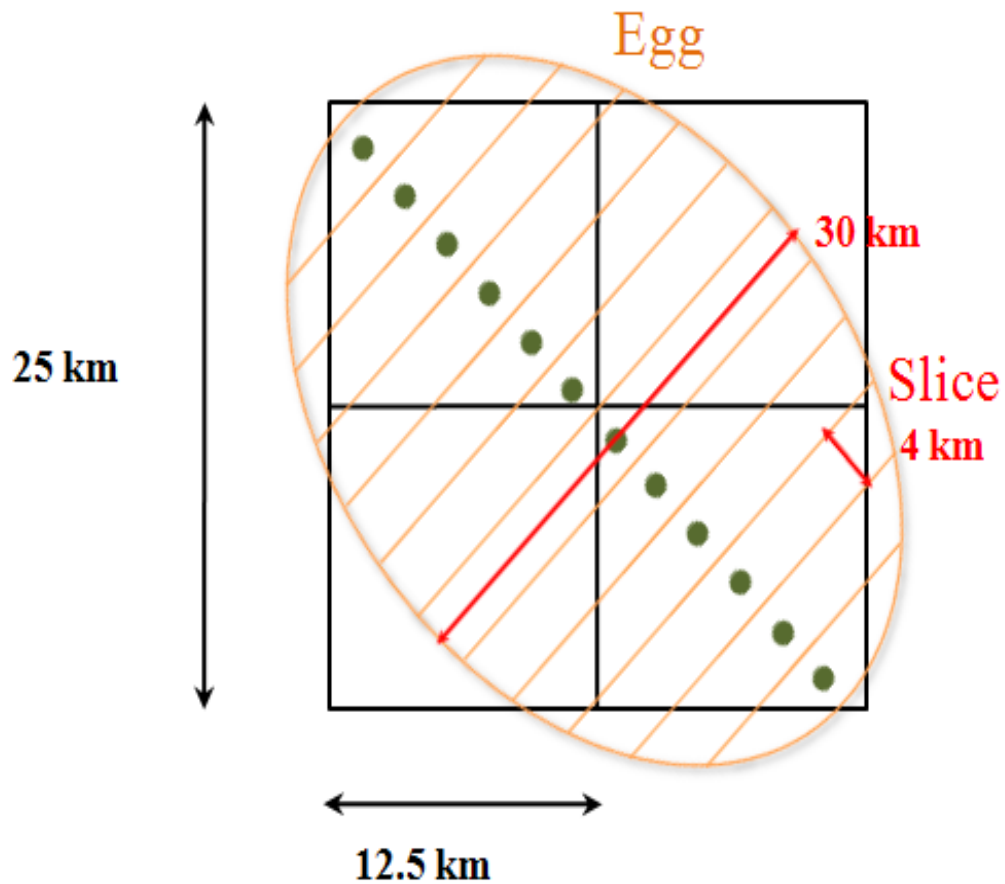


Figure 3.5 SeaWinds' σ^0 resolution elements.

3.2 Data products and Numerical Weather Model

Since the OVW retrieval algorithm developed during this dissertation is based on an instrument conceptual design, it was important to validate the simulated active and passive observations of DFS and AMSR. For this purpose, we utilized real observations from SeaWinds and AMSR onboard ADEOS-II over passing Hurricane Isabel in September 2003. The use of these data products in the validation process is described in the next chapter.

3.2.1 ADEOS-II Data Products

With SeaWinds and AMSR sharing the same platform, their observations were spatially and temporally collocated providing a unique simultaneous active and passive data set, which we used to validate the GCOM-W2 simulation developed under this dissertation. Two data products were used for that purpose corresponding to AMSR level-2A overlay (L2Ao), and SeaWinds level-2A (L2A).

SeaWinds provided measurements on a spacecraft grid of 25 km WVCs located cross-track symmetrically about the ADEOS-II satellite sub-track. In the SeaWinds L2A product, σ^0 measurements were recorded with associated radar parameters along the antenna scan that corresponds to one row of the L2A record, and each satellite orbit corresponds to one L2A file with 1624 rows of data records. L2A data products are obtained from NASA Physical Oceanography Distributed Active Archive Center (PO.DAAC), JPL; and further information can be found at ftp://podaac.jpl.nasa.gov/ocean_wind/seawinds/L2B/doc/.

Furthermore, coincident AMSR L2Ao data contain 12 channels of dual polarized (V- and H-pol) T_b measurements with retrieved geophysical parameters, which were grouped into SeaWinds WVC quadrants. Thus, the data format for the AMSR L2Ao data is a $4 \times 76 \times 1624$ array; however, for SeaWinds L2A product, the data format was slightly different since it contains all of the measurement samples. Using L2A row and column indices, each SeaWinds WVC position (simply called “cell”) could be mapped to the corresponding parameters in the AMSR L2Ao data product.

3.2.2 Weather Research and Forecasting Model

Weather Research and Forecast model (WRF) is a state-of-the-art meteorological model developed collaboratively among several agencies (National Center for Atmospheric Research, National Centers for Environmental Prediction, and Forecast Systems Laboratory) with strong participation from the research community [41]. The WRF modeling system has been designed to study mesoscale and convective scale processes and to provide an advanced mesoscale forecast and data assimilation system for broad use in both research and operations [42].

For hurricanes simulation, WRF high-resolution (1.3 km) 10-m wind and the 3-D precipitation structure geophysical “truth” fields are used. The 3-D precipitation structure divides the lowest 15 km of the atmosphere into 30 vertical layers each with 500-m vertical resolution.

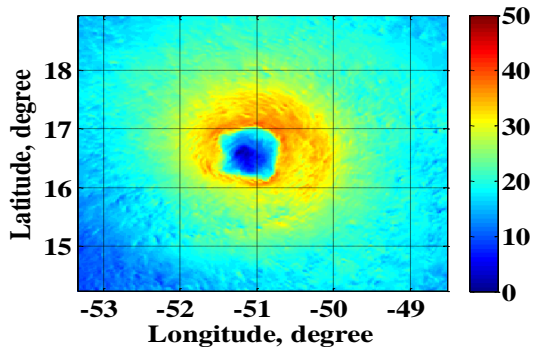
This WRF 3-D precipitation structure was input to a radiative transfer model with Mie-scattering that was used to compute the C- and Ku-band radar atmospheric attenuation, the rain volume backscatter, and the AMSR dual-polarized brightness temperatures.

The scattering properties of hydrometeors were taken into consideration as follows: 1) the number of hydrometeors per unit volume; 2) the size distribution of the hydrometeors; 3) the physical state of the hydrometeors (ice or water, temperature); 4) their shape; and 5) if asymmetrical, their aspect with respect to the radar [43]. In the WRF simulation, spherical particles were assumed with distributions that decrease exponentially with particle size. The

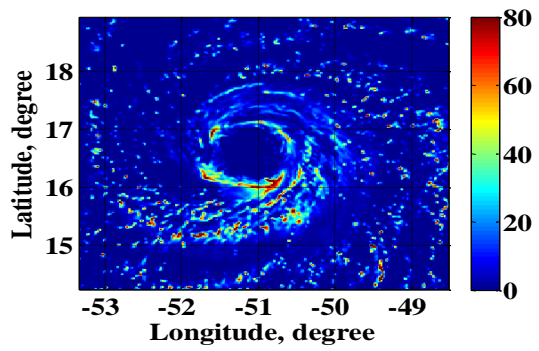
specific distributions utilized are functions of precipitation intensity and type in which the frequency of occurrence decreases with increasing drop size.

For the simulation performed in this dissertation, JPL provided high-resolution (1.3 km) geophysical truth fields (WRF nature runs) that included 10m wind speeds and directions, atmospheric attenuation and rain volume backscatter for the four DFS beams, and brightness temperature at the top of the atmosphere for all the dual polarized AMSR channels.

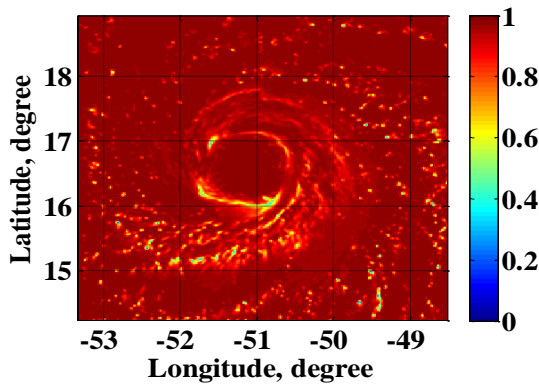
Figure 3.6 shows WRF simulation output of surface wind speeds (0-50 m/s) in panel-a, rain rates (0-80 mm/hr) in panel-b, C- and Ku-band atmospheric attenuation (0-1, power ratio) in panel-c and -e respectively, and C- and Ku-band RVBS (0-0.15 power ratio) in panel-d and -f respectively, for Hurricane Isabel in September 2003.



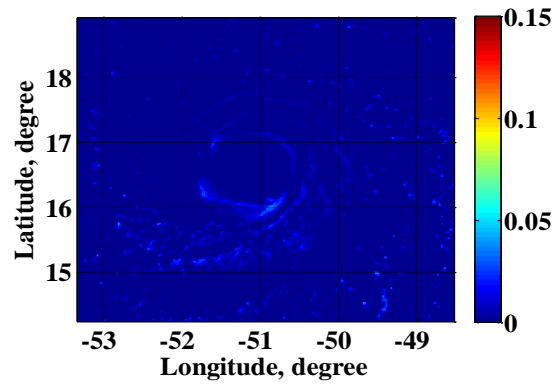
(a)



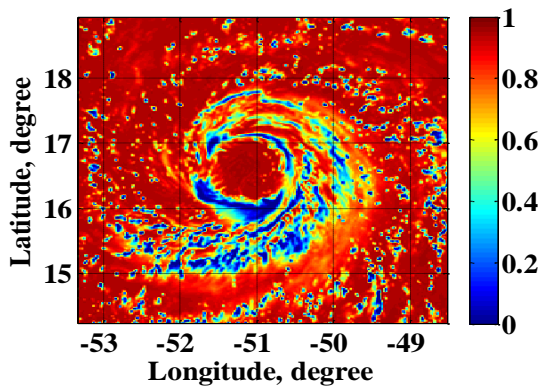
(b)



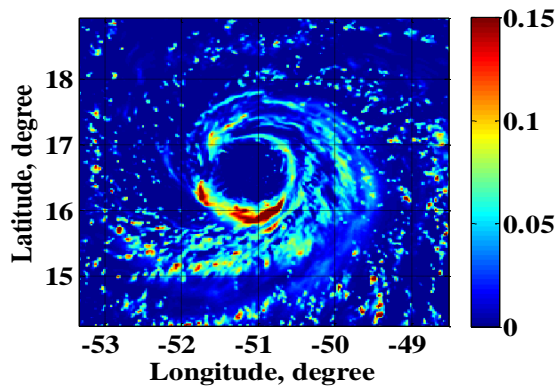
(c)



(d)



(e)



(f)

Figure 3.6 WRF simulation of Hurricane Isabel in September 2003 showing (a) wind speed, (b) rain rate, (c) C-band attenuation, (d) C-band RVBS, (e) ku-band attenuation, and (f) Ku-band RVBS.

3.3 Realistic Measurements Simulation

For the conceptual DFS/AMSR sensor payload proposed for the future GCOM-W2 mission, a major emphasis for improved OVW measurements is associated with extreme wind events (tropical and extra-tropical cyclones). This is the area that current satellite scatterometer systems consistently underestimate the peak wind speed of these storms in the presence of strong precipitation.

To meet our objectives, realistic active and passive observations of hurricanes are required to develop a robust OVW retrieval algorithm. Since the DFS and AMSR combination have not flown, there are no real observations available; thus, simulated simultaneous active/passive remote sensor measurements and associated WRF nature runs were used to train the empirical OVW algorithm over a wide range of possible geophysical parameters. Afterwards, the efficacy of the OVW retrieval processes were assessed using an independent set of simulated observations and nature runs surface truth.

This simulation process is described below. We started with the instruments viewing geometry simulation to generate measurements locations on the Earth's surface, and then we used the output of the geometry module to simulate realistic active and passive measurements as will be shown in the following subsections.

3.3.1 Viewing Geometry Simulation

A conical scanning microwave remote sensor orbit simulator was developed to simulate DFS and AMSR viewing geometry including the antenna instantaneous field of view (IFOV) on the Earth's surface as a function of azimuth look directions for the multiple sensor beams. For the DFS, the simulated IFOVs were further subdivided into range bins or "slices" with a width of 2 km each to emulate the planned pulse compression range gate processing to improve the sensor spatial resolution. The location (latitude/longitude) of slice centroid was stored for subsequent simulation processing.

Figure 3.7 illustrates the output of the DFS orbit simulator for the Ku-band outer beam. Panel-a shows a single antenna IFOV divided into range bins, and panel-b shows the resulting DFS IFOV surface sampling of the rotating antenna on a longitude/latitude grid.

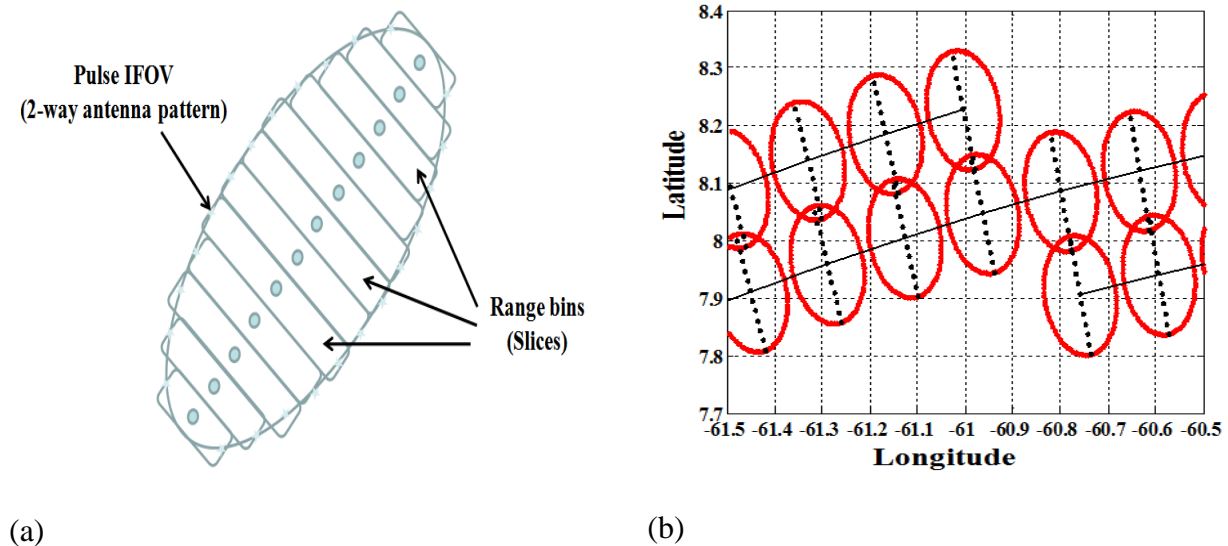


Figure 3.7 (a) a single pulse IFOV with range bins (slices) and (b) DFS IFOVs for the Ku-band outer beam showing along track and along scan overlap.

3.3.2 DFS Observations Simulation

Using the output of geometry module, high-resolution WRF fields were interpolated to the slice centroid locations. For the DFS, we mapped these interpolated WRF 10m wind vectors and relative azimuth look angles into (rain- and noise-free) C- and Ku-band surface slice σ^0 values using the IWRAP GMF model functions [7]. As described in Chapter 2, the IWRAP GMF was developed using airborne C- and Ku-band σ^0 measurements in hurricanes for wind speeds as high as 65 m/s in rain-free conditions. Hence, we have high confidence in the fidelity of the ocean surface σ^0 simulation used in this dissertation. The challenge, however, is to translate these surface σ^0 values to DFS slice σ^0 observations at the top-of-the-atmosphere (TOA).

However, due to the fact that rain bands are spatially small with a very dynamic structure, the rain contamination of σ^0 values was made on a smaller geometry scale than the slice level. Thus, IFOV slices were further subdivided into sub-slices with 2 km separation and the slice σ^0 values were linearly interpolated to the sub-slice locations before being corrupted with rain.

Subsequently, the WRF high-resolution RVBS and α fields were interpolated to the IFOV sub-slice locations, and applied to the surface sub-slice σ^0 values to produce the rain contaminated sub-slice σ^0 observations based on equation (2.9) described earlier in Chapter 2. The rain corrupted sub-slice σ^0 values were integrated over the slice IFOV modulated by the two-way antenna pattern and spatial response to generate noise-free σ^0 values at the top of the atmosphere ($\sigma^0_{TOA, noise-free}$).

Figure 3.8 (a, and b) shows the DFS antenna patterns for the C- and Ku-band beams, where color indicates antenna gain in dB. Note the differences in the C- and Ku-band antenna beam scales.

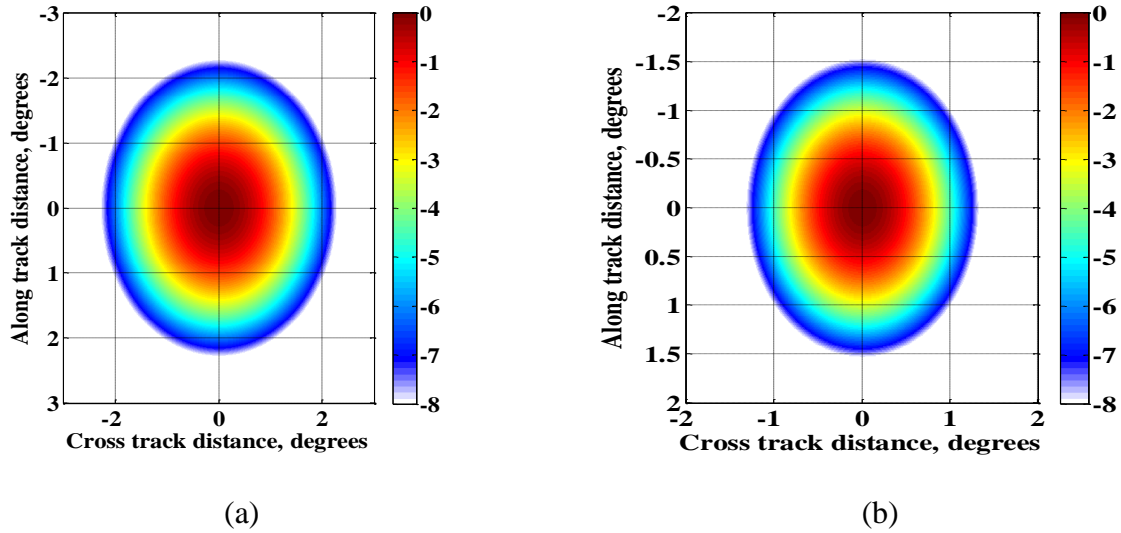


Figure 3.8 DFS antenna patterns for the (a) C- and (b) Ku-band beams.

The final step in simulating slice σ^0 observations is to add a zero-mean Gaussian noise that corresponds to the scatterometer instrument measurement. The normalized standard deviation of this noise, denoted as (k_p) , is a combination of several uncertainties due to the Rayleigh fading of the ocean echo and signal to thermal noise power ratio, which is mathematically modeled as follows [44]:

$$K_p = \sigma^0 \sqrt{\frac{1}{N} \left(1 + \frac{2}{SNR} + \frac{1}{SNR^2} \right)} \quad (3.1)$$

where N is the number of independent range bins averaged prior to down-linking, and SNR is the signal to noise ratio of the slice σ^0 measurements. In this equation, low wind speed performance is limited by the SNR while high wind speed performance is limited by N . Figure 3.9 shows the calculated k_p for various values of H-pol Ku-band σ^0 shown in dB scale.

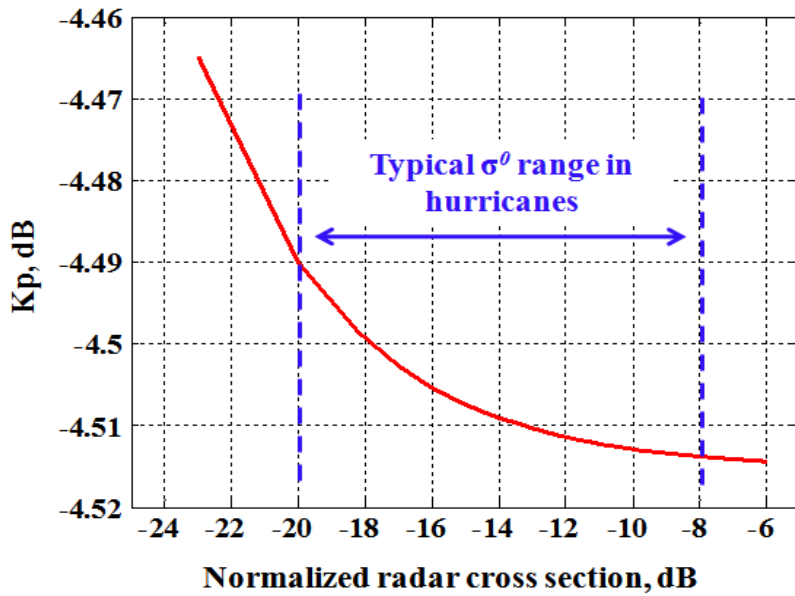


Figure 3.9 The calculated k_p values for various values of H-pol Ku-band σ^0 in dB scale.

Afterwards, K_p is used to generate zero-mean Gaussian noise to perturb the top of the atmosphere σ^0 ($\sigma_{TOA, noisy}^0$) as shown in (3.2) to represent the conventional scatterometer measurements, where " μ " is a unit normal Gaussian random number generator.

$$\sigma_{TOA, noisy}^0 = (1 + K_p) \times \mu \times \sigma_{TOA, noise-free}^0 \quad (3.2)$$

The values of $\sigma_{TOA, noisy}^0$ represent the DFS simulated measurements that will be used later in the algorithm development. Figure 3.10 summarizes the active measurements simulation steps in a top-level block diagram.

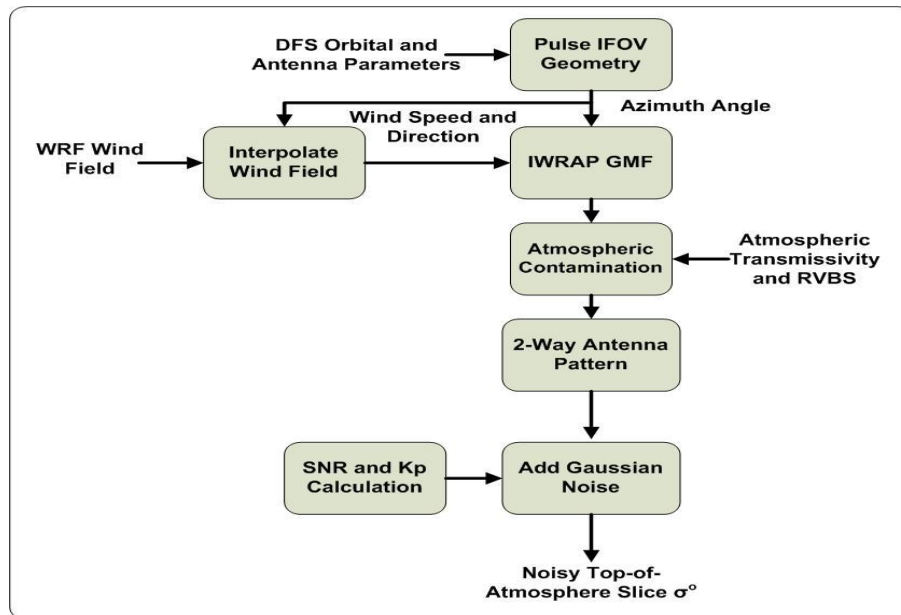


Figure 3.10 DFS σ^0 simulation top-level block diagram.

3.3.3 AMSR Brightness Temperatures Simulation

High resolution (1.3 km) H- and V-pol Tb's were simulated by the Jet Propulsion Laboratory using the RTM described earlier (section 3.2) at AMSR frequencies and incidence angle. These Tb fields were integrated over the corresponding antenna beam IFOVs after applying Gaussian effective antenna weighting pattern to simulate the corresponding AMSR antenna temperature observations. Figure 3.11 illustrates the process of calculating the Tb values at the center of the IFOV for AMSR channels.

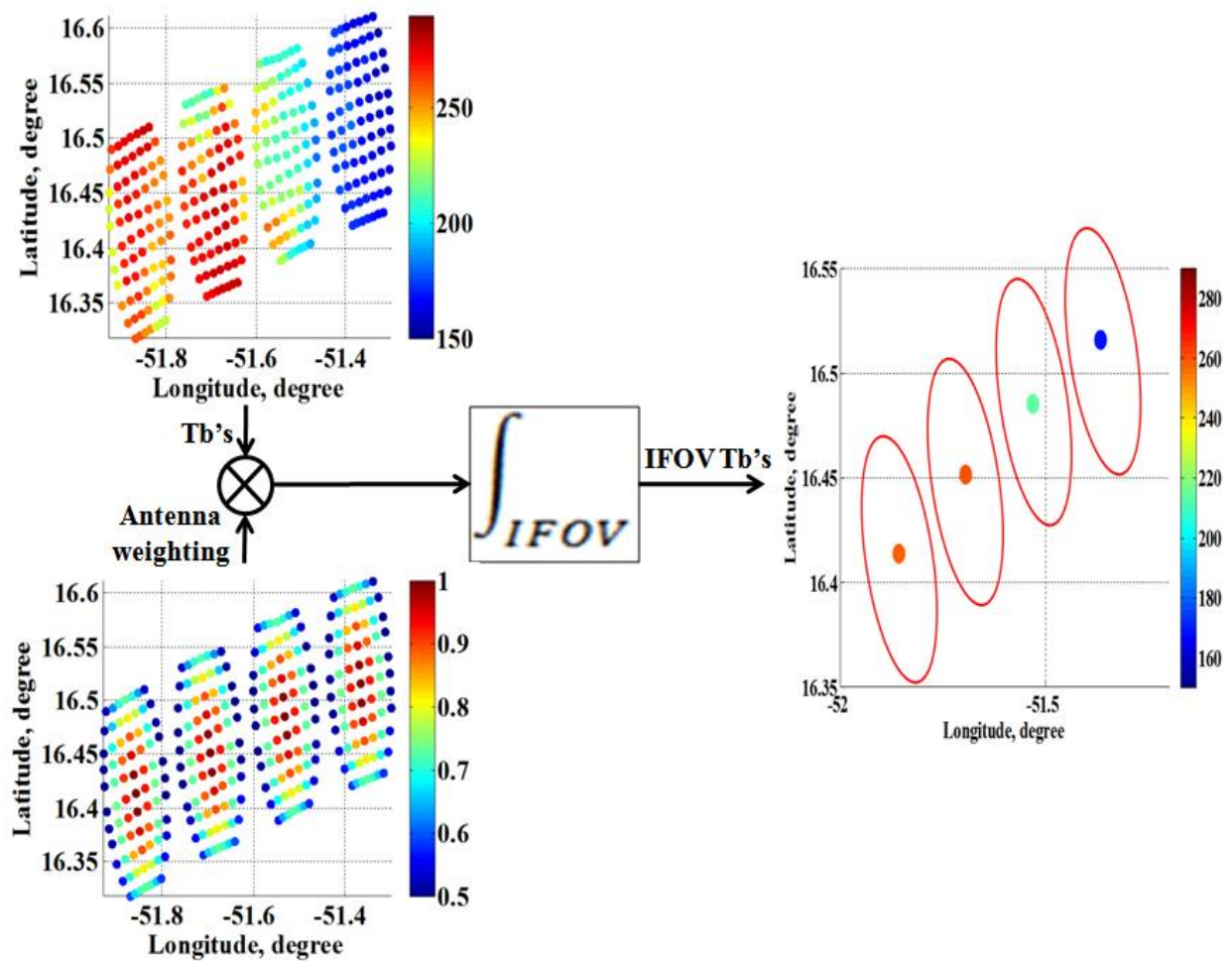


Figure 3.11 Calculating antenna brightness temperatures at the center of the IFOV for AMSR channels.

Figure 3.12 shows the H-pol Tb fields in Kelvin for the 6, 19, and 89 GHz AMSR channels on a latitude/longitude grid respectively, for hurricane Isabel in September 2003. The right side panels (a, c, and e) show the original high-resolution Tb fields, and the left side panels (b, d, and f) show the antenna weighted Tb fields. From this figure, we can observe the degradation in the resolution of the measurements for lower frequencies due to the increased antenna IFOV. The corresponding figure for the V-pol brightness temperatures is given in Appendix-C.

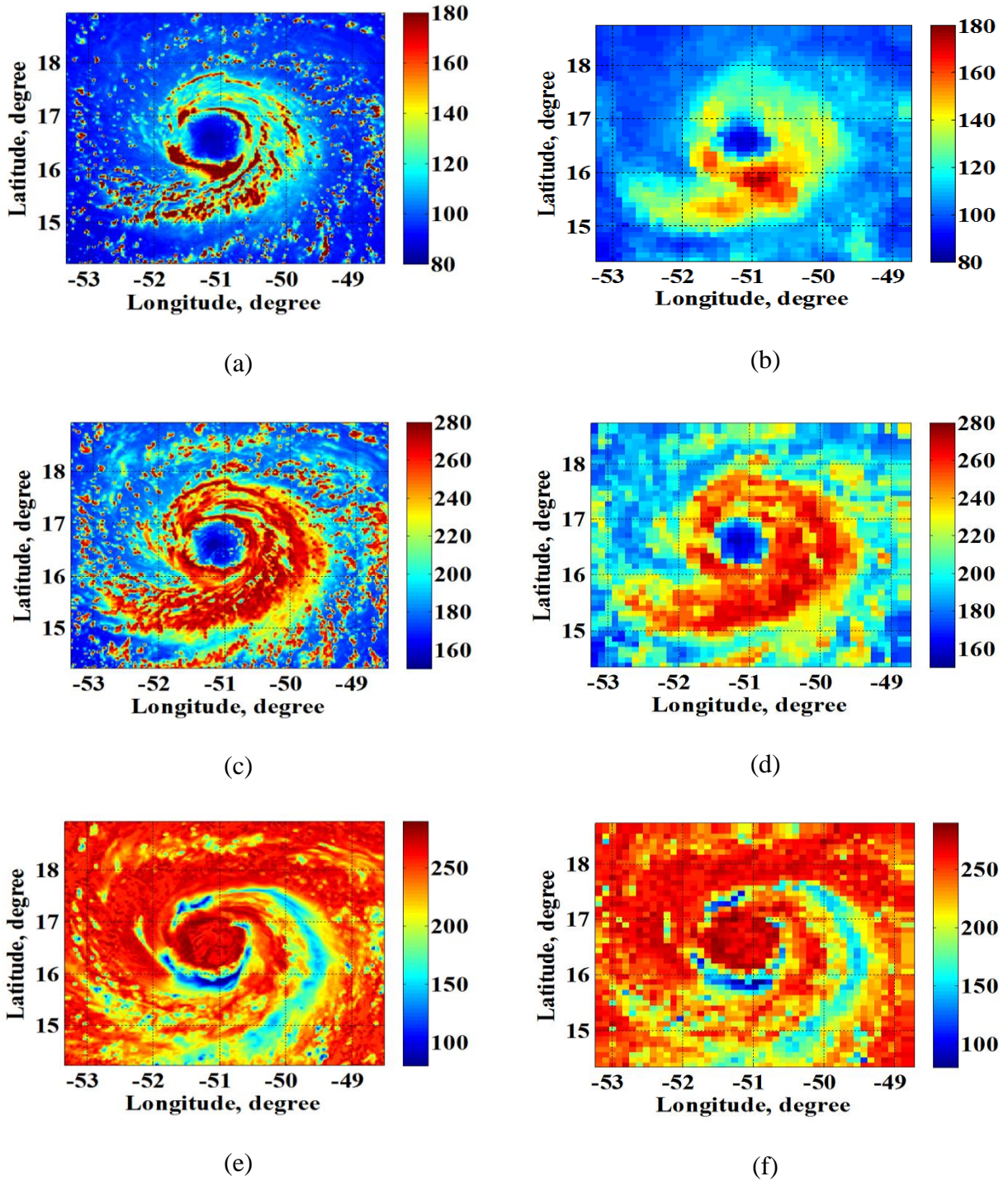


Figure 3.12 H-pol Tb fields on a latitude/longitude grid, for hurricane Isabel in September 2003. Right side panels (a, c, and e) show the original high resolution Tb fields, and the left side panels (b, d, and f) show the averaged Tb fields over the antenna pattern for 6, 19, and 89 GHz AMSR channels respectively.

3.4 Validation of Simulated Measurements

The main goal of this evaluation process is to assess the simulation capability to generate realistic slice σ^0 and Tb measurements at the top of the atmosphere using high fidelity simulated hurricane environmental parameters from WRF and theoretical EM radiative transfer models with scattering.

Under rain-free conditions, where atmosphere is slightly absorptive, the observed Tb by an ocean-viewing, space-borne, microwave radiometer can be accurately modeled using radiative transfer theory. Conversely, due to the high 3-D variability of the rainy atmosphere associated with tropical cyclones, the details of precipitation microphysical parameters (including graupel and rain drop size distribution (DSD)) are difficult to characterize [45-47]. Moreover, due to the larger hydrometeor diameters associated with tropical rain rates, it is not possible to use the simple Rayleigh approximation for absorption (rain particle size $\gg \lambda$), and the full Mie scattering theory needs to be applied.

According to this, simulated remotely sensor signatures (radar reflectivity and microwave brightness temperatures) of hurricanes are critically dependent on the DSD and microphysical assumptions. This sensitivity can negatively affect the accuracy of the simulations due to significant uncertainty in the DSD of the convective precipitating systems that dominate tropical rainfall. However, it also provides an opportunity to use comparisons between satellite scatterometer and radiometer observations in hurricanes and forward RTM simulated radiometric

signatures of precipitation to understand the sensitivity of DSD and microphysical parameter assumptions that result in most realistic simulated hurricanes.

Hence, the microphysical processes and their representation in hurricane models are of crucial importance for accurately simulating hurricane intensity and evolution. The accurate modeling of the microphysical processes becomes increasingly important when running high-resolution models that should properly reflect the convective processes in the hurricane eyewall. Several studies have addressed that in an attempt to understand how the microphysical assumptions affect the storm intensity, vertical structure, size and track.

In this dissertation, in spite of the fact that we have a limited set of rain microphysics in the available WRF nature runs, we evaluated the output of the simulation by comparing the rain signatures between the modeled and the observed data. For that purpose, we used real scenes from Hurricane Isabel in 2003 where we have real data from actual hurricane passes obtained by SeaWinds and AMSR onboard ADEOS-II. Table 3.3 renders a list of the simulated hurricane scenes and their corresponding ADEOS-II revolution number used in the validation.

Table 3.3 List of simulated hurricane scenes

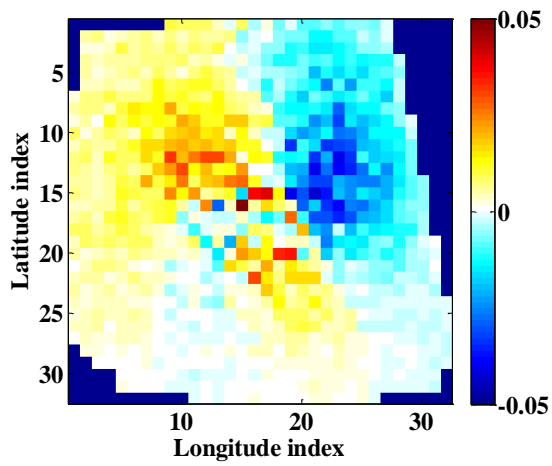
Hurricane and scene ID	Date (yyyy_mm_dd)	UTC time (hh:mm)	ADEOS-II revolution number
Isabel1	2003_09_11	01:35	3862
Isabel2	2003_09_11	14:01	3869
Isabel3	2003_09_13	02:25	3891
Isabel4	2003_09_13	14:51	3898
Isabel5	2003_09_14	02:01	3905
Isabel6	2003_09_15	03:16	3920

A stringent limitation to the evaluation process in extreme weather events is the unavailability of surface truth fields. Thus, traditional methods of validating models by direct comparisons with real *in-situ* measurements that could be paired with the satellite microwave observations will not be optimal, and significant differences are expected in the active areas of the storm, i.e. the eye wall region of the hurricane. Thus, the evaluation procedure that we have followed (to validate the representativeness of the simulated fields) was based on qualitative statistical techniques rather than quantitative pixel comparisons.

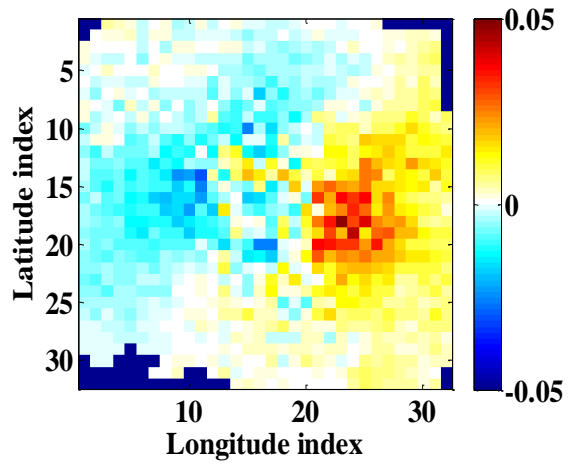
First, we compared the wind directional signature ($\Delta\sigma^0$) of the simulated σ^0 values with the corresponding signatures obtained from real measurements provided in SeaWinds L2A data products. The $\Delta\sigma^0$ is calculated by the differences between composite slice σ^0 observations from multiple azimuth looks in 25 km WVCs. Since rain effects on σ^0 measurements tend to be

isotropic, they are nearly independent of azimuth and therefore cancel when taking the difference between forward and aft looks. Thus, the dominant feature of the $\Delta\sigma^0$ obtained from multiple azimuth observations is caused by the wind direction change around the eye.

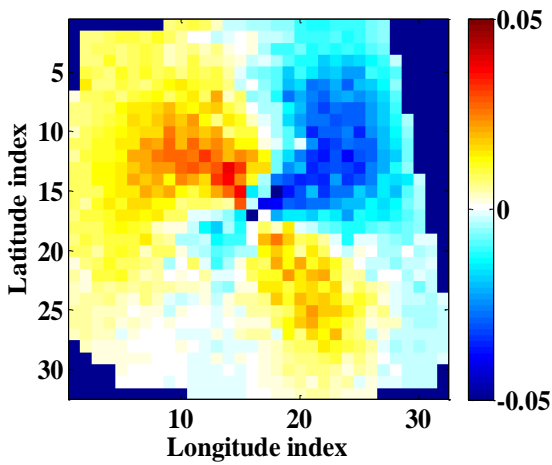
Figure 3.13 illustrates H-pol $\Delta\sigma^0$ in dB scale for two hurricane scenes (Isabel3 and Isabel4). The upper panels (a, and b) show the simulated $\Delta\sigma^0$, and the lower panels (c, and d) show the SeaWinds L2A $\Delta\sigma^0$. From this figure, we can see that the measured and modeled $\Delta\sigma^0$ for the two hurricane scenes match very well. Corresponding results for V-pol $\Delta\sigma^0$ are presented in Appendix – D.



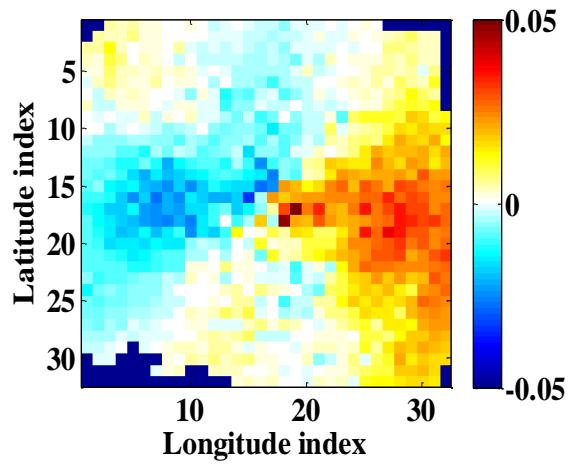
(a)



(b)



(c)



(d)

Figure 3.13 H-pol Wind directional signature for hurricane scenes Isabel3 (left panels) and Isabel4 (right panels). Upper panels [(a) and (b)] give the simulated results, and lower panels [(c) and (d)] give the SeaWinds measurements from ADEOS-II.

As will be discussed in Chapter 4, the simultaneous dual-polarized passive measurements will be used as part of the rain correction applied to the measured σ^0 at the top of the atmosphere. Thus, having the simulated active and passive measurements to be correlated, as real observations are, is very crucial to the fidelity of the OVW retrieval algorithm development. Given that, Cross-correlations between simulated active and passive measurements hurricane signatures at the top of atmosphere were compared to real ADEOS-II observations as shown in Fig. 3.14. The upper panel shows ADEOS-II real observations, while the lower panel shows the simulated data. In all the sub-figures, the x-axis is the H-pol σ^0 in dB, and the y-axis is the H-pol AMSR Tb in Kelvin for frequencies (10, 19, 37, and 89 GHz). Color indicates AMSR measured rain rate in the ADEOS-II observations plots, and WRF simulated rain rate in the simulated observations plots.

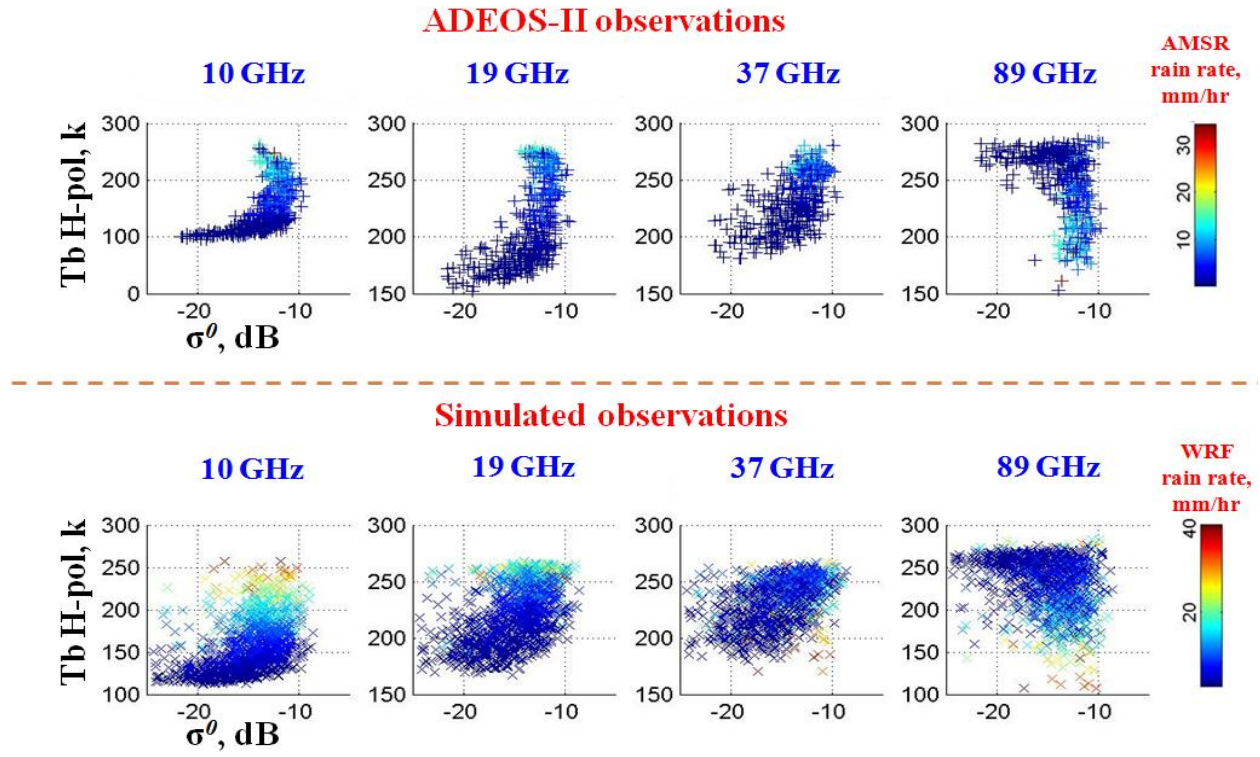


Figure 3.14 H-pol Cross-correlations between real ADEOS-II active and passive observations hurricane signatures at the top of atmosphere (upper plots) and simulated observations (lower plots).

We conclude that the real and simulated hurricane observations follow similar patterns. Note that the variations in the in the σ^0 and Tb are both driven by the dynamic range of wind speed and rain rates within the hurricane. For instance, in the 10 GHz case, high rain rates increase the Tb values while their attenuation effect decreases the σ^0 values. At the other extreme, in the 89 GHz case, Tb's will be depressed with high rain rates as the σ^0 increase with wind speed (and RVBS).

For quantitative evaluation, we used the Pearson product-moment correlation coefficient (r). In general, r is a measure of correlation that is used to identify the strength of the relationship between two random variables, and can be calculated as shown below:

$$r = \frac{\sum_{i=1}^n (x_i - \bar{x})(y_i - \bar{y})}{\sqrt{\sum_{i=1}^n (x_i - \bar{x})^2} \sqrt{\sum_{i=1}^n (y_i - \bar{y})^2}} \quad (3.3)$$

where n is the sample size, x_i and y_i are the two quantities that we need to find the correlation coefficient between them, and \bar{x}, \bar{y} are their averages.

Using this procedure, the calculated correlation coefficients between H-pol σ^0 values at the top of the atmosphere and AMSR antenna brightness temperatures H-pol channels (6, 10, 19, 24, 37, 89 GHz) for four hurricane scenes is given in Fig. 3.15. Red stars indicates the value of the correlation coefficient calculated from real SeaWinds and AMSR observations, and blue diamonds indicates the corresponding value calculated using the simulated data. We believe that the strong similarity between the different AMSR channels is a good indicator in the ability of the simulation to capture realistic active and passive microwave signatures.

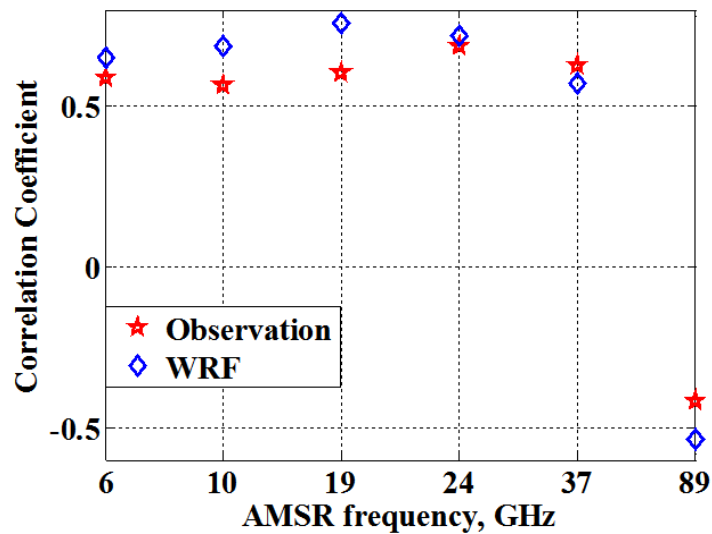


Figure 3.15 Calculated correlation coefficients from the measured parameters (red stars) and the simulated parameters (blue diamonds) for H-pol AMSR channels.

The final step in the evaluation process was to compare the simulated σ^0 values at the top of the atmosphere with wind speeds. According to the GMF, under rain-free conditions, σ^0 values will monotonically increase with wind speed. However, in hurricane environments, where high wind speeds are usually associated with high rain rates in the eyewall region, attenuation due to rain will dominate in these regions thereby causing the scatterometer measured σ^0 values to be lower than the surface values.

Figure 3.16 shows σ^0 values at the top of the atmosphere comparison with surface wind speeds for four Hurricane Isabel cases. The color scale for symbols indicate rain rate in mm/hr (warmer colors indicates higher rain rates), and panel-a shows simulated observations, and panel-b shows corresponding SeaWinds observations. The red line represents the mean of σ^0 values at the top of the atmosphere for different wind speeds. From this figure, we see that σ^0 values at the top of the

atmosphere interacts with wind speeds and rain rates in a similar fashion for both simulated and real data, especially at very high wind speeds (> 25 m/s) and high rain rates where attenuation due to rain dominates.

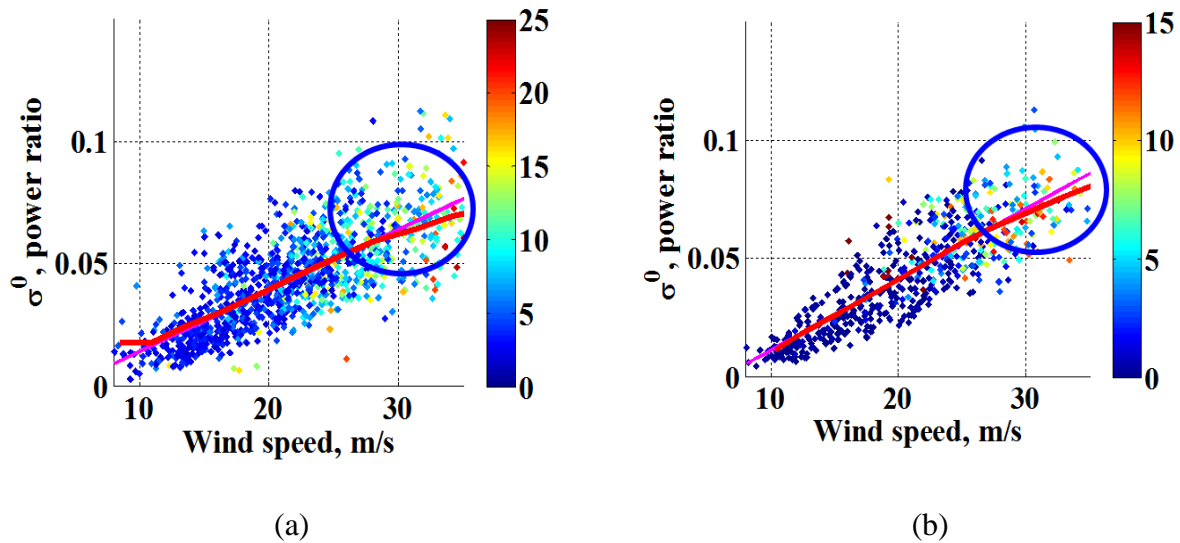


Figure 3.16 Hurricane Isabel σ^0 values at the top of the atmosphere compared with surface wind speeds for panel-(a) simulated observations, and panel-(b) SeaWinds on ADEOS-II observations.

In summary, these various statistical and qualitative evaluation results were encouraging and gave us confidence that the simulated active and passive observations in hurricanes are representative of actual observations that should be observed in real tropical cyclones. Of course, the final evidence will be when actual satellite DFS and AMSR observations are available.

As a result, the WRF nature runs (hurricane environment parameters) and simulated AMSR and DFS microwave observations were used to derive an empirical parametric relationship that

integrates the effects of wind and rain on radar backscatter from the ocean surface as will be shown in Chapter IV.

CHAPTER 4 : WIND RETRIEVAL ALGORITHM

Over the three decades of satellite scatterometer observations (1978 - present), several algorithms have been developed that are capable of retrieving accurate ocean surface wind vectors provided that the scenes under observation are rain-free [10, 24, 48-50]. Unfortunately, the performance of these algorithms usually degrades significantly in the presence of precipitation because they do not account for rain effects on the measured signal.

Moreover, for most applications, it is highly desirable to have accurate wind vector retrievals under all weather conditions. With this as a goal, this chapter describes the development of a new active/passive OVW retrieval technique that infers accurate wind vectors in extreme weather conditions, including very high winds (30–60 m/s) and intense rain. Being based on the conceptual design of the future GCOM-W2, this technique has the potential to enhance the usefulness of scatterometer winds in hurricanes for future NASA/NOAA scatterometer missions [51].

The main aspect of this new technique is the ability to correct Ku-band DFS measurements for rain effects before being inputted to the OVW retrieval process. The rain correction procedure utilizes the independent information provided by the simultaneous C-band scatterometer and dual polarized multi-frequency radiometer measurements from DFS and AMSR. The following sections describe the development of the rain correction and OVW retrieval procedures.

4.1 Rain Contamination Correction

The conventional way of obtaining corrected Ku-band radar backscatter ($\sigma_{Ku, Corrected}^0$) can be achieved by inverting equation (2.9), where superscript “^” denotes an estimated parameter as shown below:

$$\sigma_{ku, Corrected}^0 = \frac{(\sigma_{TOA}^0 - \hat{\sigma}_{Rain}^0)}{\hat{\tau}_{atmos.}} \quad (4.1)$$

Because it is difficult to distinguish the contribution from τ and σ_{rain}^0 individually, we modeled these two terms as a lumped integrated transmissivity, hereafter known as the T-factor, where T-factor > 1 corrects for rain attenuation effect and T-factor < 1 corrects for RVBS effects on Ku-band σ^0 . Accordingly (4.1) simplifies to:

$$\sigma_{Ku, Corrected}^0 = \sigma_{TOA}^0 \times \hat{T} \quad (4.2)$$

To estimate the T-factor, several approaches can be used including the use of a sophisticated RTM. However, for the RTM approach, the need of *a priori* environmental parameters inputs, the complexity, and the long computation time all put a limitation on the feasibility of these methods. An alternate approach would be to construct an empirical relationship between the available observations (C-band σ^0 and multi-frequency dual-polarized AMSR Tb's) and the T-factor.

The empirical approach was chosen for the rain correction method developed in this dissertation, and this was based upon a statistical multilinear regression procedure, as depicted in Fig. 4.1.

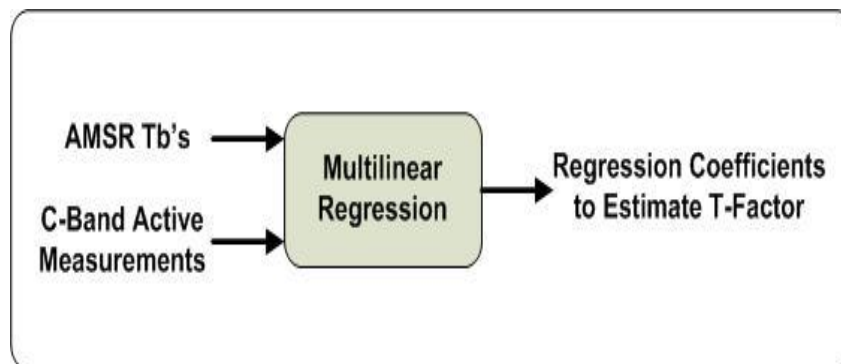


Figure 4.1 Multilinear regression procedure implemented in the rain correction.

Trade studies of AMSR and C-band DFS measurements were conducted and evaluated to choose the best combination of available parameters to estimate the T-factor. Tables 4.1 and 4.2 summarize the combinations that were studied to estimate the H- and V-pol T-factor respectively.

Table 4.1 H-pol T-factor Combinations

Combinations	Parameter		
	H-pol AMSR Tb's	V-pol AMSR Tb's	Inner beam C-band σ^0
Case 1	✓	✗	✗
Case 2	✗	✗	✓
Case 3	✓	✗	✓
Case 4	✓	✓	✗
Case 5	✓	✓	✓

Table 4.2 V-pol T-factor Combinations

Combinations	Parameter		
	H-pol AMSR Tb's	V-pol AMSR Tb's	Outer beam C-band σ^0
Case 1	✗	✓	✗
Case 2	✗	✗	✓
Case 3	✗	✓	✓
Case 4	✓	✓	✗
Case 5	✓	✓	✓

After identifying all the possible combinations that could be used to model the T-factor, a stepwise regression was employed to determine the statistical significance of the independent variables that were included in the multilinear regression for each combination. Stepwise regression is a systematic method for adding or removing terms from a multilinear model based

on their statistical significance in a regression analysis. The method begins with an initial model and then compares the explanatory power of incrementally larger and smaller models. At each step, the p value of an F -statistic is computed to test models with and without a potential term.

Figure 4.2 illustrates the stepwise regression process in general.

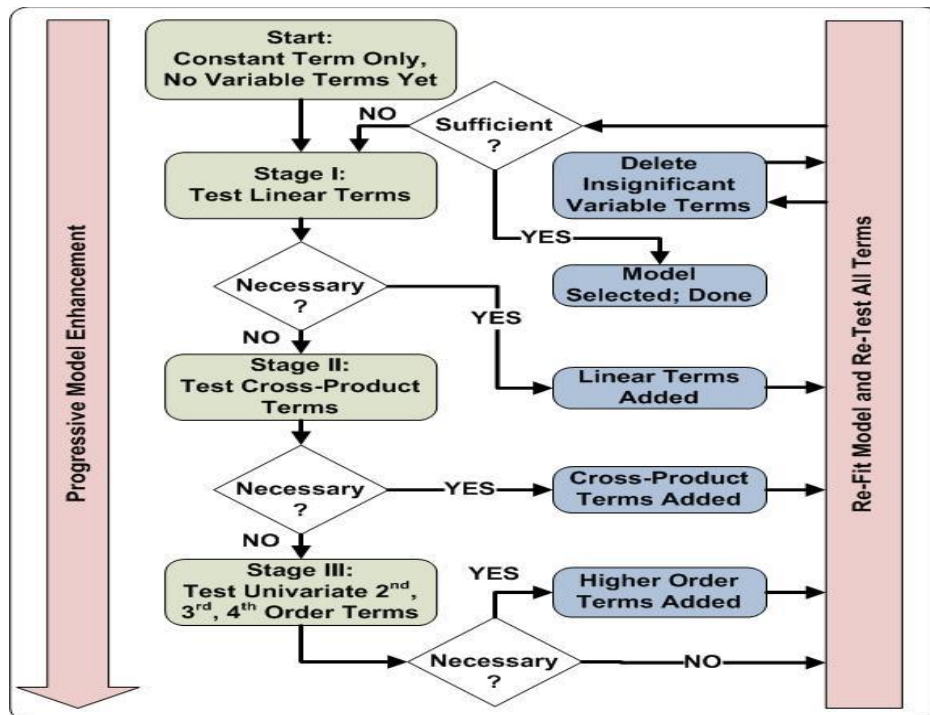


Figure 4.2 Stepwise regression procedure [from Wikipedia: <http://en.wikipedia.org/wiki/File:Stepwise.jpg>].

After applying the stepwise regression analysis on all the possible combinations, the results indicated that not all parameters are statistically significant to the regression, and hence could be eliminated. The resulting regression model was simpler and computationally faster. Table 4.3 lists the eliminated parameters from the regression before estimating the H- and V-pol T-factor based on the stepwise regression analysis.

Table 4.3 Stepwise Regression Analysis Output

Case number	Parameters to be eliminated (H-pol)	Parameters to be eliminated (V-pol)
Case 1	37 GHz H-pol Tb	24 GHz V-pol Tb
Case 2	--	--
Case 3	--	6 GHz V-pol Tb
Case 4	24 GHz H- and V-pol Tb, 37 GHz V-pol Tb	10 GHz V-pol Tb, 24 GHz H- and V-pol Tb, 37 GHz V-pol Tb, 89 GHz H-pol Tb
Case 5	37 GHz V-pol Tb	10 GHz H-pol Tb, 24 GHz H- pol Tb

To statistically analyze the utility of the regressed model for each of the tested cases, the coefficient of determination (R^2) was calculated. It is defined as the proportion of variability in a data set that is accounted for by the statistical model. In other words, R^2 provides a measure of the model adequacy (a ratio that ranges from 0 to 1 with 1 indicating perfect modeling) and can be calculated as shown below:

$$R^2 = \frac{SS_{reg}}{SS_{tot}} \quad (4.3)$$

$$SS_{tot} = \sum_{i=1}^n (y_i - \bar{y})^2 \quad (4.4)$$

$$SS_{reg} = \sum_{i=1}^n (\hat{y}_i - \bar{y})^2 \quad (4.5)$$

where SS_{tot} is the total variability, and SS_{reg} is the explained variability by the regression. Table 4.3 shows a comparison for the R^2 calculated values for all the cases used to model the T-factor for both H- and V-pol.

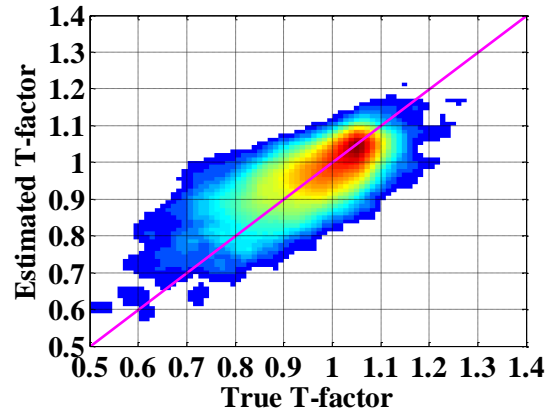
Table 4.4 R2 comparison of T-factor model

Case number	H-pol model adequacy	V-pol model adequacy
Case 1	36 %	39 %
Case 2	10 %	6 %
Case 3	61 %	65 %
Case 4	58 %	61 %
Case 5	70 %	71 %

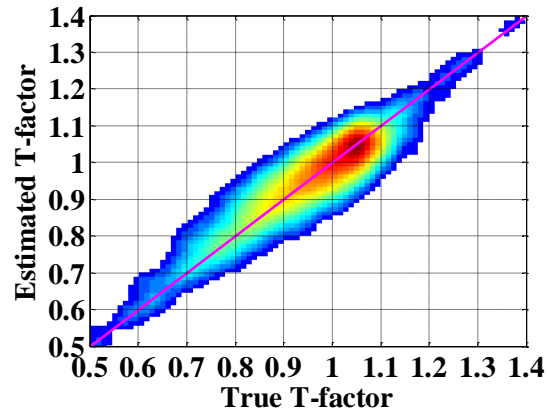
From table 4.4, we see that the best results in modeling the T-factor are achieved when AMSR H- and V-pol Tb's along with the C-band σ^0 measurements are included in the multilinear regression procedure. These substantial improvements in estimating the T-factor will significantly improve the rain correction process and thereby will improve OVW retrievals.

Because of the simulation, we know the true value of the T-factor for each pixel. Thus, we present selected scatter plots of estimated versus true T-factors for three cases in Fig. 4.3. Panel-

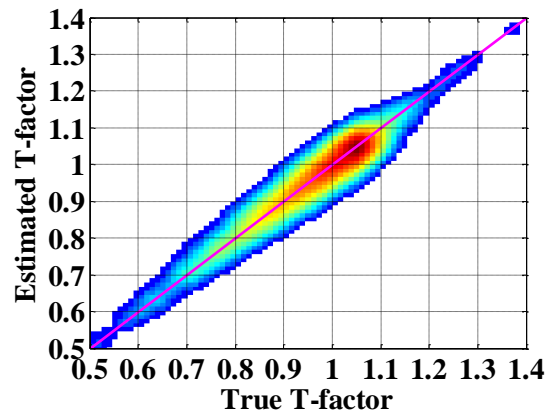
a shows the results when only the H-pol Tb's were used to estimate the T-factor. Next, panel-b shows the results when H- and V-pol Tb's were used to estimate the T-factor. Finally, panel-c shows results when C-band σ^0 measurements and H- and V-pol Tb's were used to estimate the T-factor. It is apparent that panel-c provides the best approach, which was used for the results presented in Chapter 5. The corresponding figure for the estimated V-pol T-factor is shown in Appendix - E.



(a)



(b)



(c)

Figure 4.3 H-pol T-factor comparison using (a) AMSR H-pol Tb's only, (b) AMSR H- and V-pol Tb's, and (c) AMSR H- and V-pol Tb's with C-band σ^0 measurements.

From a spatial scale perspective, the T-factor was developed at the scatterometer Ku-band IFOV level. The brightness temperatures and the C-band σ^0 measurements were spatially interpolated to the Ku-band IFOV boresight locations before being used in the multilinear regression procedure described above.

However, for the OVW retrieval algorithm, the estimated T-factor values are interpolated to the Ku-band IFOV slice locations to provide the appropriate correction for each Ku-band slice σ^0 measurement. The spatial interpolation method implemented is based on the “natural-neighbor” criterion [52], which has the advantage of providing a smoother approximation to the underlying data especially that we are dealing with hurricanes, where the geophysical fields do not vary smoothly, and some abrupt changes from point to point may occur.

Finally, after estimating the T-factor, the correction is implemented as shown in equation (4.2), and the corrected Ku-band DFS measurements are inputted to the OVW retrieval process as will be described in the following section.

4.2 Wind Vector Retrieval Algorithm

In the OVW retrieval part of the algorithm, only the Ku-band DFS measurements were used after being corrected for rain effects using the C-band DFS measurements and AMSR Tb's. The algorithm will take advantage of the rain corrected Ku-band high-resolution measurements to

retrieve hurricane force winds. Figure 4.4 shows a top level block diagram for the OVW retrieval process.

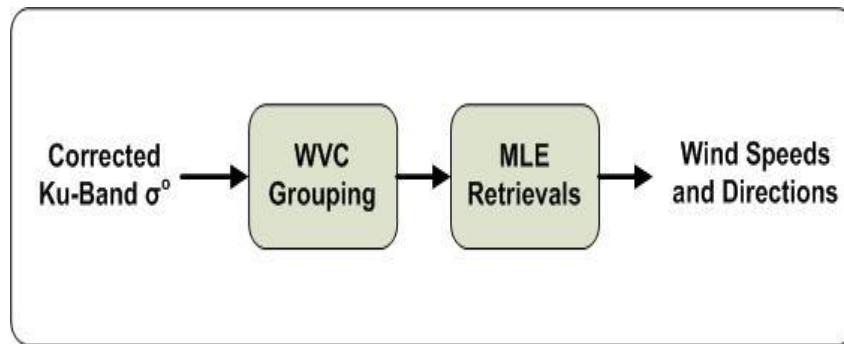


Figure 4.4 OVW retrieval process block diagram.

The conventional MLE method described earlier was used in the retrievals. The size of each WVC is defined as a $10 \text{ km} \times 10 \text{ km}$ box. The grouping procedure combines all σ^0 slices that fall within the WVC boundaries in a weighted sense. Each slice is multiplied by a Gaussian weighting (w_j) according to the inverse distance from slice center to WVC center as illustrated in Fig. 4.5. The green colored slices represent IFOV range bins that were grouped and included in the MLE after applying the Gaussian weighting scheme.

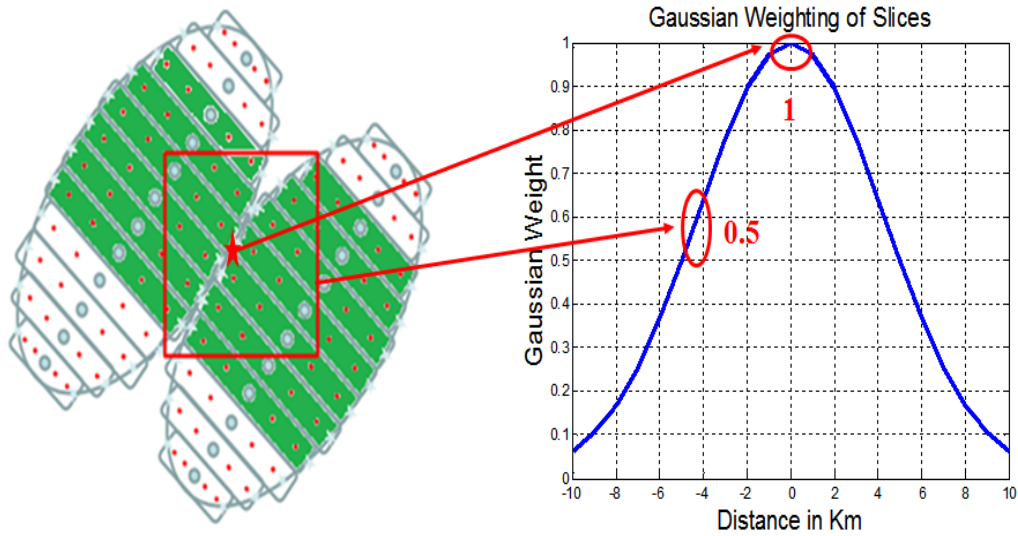


Figure 4.5 Grouped IFOV slices (filled with green color) with portions falling within the WVC boundaries (red box) showing the Gaussian weighting scheme applied.

Afterwards, the grouped measurements are inputted to the MLE objective function (ζ) as expressed in (4.6):

$$\zeta = \sum_{pol=V,H}^n \frac{w_j * \left(\sigma_{ku, Corrected}^0 - \sigma_{GMF}^0(wS, \chi) \right)_{pol}^2}{(Kp^2)} \quad (4.6)$$

The retrieved OVW is based upon the best case (closest wind direction alias to WRF wind direction) of the highest four-ranked wind vector aliases that were kept. An example on the DFS OVW retrieval for one WVC is shown in Fig. 4.6. Panel-a shows 3-dimensional (3-D) MLE residue surface (in dB) with respect to wind direction and wind speed. The wind vector solutions are the local minima of the MLE surface, and the corresponding 2-dimensional (2-D) projections

of these minima are shown as contour plots in panel-b. For this case, four different aliases were retrieved with the deepest null in panel-a indicated as the highest rank alias defined by the dark blue contour in panel-b.

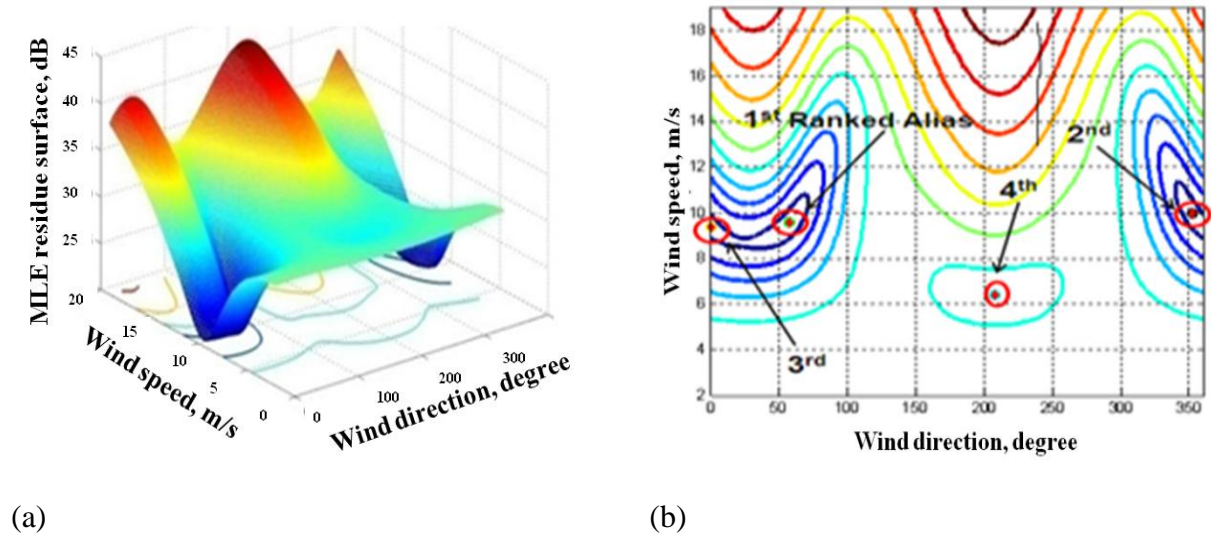


Figure 4.6 MLE objective function. a) 3-D active/passive (RadScat) MLE residue surface in dB, b) 2-D residue contours with ranked wind vector aliases.

A summary block diagram for the end-to-end simulation performed for the GCOM-W2 mission is provided in Fig. 4.7.

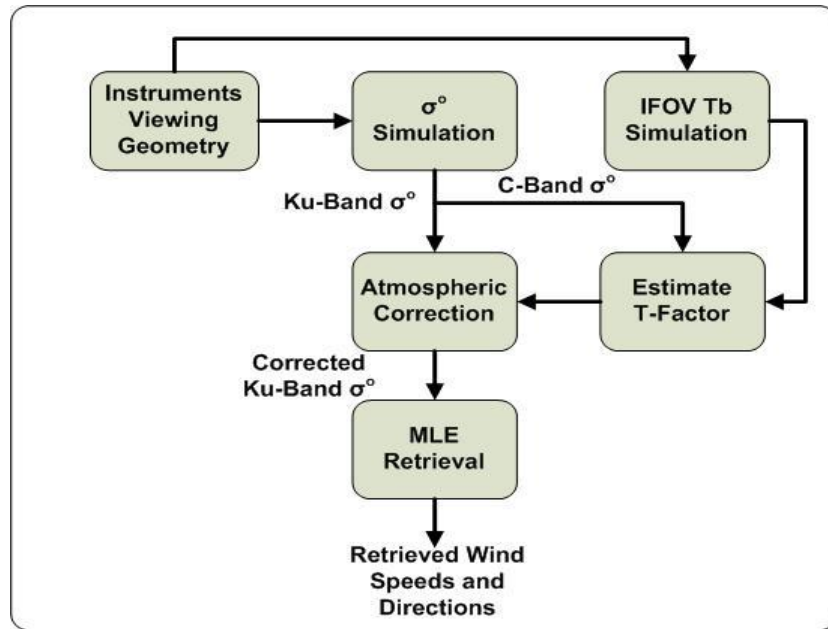


Figure 4.7 GCOM-W2 end-to-end simulation block diagram.

In the next chapter, we will evaluate the effectiveness of the rain correction procedure we developed, and we will test the performance of the OVW retrieval algorithm by comparing the retrieved wind vectors with the WRF surface truth.

CHAPTER 5 : ALGORITHM PERFORMANCE EVALUATION & RESULTS

In this chapter, the performance of the new Ku-band OVW retrieval algorithm, developed under this dissertation, will be assessed from several aspects. First the effectiveness of the Ku-band rain correction procedure will be examined. Next, wind speed and wind direction retrievals will be compared with WRF nature run of Hurricane Isabel as the assumed surface truth. A three-way comparison will be performed between: conventional Ku-band OVW MLE retrievals, conventional C-band OVW MLE retrievals, and the new rain corrected Ku-band OVW retrievals (i.e. with the T-factor applied to the σ^0 observations to correct for rain effects).

Further, statistical performance metrics are assessed and summarized; and hurricane OVW image comparisons are also presented. The overall OVW retrieval statistics presented in this chapter are based on four simulated hurricane Isabel scenes, which are independent of those used in training the regression model for rain correction.

5.1 Rain Correction Effectiveness

In order to assess the effectiveness of the rain correction procedure, Ku-band surface rain-free and noise-free simulated ocean surface σ^0 fields were compared with the corrected Ku-band σ^0 simulated top of the atmosphere observations. Figures 5.1 up to 5.3 demonstrate the comparisons made for H-pol Ku-band fields (5° by 5° latitude/longitude box) from hurricane scenes Isabel2,

Isabel5, and Isabel6. In all figures, panel-a shows the ocean surface σ^0 truth field, panel-b shows the observed σ^0 field at the top of the atmosphere (no correction applied), panel-c shows the estimated rain correction T-factor, and panel-d shows the rain corrected σ^0 surface field that was calculated using the estimated T-factor. In these figures, for illustration purposes, we limited the range of the T-factor for values > 1 to emphasize the rain correction effect on the high wind speed regions, where the rain attenuation dominates.

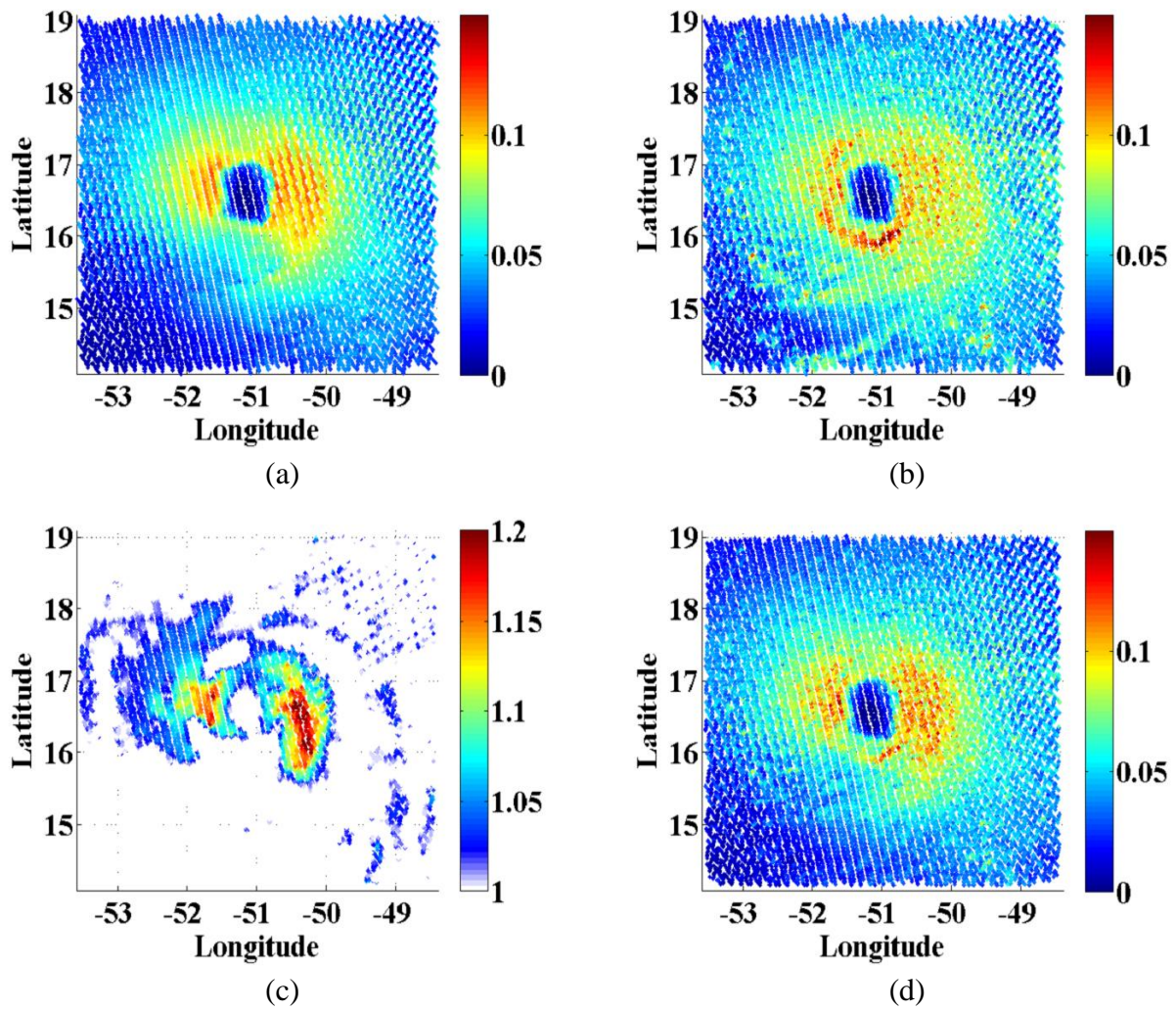


Figure 5.1 Isabel2 hurricane case for H-pol ku-band (a) surface σ^0 truth field, (b) σ^0 field at the top of the atmosphere (no correction applied), (c) estimated T-factor, and (d) the corrected σ^0 surface field using the estimated T-factor.

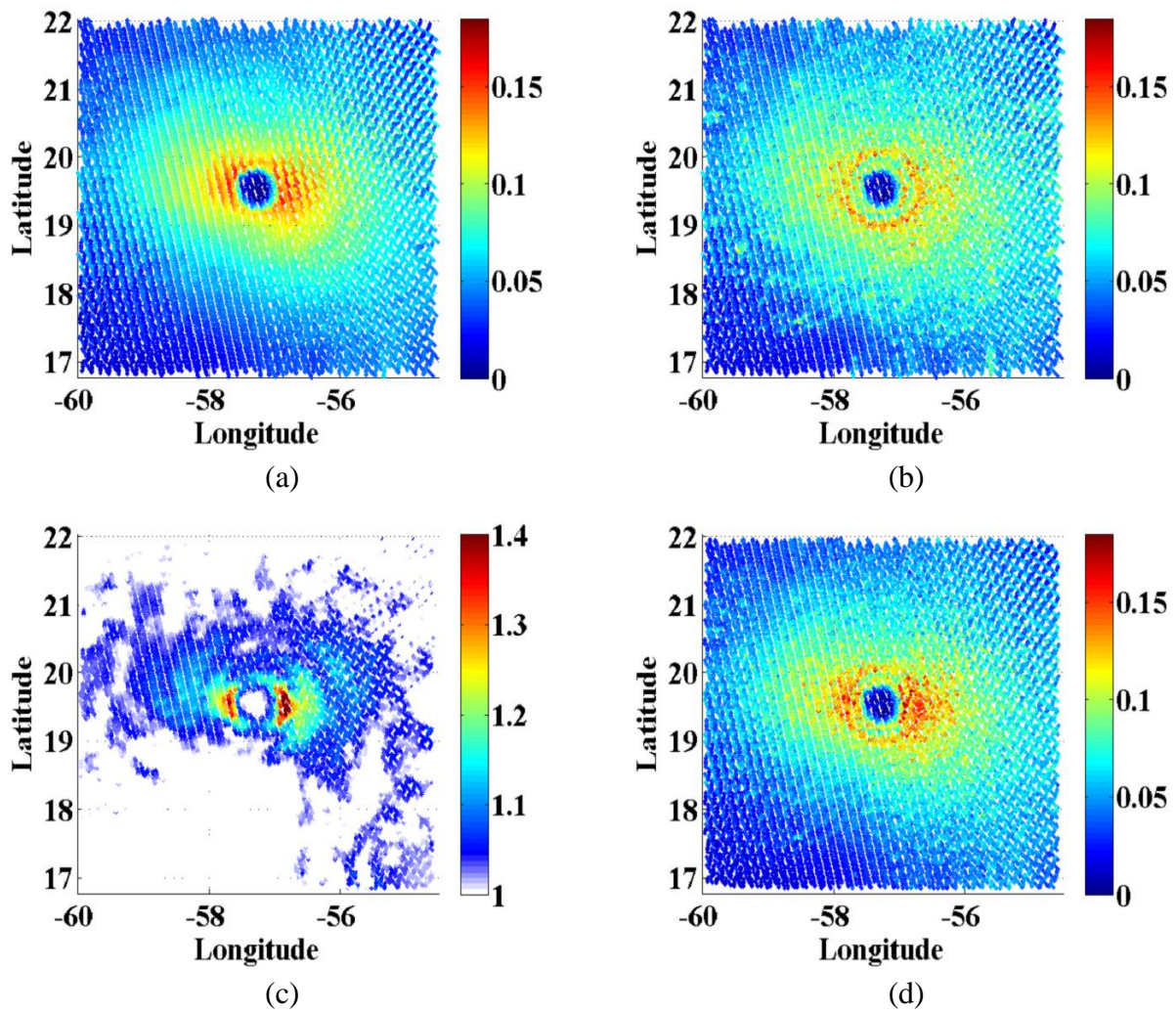


Figure 5.2 Isabel5 hurricane case for H-pol ku-band (a) surface σ^0 truth field, (b) σ^0 field at the top of the atmosphere (no correction applied), (c) estimated T-factor, and (d) the corrected σ^0 surface field using the estimated T-factor.

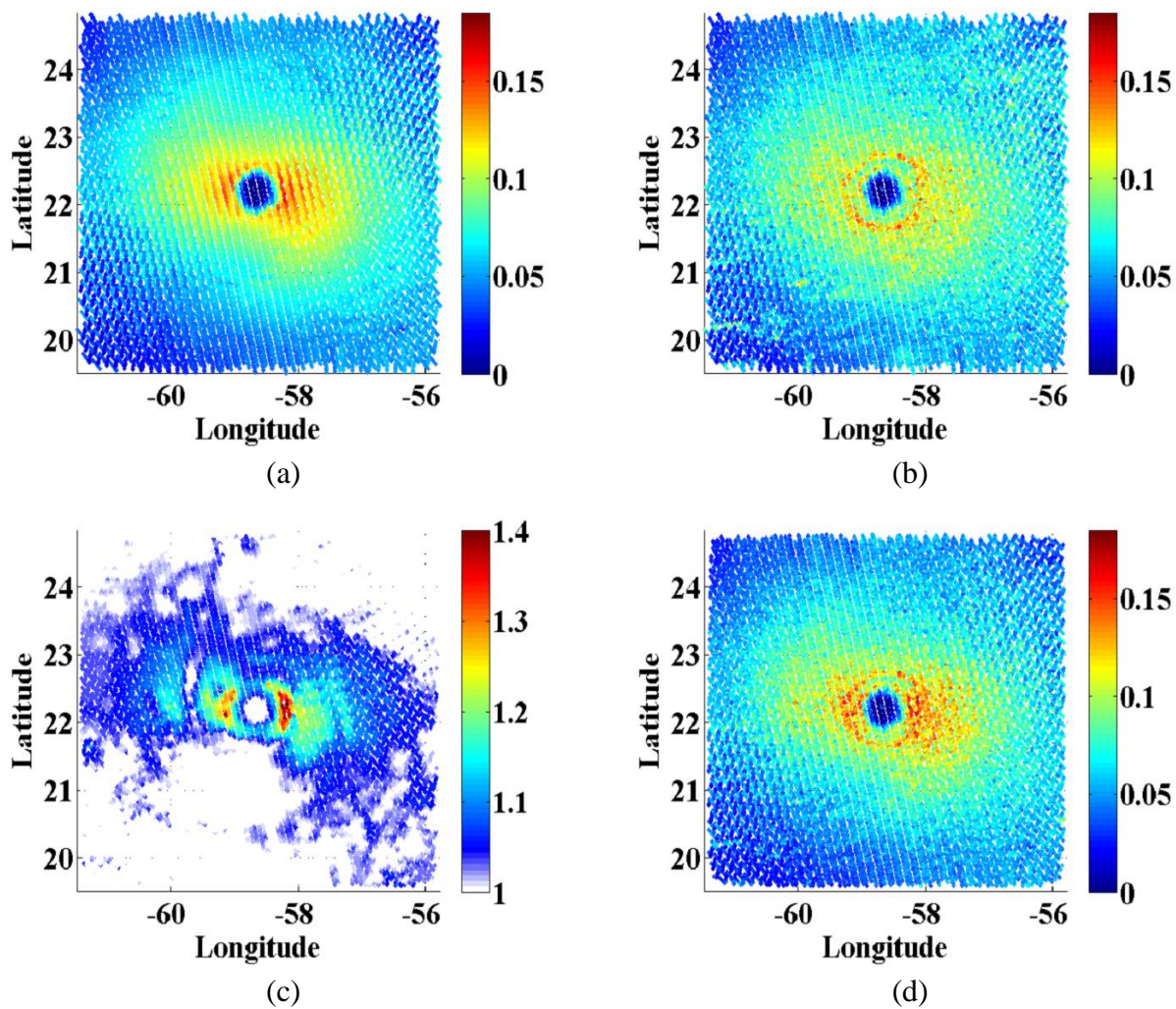


Figure 5.3 Isabel6 hurricane case for H-pol ku-band (a) surface σ^0 truth field, (b) σ^0 field at the top of the atmosphere (no correction applied), (c) estimated T-factor, and (d) the corrected σ^0 surface field using the estimated T-factor.

By subjective inspection, we can see that the applied T-factor correction compensates for the rain attenuation effect in the eye wall region of the storm where the peak winds exists; thus, using the corrected Ku-band σ^0 significantly improves the OVW retrievals as will be shown in the next section.

Another way to evaluate the effectiveness of the T-factor correction, on the measured Ku-band σ^0 values, was to examine the differences between the surface rain-free σ^0 and both σ^0_{TOA} and corrected σ^0 values. Figure 5.4 shows the comparison for H-pol Ku-band σ^0 fields (5° by 5° latitude/longitude box) from hurricane scene Isabel15. Panels-a and -b show the difference in dB (ratio in linear power) between surface σ^0 truth field, and the corresponding σ^0_{TOA} and the corrected σ^0 respectively. Color indicates the dB difference between the compared values; where blue (red) color indicates σ^0 value lower (higher) than the surface. From this figure, we see that blue color in panel-a dominates the eye wall region of the storm due to the high rain attenuation, while in panel-b the T-factor mitigated this effect, hence there is much less dark blue color in that region.

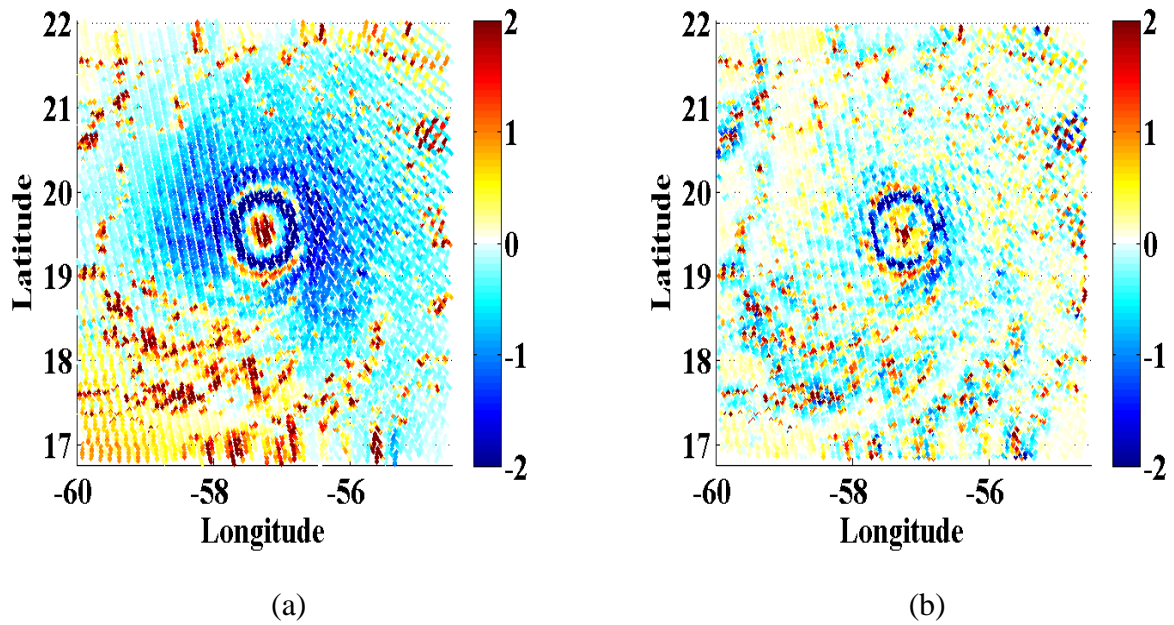


Figure 5.4 Isabel5 H-pol ku-band σ^0 differences (dB) when (a) no correction is applied, and (b) when T-factor correction is applied.

For the same case illustrated in this figure, Fig. 5.5 (a and b) shows the σ^0 measurements scatter plot comparison with color indicating the T-factor. These results clearly show the benefit of the T-factor correction in panel-b.

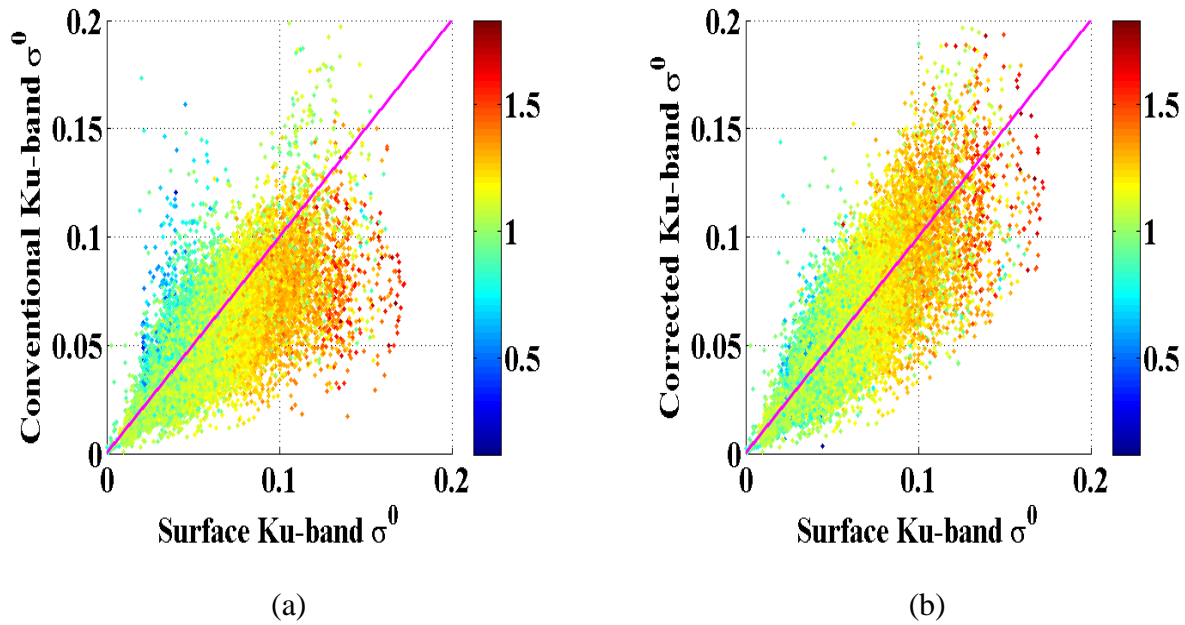


Figure 5.5 Isabel5 H-pol ku-band differences when (a) no correction to the σ^0 is applied, and (b) when T-factor correction is applied.

5.2 Wind Speed Retrievals

The goal of this section is to evaluate the capability of the rain corrected Ku-band OVW algorithm to retrieve accurate wind speeds in extreme weather conditions. For this purpose, we compare WRF hurricane surface wind fields interpolated to the center of the 10 km WVC with the corresponding scatterometer retrieved wind speeds using three different OVW retrieval algorithms: namely, conventional C-band, conventional Ku-band, and the new rain corrected Ku-band. Figs 5.6 and 5.7 show image comparisons for retrieved and truth wind speeds for hurricane scenes Isabel5 and Isabel6. Each panel is a hurricane image of a 5° by 5° latitude/longitude

region where the relative distance scale is 0.1° (~ 10 km) increments. Wind speeds are presented in a color scale that ranges from 0 to 50 m/s.

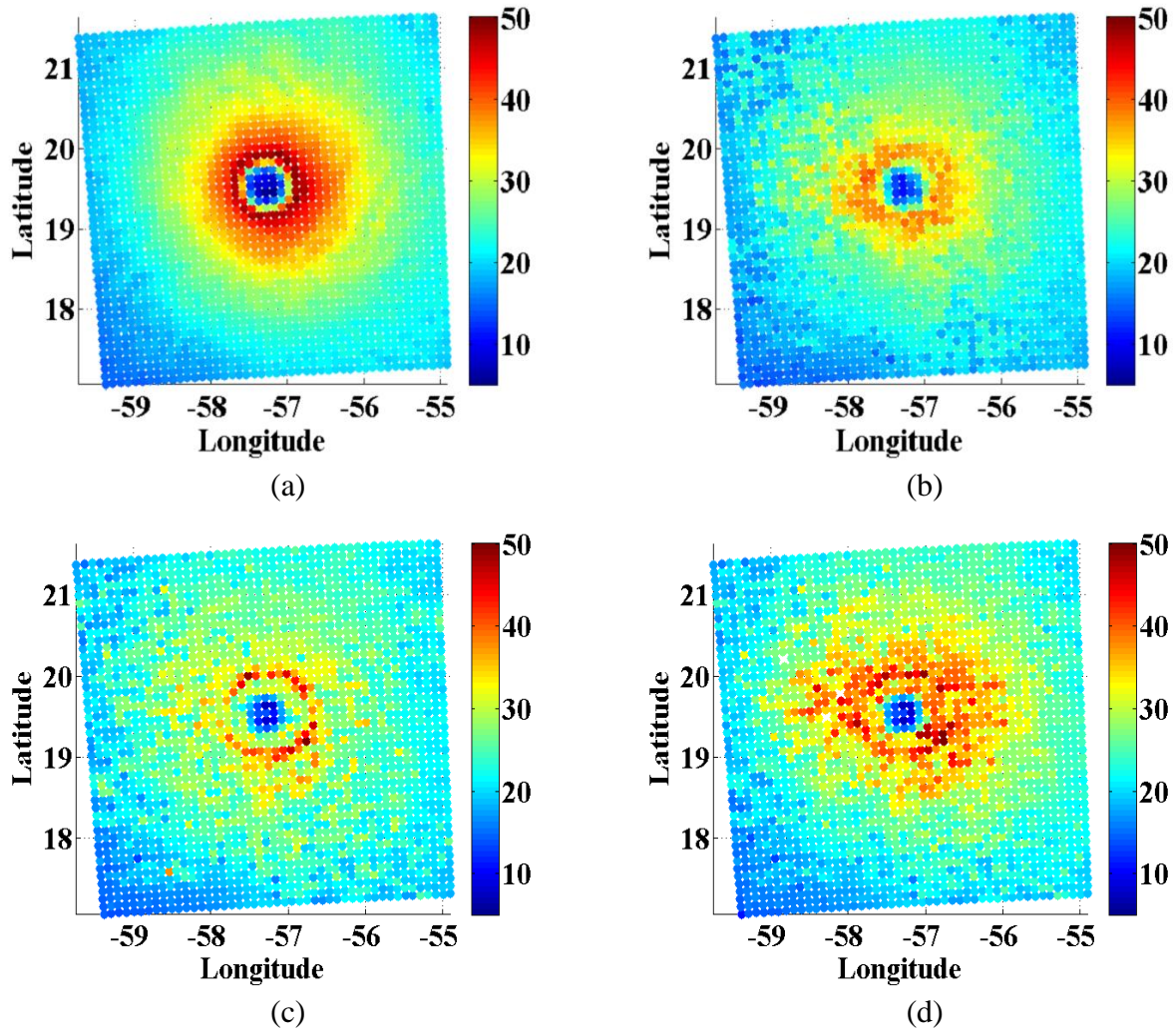


Figure 5.6 Isabel5 surface wind speeds: (a) WRF wind field, (b) conventional C-band retrievals, (c) conventional Ku-band retrievals, and (d) the rain corrected Ku-band retrievals.

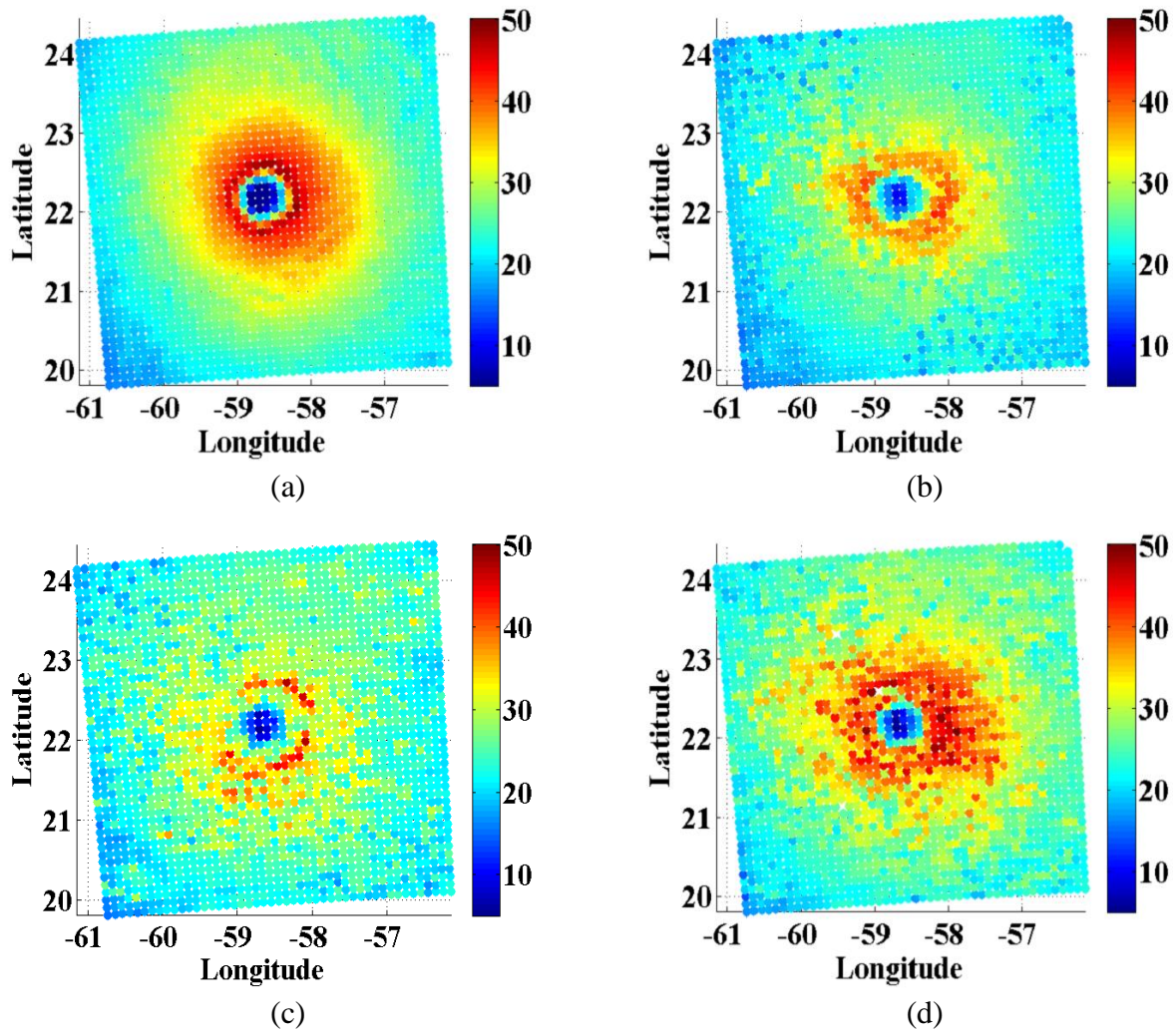
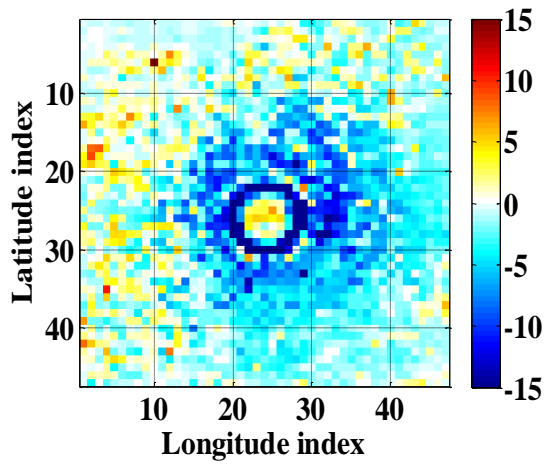


Figure 5.7 Isabel6 surface wind speeds: (a) WRF wind field, (b) conventional C-band OVW retrievals, (c) conventional Ku-band OVW retrievals, and (d) the rain corrected Ku-band OVW retrievals.

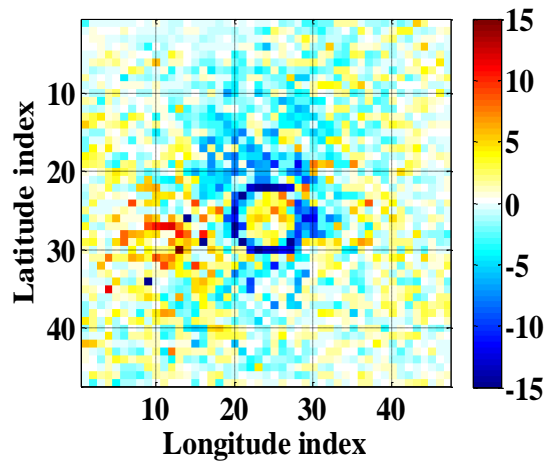
The C-band wind speed retrievals (panel-b in Figs 5.5 and 5.6) show the reduction in wind speed due to spatial smoothing effect of the larger IFOV on wind speeds, especially in the high wind speed gradient regions. On the other hand, the conventional Ku-band retrievals (shown in panel-c of the same figures) suffer from rain effects resulting in large random errors. The rain corrected

Ku-band wind speed retrievals (panel-d in Figs 5.5 and 5.6) has better correlation with the WRF nature run than either the conventional Ku-band or the C-band retrievals.

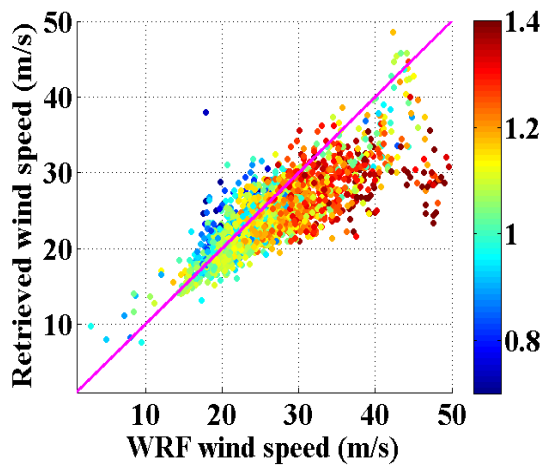
To evaluate the effect of the T-factor on the wind speed retrievals, we compare images of the wind speed retrieval error (retrieved minus WRF) for two cases: where σ_{TOA}^0 values were used for OVW retrieval process and where rain corrected σ^0 values were used. Comparisons are presented below in Figs. 5.8 and 5.9 for hurricane scenes Isabel5 and Isabel6 respectively, where panels-a and -c represent the wind speed comparisons with no correction applied, and panels-b and -d represents the wind speed comparison after we apply the T-factor rain correction. Panels-a and -b show the wind speed error in m/s (indicated by the color), and panels c and d show scatter plot comparison between WRF wind speeds (x-axis) and the retrieved wind speeds (y-axis) with color indicating the corresponding T-factor values.



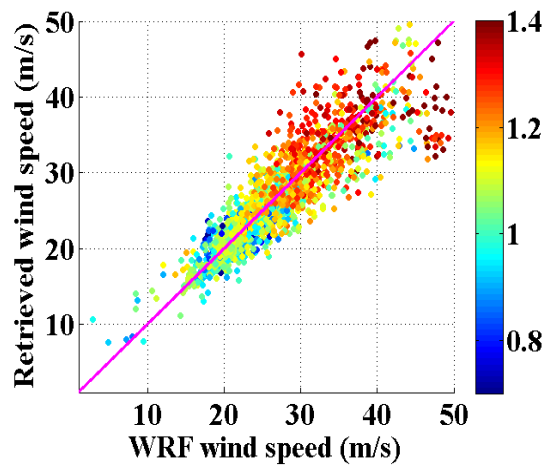
(a)



(b)

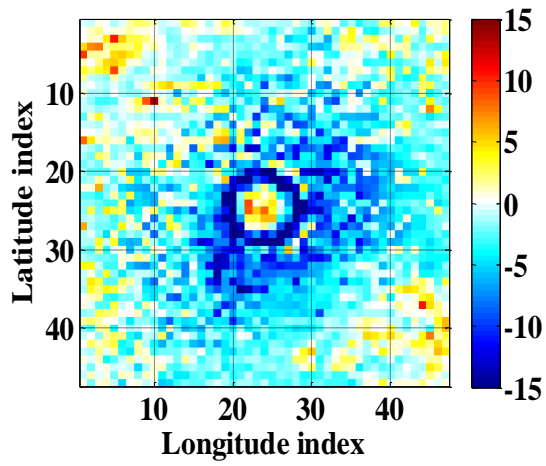


(c)

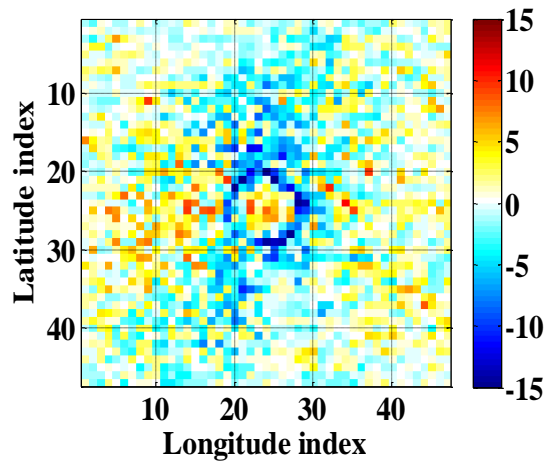


(d)

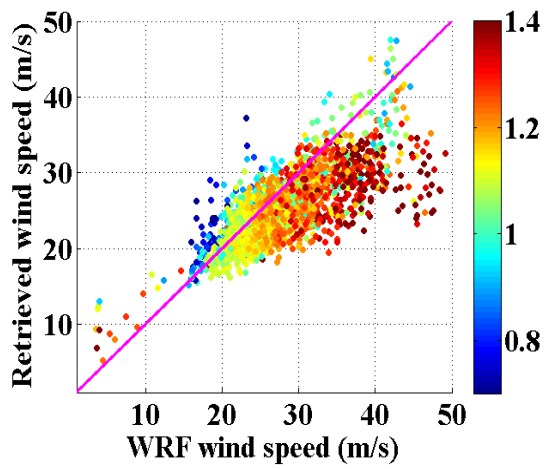
Figure 5.8 Isabel5 case for (a) conventional Ku-band wind speed retrievals errors, (b) rain corrected Ku-band wind speeds retrievals error, (c) conventional Ku-band wind speed scatter plot, and (d) rain corrected Ku-band wind speed scatter plot.



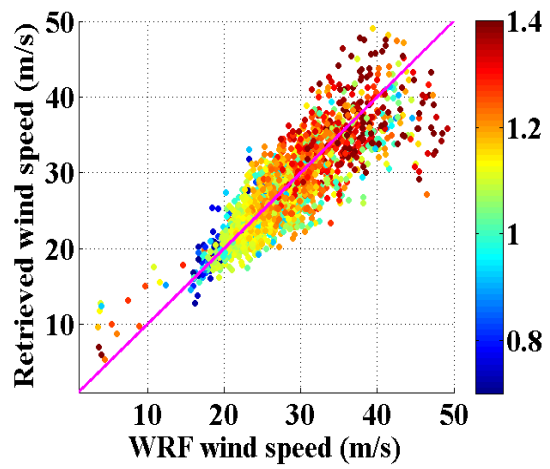
(a)



(b)



(c)

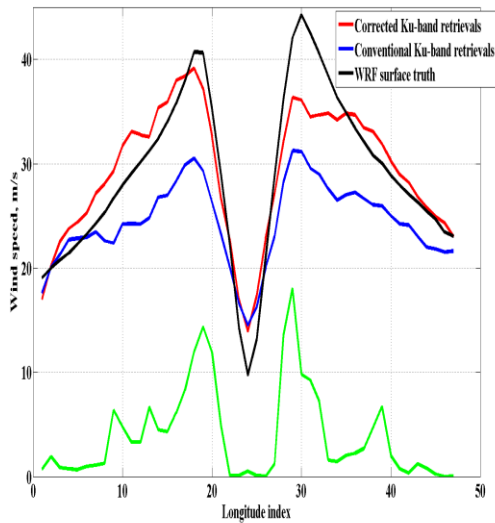


(d)

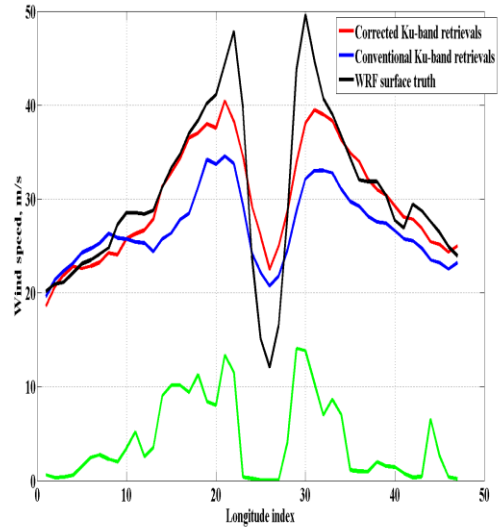
Figure 5.9 Isabel5 case for (a) conventional Ku-band wind speed retrieval errors, (b) rain corrected Ku-band wind speeds retrieval error, (c) conventional Ku-band wind speed scatter plot, and (d) rain corrected Ku-band wind speed scatter plot.

From Figs. 5.8 and 5.9, panel-a shows that the highest wind speed errors are spatially correlated with the hurricane eye wall region, where the highest gradients of rain rates and wind speeds occur. This is consistent with the scatter plot comparison in panel-c where higher values of the T-factor are estimated to compensate for the high rain attenuation effect. Results presented in Panels-b and -d shows significant improvement in the retrievals after applying the rain correction.

Furthermore, radial cuts through Isabel5 hurricane scene wind speed and rain field are show in Fig. 5.10 for an east/west (panel-a) and a north/south (panel-b) passes through the storm. The Solid black line represents WRF wind speeds, blue solid line represents conventional Ku-band retrieved wind speeds, red solid line represents rain corrected Ku-band retrieved wind speeds, and green solid line represents WRF rain rate (scaled down by 50%). Here, the effects of rain attenuation are apparent on both Ku-band retrievals; but the T-factor rain corrected version is superior.



(a)



(b)

Figure 5.10 Isabel5 case for (a) east/west and (b) north/south radial cuts through the storm. Solid black line represents WRF wind speeds, blue solid line represents conventional Ku-band retrieved wind speeds, red solid line represents rain corrected Ku-band retrievals.

Further, we analyze the wind speed retrieval error sensitivity to wind speed and rain rate based on four hurricane scenes (Isabel1, Isabel2, Isabel5, and Isabel6), and the results are presented in Fig. 5.11. Here the root mean squared error (RMSE) surface is shown as a function of wind speed (0-50 m/s) and rain rate (0-60 mm/h). The RMSE is maximized in regions of high wind speeds and high rain rates due to rain attenuation effects. Moreover, at low wind speeds, residual errors in the T-factor correction due to light rain can lead to significant errors in the retrieved wind speeds.

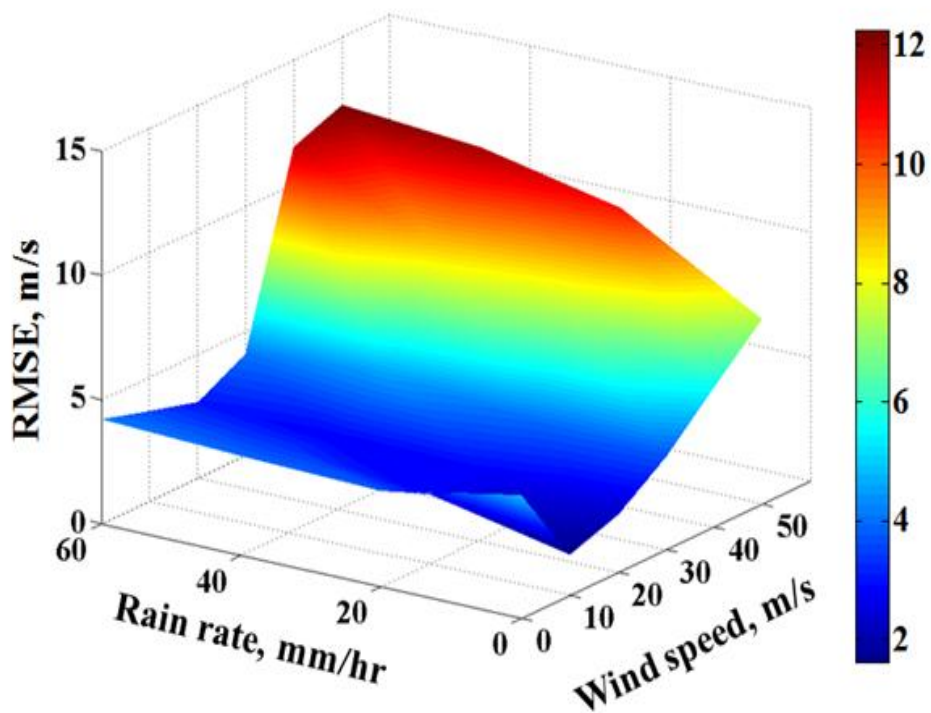


Figure 5.11 RMSE surface as a function of wind speed (m/s) and rain rate (mm/h)

Table 5.1 summarizes the mean and standard deviation (STD) of the scalar differences between the retrieved wind speeds and the corresponding surface truth for different wind speed bins based on four hurricane scenes (Isabel1, Isabel2, Isabel5, and Isabel6).

Table 5.1 Wind speed comparisons for different wind speed bins

Wind speed range	Conventional Ku-band Retrievals (m/s)		Corrected Ku-band Retrievals (m/s)		Number of points
	Mean	STD	Mean	STD	
0-5 m/s	5.1	2.1	5	2.6	15
5-10 m/s	1.8	2.2	2.1	2.2	94
10-15 m/s	1.7	2	0.6	2.2	477
15-20 m/s	0.8	1.9	0.4	1.6	2582
20-25 m/s	-0.1	3.4	0.2	2	4659
25-30 m/s	-1.7	5	0.1	2.9	2893
30-35 m/s	-4.3	5.7	-0.5	3.6	1493
35-40 m/s	-6.6	7.5	-1.5	3.9	644
40-45 m/s	-5.4	5.5	-1.7	4.9	265
45-50 m/s	-17.4	7.2	-10.3	5	129

Finally, speed error statistics were evaluated with respect to the WRF truth field at the WVC resolution. Figure 5.12 summarizes the biases and the standard deviation of the scalar differences between the retrieved wind speeds and the corresponding surface truth for different wind speed bins. The solid red and blue lines represent the conventional Ku-band wind speed retrievals statistics, and the rain corrected Ku-band wind speed retrievals statistics respectively.

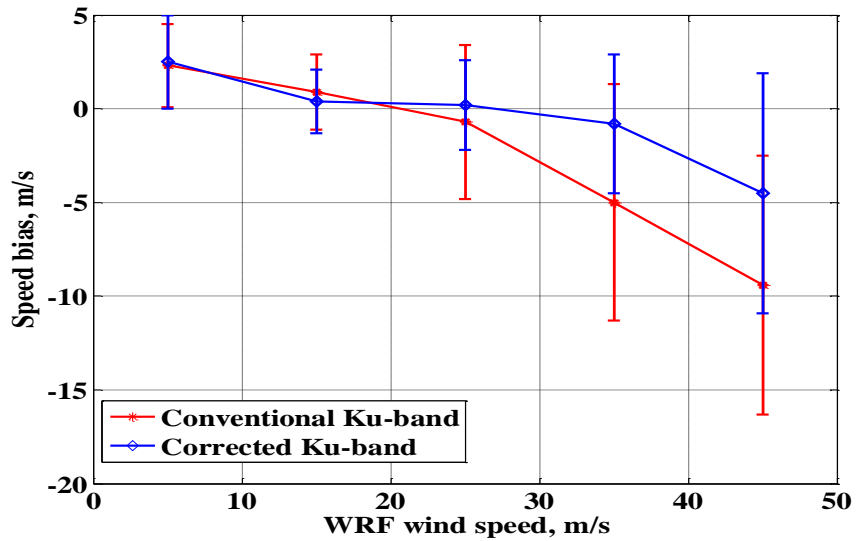


Figure 5.12 Wind speed retrieval error statistics for conventional Ku-band speed retrievals and rain corrected Ku-band speed retrievals.

According to these results, the rain corrected Ku-band wind speed retrievals are superior in both the mean and the standard deviation (STD), especially for higher wind speed regions (> 20 m/s).

5.3 Wind Direction Retrievals

In this dissertation, no wind direction alias selection technique was implemented, and the closest alias to the WRF wind direction was chosen as the retrieved value. In other words, wind direction retrievals were based on the assumption that a perfect alias selection technique was implemented; thus, this approach results in somewhat optimistic wind direction retrieval errors. Existing wind alias selection techniques such as nudging and median filtering [34] may be

applied to yield more realistic results; however the relative comparisons between conventional and rain corrected retrievals are still valid.

Figure 5.13, shows a wind direction comparison between two OVW retrieval algorithms and the corresponding WRF surface truth for four hurricane scenes (Isabel1, Isabel2, Isabel5, and Isabel6). Panel-a shows the conventional Ku-band retrievals, and panel-b shows the rain corrected Ku-band retrievals. The color scale indicates the density of points where warm colors indicate high density and cool colors indicate low density.

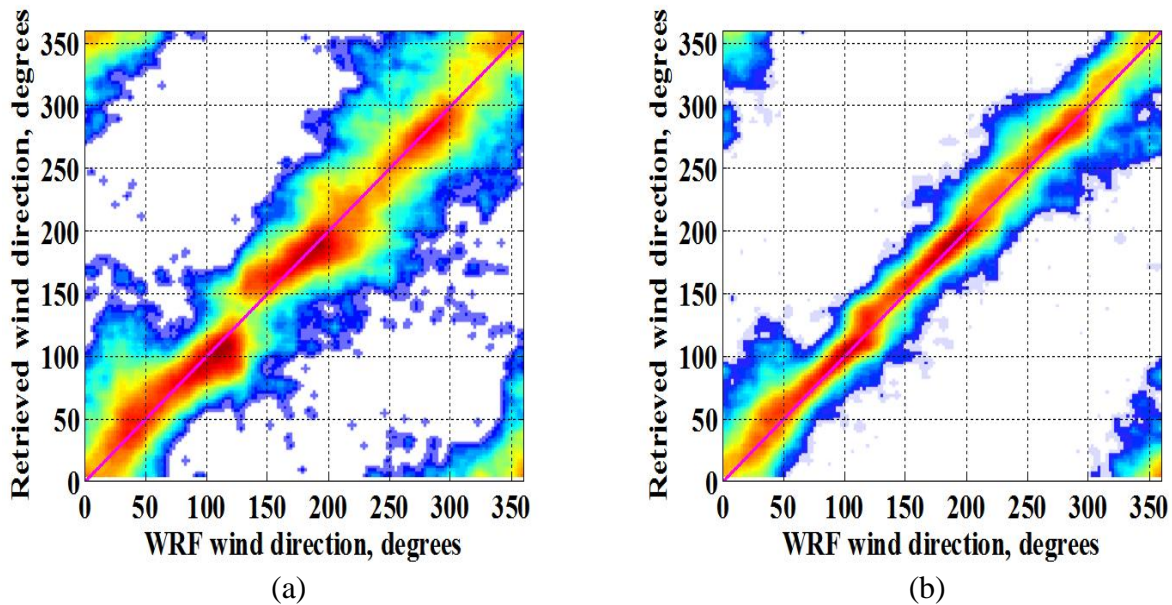


Figure 5.13 Wind direction comparison between WRF surface truth and (a) the conventional Ku-band retrievals, and (b) the rain corrected Ku-band retrievals.

From these results, it is apparent that the rain corrected Ku-band wind direction retrievals are superior in both the mean and the STD. Final conclusions and summary of future work are presented next in Chapter 6.

CHAPTER 6 : SUMMARY & CONCLUSION

Accurate observations of ocean surface vector winds from spaceborne earth observing satellites have been proven to be extremely useful for many oceanographic and meteorological applications. They provide global mapping of ocean surface winds with more uniform sampling and coverage than *in situ* observations. More importantly, in extreme weather events, spaceborne wind observations have been crucial to weather forecast and modeling activities, and warning capabilities.

Experience with the currently available satellite OVW measurements and the continuous increase in the operational needs resulted in new operational XOVWM requirements for future scatterometry missions. Thus, in response to the scientific community, NASA's JPL has proposed the DFS as a baseline scatterometer onboard the GCOM-W2 satellite mission planned by JAXA in the coming few years.

6.1 Summary and Conclusion

Under this dissertation, we have developed a novel OVW retrieval algorithm for the next generation NASA/NOAA missions. It utilizes the rain corrected Ku-band scatterometer measurements to infer accurate winds after correcting them for rain effects using the simultaneous C-band active measurements and multi-frequency passive radiances.

Being based on the future GCOM-W2 mission, no real data were available; hence simulated data were used to evaluate the performance and study the feasibility of the algorithm. High-resolution (1.3 km) hurricane wind and precipitation fields were simulated for several scenes of Hurricane Isabel in 2003 using the WRF model and RTM with Mie-scattering.

To evaluate the fidelity of the simulation, real Isabel hurricane passes from SeaWinds and AMSR onboard ADEOS-II were used. The analysis of these satellite data provided confidence in the capability of the simulation to generate realistic active and passive measurements at the top of the atmosphere taking rain effects into consideration.

Rain can affect scatterometer σ^0 measurements in three ways: attenuation, rain volume backscatter, and splash. All of these introduce errors into the process of estimating OVW at the surface. Typically, in extreme weather events, where rain is very intense, the attenuation effect dominates leading to underestimated retrieved winds.

A rain correction procedure for the Ku-band scatterometer measurements was developed under this dissertation that modeled the rain attenuation and rain volume backscatter as a lumped integrated transmissivity or “T-factor”. We used a high-fidelity simulation to produce C-band active measurements and dual polarized AMSR Tb’s observations for two hurricane cases. Using these data an empirical T-factor multilinear regression was performed. Afterwards, the corrected Ku-band active measurements were fed to the conventional MLE technique to retrieve wind speeds and directions in a 10×10 km wind vector cells.

To evaluate the performance of the algorithm, OVW retrievals were obtained using the corrected Ku-band measurements, and the wind measurement performance was compared with that of the conventional Ku-band measurements. Results from the developed algorithm are very encouraging and they demonstrate the potential to improve wind measurements in extreme wind events for future wind scatterometry missions such as the proposed GCOM-W2.

6.2 Future Work

Several avenues for future research are apparent to us. The present simulation is limited in possible dynamic range of rain parameters, thus the simulated observations need to be validated using different sets of rain micro-physics. Moreover, only two hurricane scenes were used to train the T-factor regression model, so having more simulated hurricane cases to train the T-factor model will include a wider range of geophysical parameters, hence improve the robustness of the model.

Moreover, the C-band scatterometer measurements are currently only used in the rain correction procedure as one of the independent variables used in the multilinear regression model used to estimate the T-factor. In the future, we want to exploit the sensitivity of the H-pol C-band scatterometer measurements in combination with the Ku-band scatterometer measurements to

retrieve OVW. One way of doing that is to combine these two active measurements in the MLE cost function.

Finally, in this dissertation, we did not incorporate a wind direction alias selection technique into the OVW retrieval algorithm, and perfect alias selection was assumed by choosing the closest wind directions (aliases) to the nature run. Several good alias selection techniques are currently available for conventional scatterometer OVW retrievals [53, 54], and any of them can be implemented in the OVW retrieval process described in the dissertation.

APPENDIX A. SPACE-BORNE ACTIVE MICROWAVE WIND ESTIMATION HISTORY

The idea of using radar to estimate ocean surface wind conditions was originated during the World War II (1940's), where the interest was primarily clutter rejection in military radar systems. During this period, it was recognized that normalized radar cross section of the ocean surface (σ^0) was related to wind velocity. Later, in 1963, Richard Moore and Willard Pierson, proposed that ocean wind speed could be inferred using radar remote sensing techniques by interpreting the magnitude of the ocean backscatter.

During the 1960's and 70's, ocean remote sensing was actively studied within the National Aeronautics and Space Administration (NASA) and US Navy research communities to define the fundamental physics and develop the technology of microwave scatterometry for the measurement of ocean winds.

The advent of the first spaceborne wind scatterometers, on the NASA's SeaSat-A mission in 1978, proved that OVW retrievals from space are possible [9]. As a follow-up mission, the NASA scatterometer (NSCAT) aboard the Advanced Earth Observing Satellite (ADEOS) was launched in 1996. Unfortunately, the ADEOS satellite, however, failed after only one-year of operation, which prematurely terminated the NSCAT measurements..

During the NSCAT era, the next generation scatterometer called SeaWinds was being designed. To fill the gap in coverage caused by the NSCAT failure, a SeaWinds instrument was flown on

the QuikSCAT satellite as a “quick recovery” mission in June 1999. The next SeaWinds instrument was launched in November 2002 aboard ADEOS-II. Both SeaWinds instruments provided unprecedented earth-wide coverage of ocean winds. Additional scatterometers have been launched by the European Space Agency (ESA) aboard the European Remote Sensing-1 (ERS-1) and ERS-2 satellites. As a sequel instrument to ERS-1 and ERS-2, the Advanced Scatterometer (ASCAT), was launched in 2006 on the European Meteorological Operational (MetOp) satellite [55]. An illustration of satellite scatterometers from 1974 to present (2011) is given in Fig. A.1 and key instrument characteristics are summarized in Table A.1.

ERS-1 and -2 have provided nine years of continuous wind data with daily global ocean coverage of 40%. Their measurements have 50- km spatial resolution but are sampled at 25 km. NSCAT covered 77% of global ocean at 25-km resolution while QuikSCAT covered 93% of the global ocean in a single day. QuikSCAT has provided over a decade of standard wind products with 25-km spatial resolution, but special products with 12.5-km resolution for selected regions have been produced. In one decade, daily wind vector coverage increases from 41%, to 77%, then to 93%, and spatial resolution improves from 50km, to 25 km, and to 12.5 km.

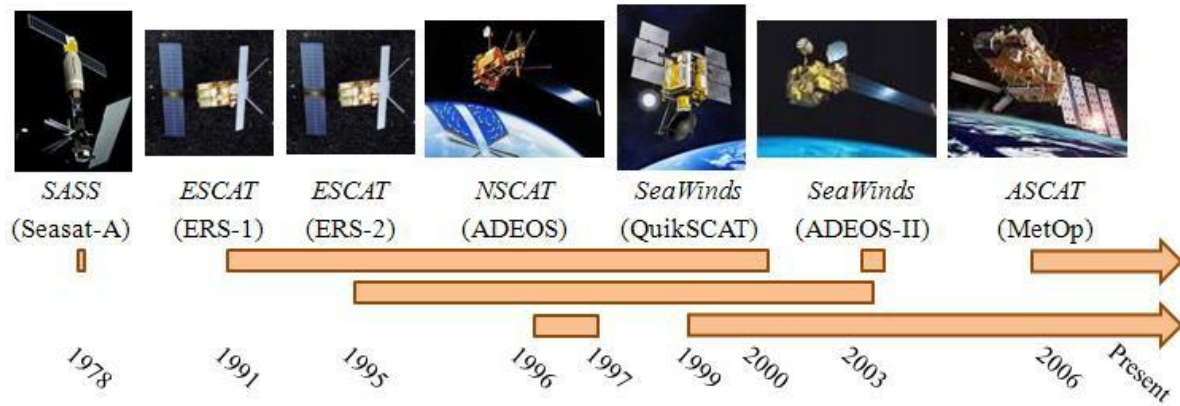





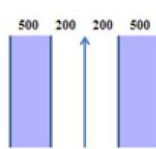

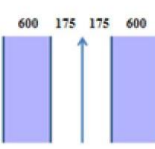
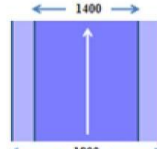
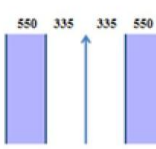


Figure A.1 Spaceborne wind measuring scatterometers sponsored by NASA and ESA.

Table A.1 Characteristics of space-borne wind scatterometers.

	SASS	ESCAT	NSCAT	SeaWinds	ASCAT
Frequency (GHz)	14.6	5.3	14.0	13.4	5.3
Antenna Azimuth Orientations					
Polarizations	V-H, V-H	VV	V, V-H, V	H(Inner), v(Outer)	VV
Resolution (km)	50/100	25/50	25/50	25/6×25	25/50
Swath (km)					
Incidence Angles	0°-70°	18°-59°	17°-60°	46°, 54°	25°-65°

APPENDIX B. THE SAFFIR-SIMPSON HURRICANE WIND SCALE

The Saffir-Simpson Hurricane Wind Scale (SSHS) is a 1 to 5 categorization based on the hurricane's intensity at the indicated time. It was originally developed by wind engineer Herb Saffir and meteorologist Bob Simpson, and has been an excellent tool for alerting the public about the possible impacts of various intensity hurricanes. The scale provides examples of the type of damage and impacts in the United States associated with winds of the indicated intensity. The determining factor in the scale is the maximum 1-minute sustained surface wind speed, which is the peak 1-minute wind at the standard meteorological observation height of 10 m [33 ft] over unobstructed exposure. The SSHS is presented in Table B .1.

Table B.1 Saffir-Simpson Hurricane Scale

Storm Class	m/s	mph	kt	km/h
Tropical depression	0-17	0-38	0-33	0-62
Tropical storm	18-33	39-73	34-63	63-117
1	34-43	74-95	64-82	119-153
2	44-49	96-110	83-95	154-177
3	50-58	111-130	96-113	178-209
4	59-69	131-155	114-135	210-249
5	> 70	> 156	> 135	> 250

APPENDIX C. MAXIMUM LIKELIHOOD ESTIMATION

Maximum likelihood (MLE) is a well-known statistical method to estimate parameters using a mathematical model and applying this to an empirical dataset with random errors of known probability distribution. The principle behind maximum likelihood estimation is to determine the variables that maximize the likelihood probability of the sample data. The advantages of this method are its robustness and its efficient method to determine the mean of the process.

Consider x is a continuous random variable with PDF

$$f(x; \theta_1, \theta_2, \dots, \theta_k) \tag{C.1a}$$

where $\theta_1, \theta_2, \dots, \theta_k$ are k unknown constant parameters. For an experiment with N independent observations, x_1, x_2, \dots, x_N . The likelihood function is defined as follows:

$$L(x_1, x_2, \dots, x_N | \theta_1, \theta_2, \dots, \theta_k) = L = \prod_{i=1}^N f(x_i; \theta_1, \theta_2, \dots, \theta_k) \tag{C.1b}$$

Assuming Gaussian distribution with identical standard deviation σ , the PDF of the distribution is given by:

$$f(x) = \frac{1}{\sigma\sqrt{2\pi}} e^{-\frac{1}{2}\left(\frac{x-\bar{x}}{\sigma}\right)^2} \quad (\text{C.2})$$

where \bar{x} denotes the mean value, and σ is the standard deviation of the process. MLE of the process is compute by (C.1) and yields:

$$L = \prod_{i=1}^N \frac{1}{\sigma\sqrt{2\pi}} e^{-\frac{1}{2}\left(\frac{x_i-\bar{x}}{\sigma}\right)^2} \quad (\text{C.3a})$$

$$= \frac{1}{(\sigma\sqrt{2\pi})^N} e^{-\frac{1}{2}\sum_{i=1}^N \left(\frac{x_i-\bar{x}}{\sigma}\right)^2} \quad (\text{C.3b})$$

For convenience L is usually expressed in logarithmic domain as:

$$\Lambda = \ln(L) = \ln \sum_{i=1}^N \ln f(x_i; \theta_1, \theta_2, \dots, \theta_k) \quad (\text{C.4a})$$

$$= -\frac{N}{2} \ln(2\pi) - N \ln \sigma - \frac{1}{2} \sum_{i=1}^N \left(\frac{x_i - \bar{x}}{\sigma}\right)^2 \quad (\text{C.4b})$$

The MLE's of $\theta_1, \theta_2, \dots, \theta_k$ are determined by maximizing L (or Λ). Taking the partial derivatives of Λ with respect to each parameter and equates to zero yields:

$$\frac{\partial(\Lambda)}{\partial \bar{x}} = \frac{1}{\sigma^2} \sum_{i=1}^N (x_i - \bar{x}) = 0 \quad (\text{C.5a})$$

$$\frac{\partial(\Lambda)}{\partial \sigma} = -\frac{N}{\sigma} + \frac{1}{\sigma^3} \sum_{i=1}^N (x_i - \bar{x})^2 = 0 \quad (\text{C.5b})$$

Solving (C.5a) and (C.5b) simultaneously, solutions are:

$$\bar{x} = \frac{1}{N} \sum_{i=1}^N x_i \quad (\text{C.6a})$$

$$\sigma = \sqrt{\frac{1}{N} \sum_{i=1}^N (x_i - \bar{x})^2} \quad (\text{C.6b})$$

This implies that by minimizing $\sum_{i=1}^N (x_i - \bar{x})^2$ will also maximizes L (or Λ).

APPENDIX D. V-POL TB FIELDS FOR HURRICANE ISABEL

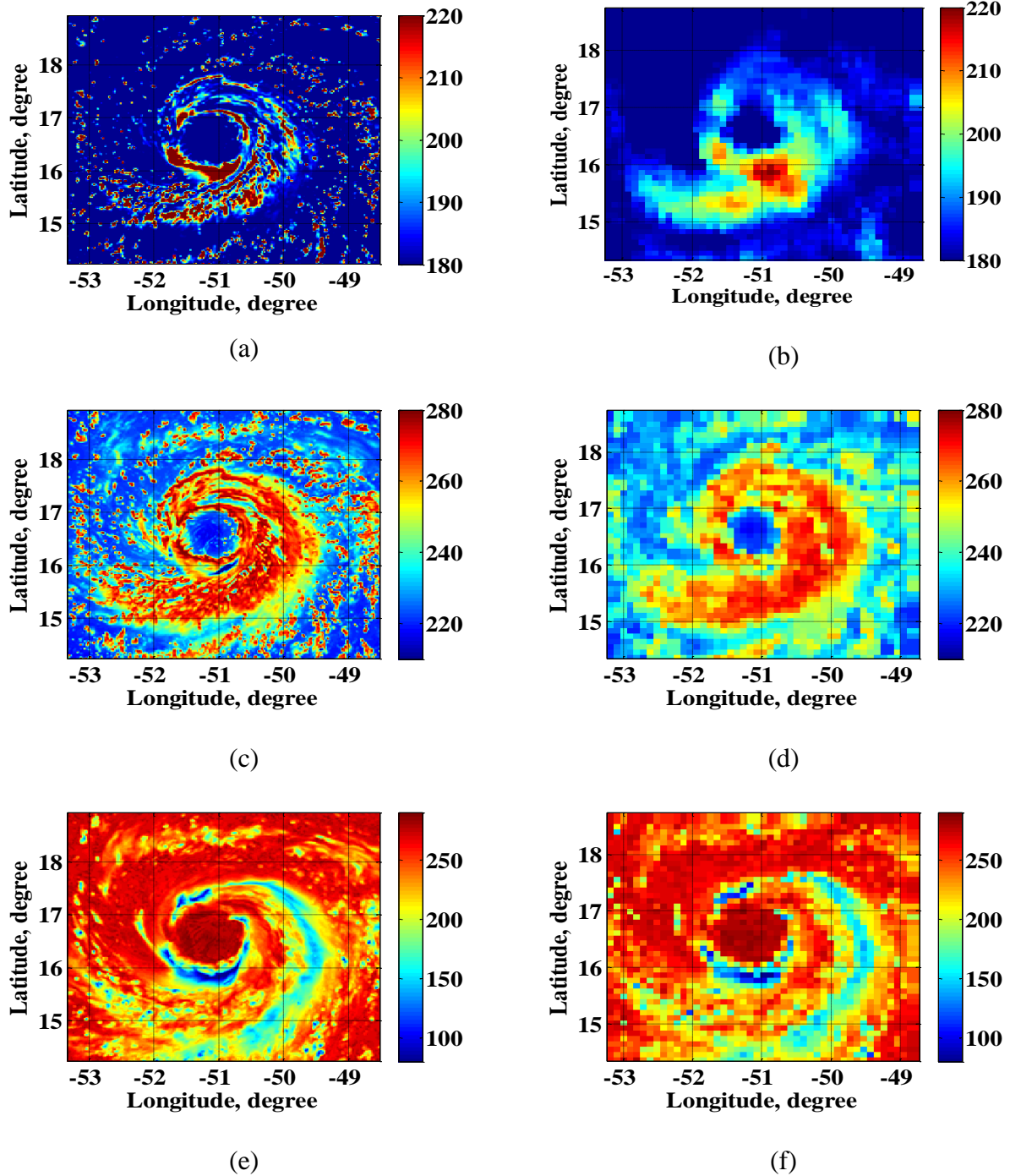


Figure D.1 V-pol Tb fields on a latitude/longitude grid, for hurricane Isabel in September 2003. Right side panels (a, c, and e) show the original high resolution Tb fields, and the left side panels (b, d, and f) show the averaged Tb fields over the antenna pattern

APPENDIX E. V-POL WIND DIRECTIONAL SIGNATURE FOR HURRICANE SCENES ISABEL3 & ISABEL4

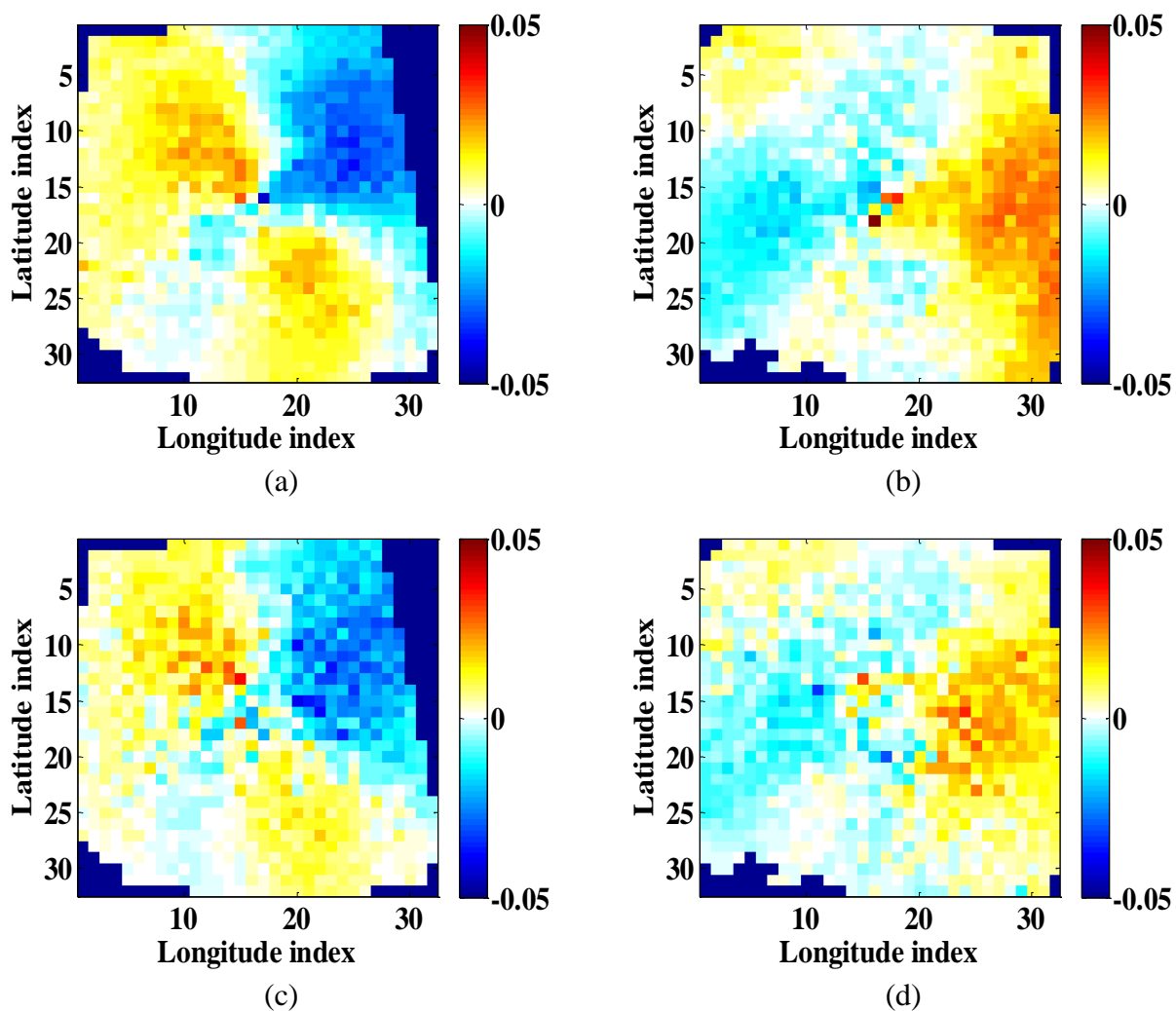
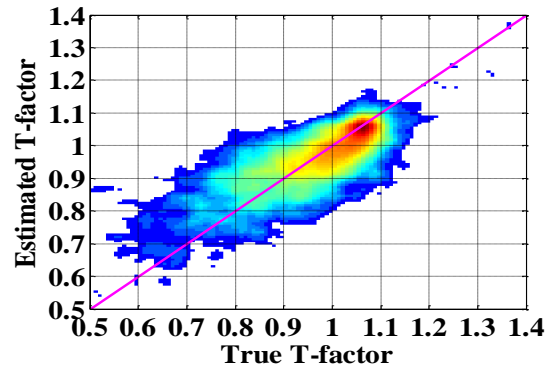
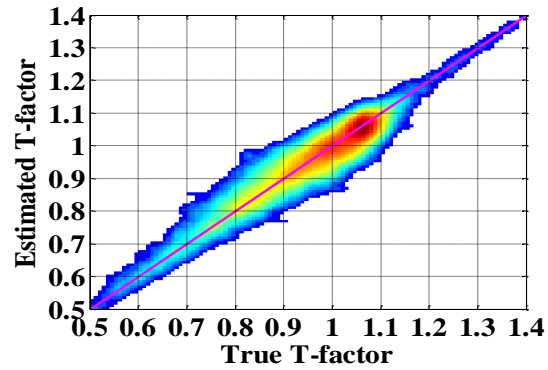


Figure E.1 V-pol Wind directional signature for hurricane scenes Isabel3 (left panels) and Isabel4 (right panels). Upper panels [(a) and (b)] give the simulated results, and lower panels [(c) and (d)] give the SeaWinds measurements from ADEOS-II.

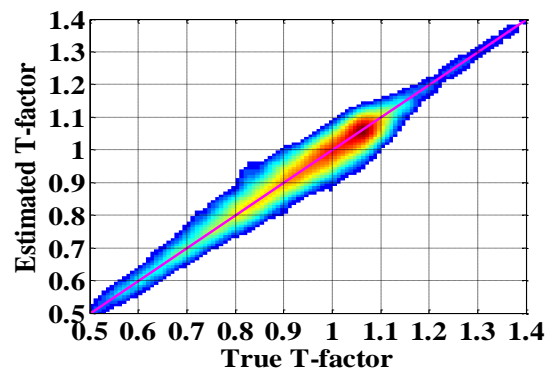
APPENDIX F. V-POL T-FACTOR COMPARISON



(a)



(b)



(c)

Figure F.1 V-pol T-factor comparison using (a) AMSR V-pol Tb's only, (b) AMSR V- and H-pol Tb's, and (c) AMSR V- and H-pol Tb's with C-band σ^0 measurements

LIST OF REFERENCES

- [1] K. Trenberth, "Uncertainty in Hurricane and Global Warming," *Journal of Science*, vol. 308, pp. 1753–1754, 2005.
- [2] R. Atlas, *et al.*, "Application of SeaWinds scatterometer and TMI-SSM/I rain rates to hurricane analysis and forecasting," *ISPRS J. Photogramm, Remote Sensing*, vol. 59, pp. 233–243, 2005.
- [3] S. H. Chen, "The impact of assimilating SSM/I and QuikSCAT satellite winds on Hurricane Isidore simulations," *Journal of Monthly Weather*, vol. 135, pp. 549–566, 2007.
- [4] Z. Jelenak and P. S. Chang. (2008, NOAA Operational Satellite Ocean Surface Vector Winds - QuikSCAT Follow-On Mission: User Impact Study Report. 90. Available: http://manati.orbit.nesdis.noaa.gov/SVW_nextgen/QFO_user_impact_study_final.pdf
- [5] D. B. Chelton, *et al.*, "On the use of QuikSCAT scatterometer measurements of surface winds for marine weather prediction," *Journal of Monthly Weather*, vol. 134, pp. 2055–2071, 2006.
- [6] P. S. Chang and Z. Jelenak, "NOAA Operational Ocean Surface Vector Winds Requirements Workshop Report," National Hurricane Center, Miami, 2006.
- [7] D. Esteban-Fernandez, *et al.*, "Dual-polarized C-and Ku-band ocean backscatter response to hurricane-force winds," *Journal of Geophysical Research*, vol. 111, p. C08 013, 2006.
- [8] Z. Jelenak and P. S. Chang, "Impact Of The Dual-Frequency Scatterometer On NOAA Operations," presented at the Geoscience and Remote Sensing Symposium (IGARSS), 2010.
- [9] R. K. Moore and W. L. Jones, "Satellite Scatterometer Wind Vector Measurements - the Legacy of the Seasat Satellite Scatterometer," *IEEE Geoscience and Remote Sensing Society Newsletter*, pp. 18-36, 2004.
- [10] W. L. Jones, *et al.*, "The SeaSat-A Satellite Scatterometer: The Geophysical Evaluation of Remotely Sensed Wind Vectors Over the Ocean," *Journal of Geophysical Research*, vol. 87, pp. 3297 - 3317, 1982.
- [11] C. A. Balanis, *Advanced Engineering Electromagnetics*. New York: Wiley, 1989.
- [12] F. T. Ulaby, *et al.*, *Microwave Remote Sensing* vol. 2: Addison-Wesley Publishing Company inc., 1982.
- [13] W. L. Jones and L. C. Schroeder, "Radar Backscatter from the Ocean, Dependence on Surface Friction Velocity," *Boundary Layer Meteorology* vol. 13, pp. 133 – 149, 1978.
- [14] J. T. Brucks, *et al.*, "Comparison of Surface Wind Stress Measurements: Airborne Radar Scatterometer Versus Sonic Anemometer," *Journal of Geophys. Res.*, vol. 85, pp. 4967 - 4976, 1980.
- [15] W. J. Plant, "Relationship between Stress Wind and Wave Slope," *Journal of Geophys. Res.*, vol. 87, pp. 1961-1967, 1982.
- [16] W. L. Jones, *et al.*, "Aircraft Measurements of the Microwave Scattering Signature of the Ocean," *IEEE Trans. Ant & Prop/IEEE J. Oceanic Eng. (Special Issue on Radio Oceanography)*, vol. AP-25, pp. 52-61, 1977.

- [17] L. C. Schroeder, *et al.*, "The Relationship Between Wind Vector and Normalize Radar Cross section Used to Derive SeaSat-A Satellite Scatterometer Winds," *Journal of Geophysical Research*, vol. 87, pp. 3318 - 3336, 1982.
- [18] L. Schroeder, *et al.*, "AAFE RadScat 13.9-GHz measurements and analysis: wind-speed signature of the ocean," *IEEE J. Oceanic Engr*, vol. 10, pp. 346-357, 1985.
- [19] F. J. Wentz and D. K. Smith, "A model function for ocean-normalized radar cross sections at 14.6 GHz derived from NSCAT observations," *Journal of Geophys. Res.*, vol. 104, pp. 11499-11514, 1999.
- [20] W. T. Liu, *Evaluation of parameterization models for determining air-sea exchanges in heat and momentum from satellite data, Application of the existing satellite data to the study of ocean surface energetic*: University of Wisconsin Press, 1981.
- [21] W. Tang and W. T. Liu, "Equivalent Neutral Wind," ed: JPL Publication, SuDoc NAS 1.26:112603, 1996, pp. 96-17.
- [22] M. H. Freilich and R. S. Dunbar, "Derivation of satellite wind model functions using operational surface wind analyses: An altimeter example," *Journal of Geophys. Res.*, vol. 98, pp. 14 633–14 649, 1993.
- [23] A. Stoffelen and D. Anderson, "Scatterometer data interpretation: Estimation and validation of the transfer function CMOD4," *Journal of Geophys. Res.*, vol. 102, pp. 5767–5780, 1997.
- [24] F. M. Naderi, *et al.*, "Spaceborne radar measurement of wind velocity over the ocean - an overview of the NSCAT scatterometer system," *IEEE Proceedings*, vol. 79, pp. 850-866, 1991.
- [25] D. G. Long and J. M. Mendel, "Identifiability in wind estimation from scatterometer measurements," *IEEE Trans. Geoscience and Remote Sensing*, vol. 29, pp. 268-276, 1991.
- [26] R. N. Hoffman and S. M. Leidner, "An introduction to the near-real-time QuikSCAT data," *Weather and Forecasting*, vol. 20, pp. 476-493, 2005.
- [27] R. K. Moore, *et al.*, "Preliminary Study of Rain Effects on Radar Scattering from Water Surfaces," *IEEE Journal of Oceanic Eng.*, vol. OE-4, pp. 31-32, 1979.
- [28] C. Craeye, "Study of Microwave Scattering from Rain and Wind Roughened Seas," PhD, Universite Catholique de Louvain, Louvain, Belgium, 1998.
- [29] C. Craeye, *et al.*, "Scattering by artificial wind and rain roughened water surfaces at oblique incidences," *Int. Journal of Remote Sens.*, vol. 18, pp. 2241–2246, 1997.
- [30] D. W. Draper and D. G. Long, "Simultaneous wind and rain retrieval using SeaWinds data," *IEEE Trans. Geoscience and Remote Sensing*, vol. 42, pp. 1411-1423, 2004.
- [31] C. A. Mears, *et al.*, "Detecting rain with QuikSCAT," presented at the IEEE Int. Geoscience and Remote Sensing Symp., Honolulu, HI, 2000.
- [32] D. E. Weissman, *et al.*, "Effects of rain rate and wind magnitude on SeaWinds scatterometer wind speed errors," *Journal of Atmos. Oceanic Technology*, vol. 19, pp. 738-746, 2002.
- [33] J. Tournadre and J. C. Morland, "The Effects of Rain on TOPEX/Poseidon Altimeter Data," *IEEE Trans. Geoscience and Remote Sensing*, vol. 35, pp. 1117-1135, 1997.

- [34] B. W. Stiles, *et al.*, "Direction interval retrieval with threshold nudging: A method for improving the accuracy of QuikSCAT winds," *IEEE Geoscience and Remote Sensing*, vol. 40, pp. 79–89, 2002.
- [35] J. N. Huddleston and B. W. Stiles, "A multi-dimensional histogram rain flagging technique for SeaWinds on QuikSCAT," in *IGARSS*, Honolulu, HI, 2000, pp. 1232–1234.
- [36] M. Portabella and A. Stoffelen, "Rain detection and quality control of SeaWinds," *Journal of Atmos. Oceanic Technology*, vol. 18, pp. 1171–1183, 2001.
- [37] Z. Jelenak and P. S. Chang, "Dual Frequency Scatterometer (DFS) on GCOM-W2 Satellite: Instrument Design, Expected Performance and User Impact," 2009.
- [38] E. Rodríguez, *et al.*, "Progress in the Dual-Frequency Scatterometer for GCOM-W2," 2009.
- [39] K. Tachi, *et al.*, "Advanced Microwave Scanning Radiometer (AMSR): Requirements and Preliminary Design Study," *IEEE Trans. Geoscience and Remote Sensing*, vol. 27, pp. 177-183, 1989.
- [40] M. W. Spencer, *et al.*, "Improved resolution backscatter measurements with the SeaWinds pencil-beam scatterometer," *IEEE Trans. Geoscience and Remote Sensing*, vol. 38, pp. 89–104, 2000.
- [41] W. C. Skamarock, *et al.*, "A description of the Advanced Research WRF Version 3," 2008.
- [42] C. Davis, *et al.*, "Prediction of landfalling hurricanes with the advanced hurricane WRF model," *Journal of Monthly Weather*, vol. 136, pp. 1990-2005, 2008.
- [43] G. Mie, "Beiträge zur Optik trüber Medien, speziell kolloidaler Metallösungen," *Ann. Phys., Vierte Folge*, vol. 25, pp. 377-445, 1908.
- [44] D. G. Long and M. W. Spencer, "Radar Backscatter Measurement Accuracy for a Spaceborne Pencil-Beam Wind Scatterometer with Transmit Modulation," *IEEE Trans. Geoscience and Remote Sensing*, vol. 35, pp. 102-114, 1997.
- [45] K. N. Liou, *An Introduction to Atmospheric Radiation*. New York: Academic Press, 1980.
- [46] F. J. Wentz and R. W. Spencer, "SSM/I rain retrievals within a unified all-weather ocean algorithm," *Journal of the Atmospheric Sciences*, vol. 55, pp. 1613-1627, 1998.
- [47] K. A. Hilburn and F. J. Wentz, "Intercalibrated passive microwave rain products from the unified microwave ocean retrieval algorithm (UMORA)," *Journal of Applied Meteorology and Climatology*, vol. 47, pp. 778-794, 2008.
- [48] F. J. Wentz, *et al.*, "New algorithms for microwave measurements of ocean winds: Applications to SaeSat and Special Sensor Microwave Imager," *Journal of Geophys. Res.*, vol. 91, pp. 2289-2307, 1986.
- [49] D. G. Long, "Wind Field model-based estimation of Seasat scatterometer winds," *Journal of Geophys. Res.*, vol. 98, pp. 14651-14668, 1993.
- [50] S. O. Alswiss, *et al.*, "A Novel Ku-Band Radiometer/Scatterometer Approach for Improved Oceanic Wind Vector Measurements," *IEEE Trans. Geosci. Rem. Sensing*, vol. PP, pp. 1-9, 2011.
- [51] R. Gaston and E. Rodríguez, "QuikSCAT Follow-On Concept Study," JPL, Pasadena, 2008.
- [52] R. Sibson, *Interpreting Multivariate Data*. Chichester: John Wiley, 1981.

- [53] S. J. Shaffer, *et al.*, "A Median-Filter-Based Ambiguity Removal Algorithm For NSCAT," *IEEE Geoscience and Remote Sensing*, vol. 29, 1991.
- [54] S. Thiria, *et al.*, "A Neural Network Approach for modelling Non Linear Transfer functions : Application for Wind Retrieval from Spaceborne Scatterometer Data," *Journal of Geophys. Res.*, vol. 98, pp. 22827-22841, 1993.
- [55] J. Figa-Saldaña, *et al.*, "The advanced scatterometer (ASCAT) on the meteorological operational (MetOp) platform: A follow on for European wind scatterometers," *Remote Sensing*, vol. 28, pp. 404–412, 2002.